Measurement of Differential Cross Section of ϕ-meson Photoproduction from Deuterons near Threshold at SPring-8/LEPS

BY

Po-Ju Lin

Advisors: Dr. Rurng-Sheng Guo
Dr. Wen-Chen Chang

THESIS

Abstract

The differential cross section of $\phi(1020)$ meson photoproduction from deuterium target has been studied and compared with the results from hydrogen target in the energy range from the production threshold to $E_\gamma = 2.4$ GeV. The experiment was performed using linearly-polarized photon beam at SPring-8/LEPS facility. By fitting the missing mass spectra assuming deuteron as target, the contribution of coherent and incoherent interactions are disentangled. The differential cross section of LD_2 coherent interaction has a large exponential slope and the intercept at $t = t_min$ increases with photon energy. The differential cross section of LD_2 incoherent events shows a strong isotopic effect. The structure of non-monotonically increasing are observed in LD_2 incoherent and LH_2 events, indicating the existence of new dynamics that may involve a multigluon exchange beyond standard Pomeron exchange process.

II

Contents

List of Figures

List of Tables

Chapter 1

Introduction

In this chapter, the physics motivation for the study for $\phi(1020)$ meson photoproduction is discussed. The historical background of the intermediate-energy nuclear physics is mentioned. The vector meson photoproduction and some theoretical approaches to it are discussed. The specialty of ϕ-meson photoproduction from deuteron is explained.

1.1 Fundamental

"What is matter made of?" Human being has long been asking this question. It is believed that behind all the multitudinous phenomena, there lies rules which can be described by basic constituents and ultimate ways they interact with each other. Efforts on searching and investigating the fundamental building blocks of matter and the interactions among these building blocks have therefore been made. Not only because of curiosity, but understanding this ancient puzzle would surely shed light on those exciting and challenging problems of the modern science.

Since the question needs to be answered on the most fundamental level, which is to say, on the smallest scale of size, another question arose: how to perform experiments that are capable to measure the desired information about the fundamental property of nature?

The famous scattering experiment performed by Rutherford in 1911 gave a good example. By firing a beam of α-particles into a thin sheet of gold foil and the fact that most of the α-particles passed through but a few of them been deflected or bounced back at large angles, Rutherford concluded that the atoms are consisted of positively charged tiny massive cores surrounded by negatively charged light electrons and therefore overruled the atom model as a diffuse sphere as suggested by J.J. Thomson.

In the same way, scientists used particles as the probes just like what Rutherford did. And the spatial resolution of these kinds of probes is related and limited to the wave-like nature of the particles used, which is similar to the case in optics. By the formulation of Louis-Victor de Broglie, this wave-like nature can be written as:

$$\lambda = h/p \tag{1.1}$$

where λ is the wave length, h is Plank's constant, and p is the particle momentum. As can be seen in the formula, with the higher momentum (that is, higher energy) of the particles used, the shorter wave length and the better resolution can be achieved.

There are three main sources to acquire demanded particles: cosmic rays, nuclear reactors, and particle accelerators. Cosmic rays are free and their energy can be extremely high, but the rate of the desired events from them is too low and they are uncontrollable. The nuclear

reactors provide particles by the disintegration of radioactive nucleus, while the energy scale of the produced particles is limited. The advent of particle accelerators provided convenient and controllable ways to produce particles and interactions, and can reach energies as high as TeV (10^{12} eV) nowadays.

1.2   The Standard Model and the strong interaction

Classical mechanics describes well the world of everyday life. But for objects traveling at speeds comparable to the speed of light, special relativity is needed to make modification, and for objects that are as small as the size of atoms, classical rules are replaced by quantum mechanics. When it comes to objects that are both fast and small, which are usually the case for elementary particles, we need a theory that incorporates relativity and quantum mechanics.

Table 1.1: The fundamental fermions

Particle	Flavour			Q/|e|
quarks	u	c	t	$+2/3$
	d	s	b	$-1/3$
leptons	e	μ	τ	-1
	ν_e	ν_μ	ν_τ	0

The most widely accepted theory of this approach is the quantum field theory (QFT, actually it's a collection of related theories). Under the framework of QFT and with the accumulated experimental evidence, the Standard Model which incorporates quantum electrodynamics (QED), the Glashow-Weinberg-Salam theory of electroweak process, and quantum chromodynamics (QCD) has been constructed. The Standard Model is believed not to be the final answer–it still have some limitations and, for example, the gravitational interaction is not included in it because of the experimental difficulty due to the feeble magnitude of gravity. The Standard Model provides at least a full deck of cards to play with, and it is also believed that future developments shall be the extensions of the Standard Model, not contradiction.

The Standard Model consists of two major parts: the spin-1/2 fermions, and the integer-spin bosons as are listed in Table 1.1, and Table 1.2. As described in the model, all matter is built from the fermions: six *quarks* and six *leptons*. For example, the familiar nucleons, proton and neutron, are consist of the quarks **uud** and **udd**. These fermion constituents interact with each other by constantly exchanging specific boson mediators: the electromagnetic interaction between electrically charged particles is carried out by the exchanging of photons between them as an example.

The quarks possess color charges (red, green, and blue) and this degree of freedom is the necessity to take part in strong interaction just like the electric charge is needed for electromagnetic interaction. Although the quarks are convinced to be the fundamental constituents

Table 1.2: The boson mediators

Interaction	Mediator	Spin/parity
strong	gluon, G	1^-
electromagnetic	photon, γ	1^-
weak	$W^\pm$, Z^0	1^-, 1^+

Table 1.3: Example of hadrons

Hadron	Particle	Electric charge	Mass (MeV/c^2)	Spin/parity
Baryons	p (uud)	1	938.3	$\frac{1}{2}^+$
	$\bar{p}$ $(\bar{u}\bar{u}\bar{d})$	-1	938.3	$\frac{1}{2}^+$
	n (udd)	0	939.6	$\frac{1}{2}^+$
	λ (uds)	0	1115.7	$\frac{1}{2}^+$
	$\Lambda(1520)$ (uds)	0	1519.5	$\frac{3}{2}^-$
	$\Omega(sss)$	-1	1672.5	$\frac{3}{2}^+$
Mesons	π^+ $(u\bar{d})$	1	139.6	0^-
	π^- $(d\bar{u})$	-1	139.6	0^-
	π^0 $((u\bar{u}-d\bar{d})/\sqrt{2})$	0	135.0	0^-
	η $((u\bar{u}+d\bar{d})/\sqrt{2})$	0	547.5	0^-
	ρ $((u\bar{u}-d\bar{d})/\sqrt{2})$	0	768.5	1^-
	ω $((u\bar{u}+d\bar{d})/\sqrt{2})$	0	781.9	1^-
	ϕ $(s\bar{s})$	0	1019.4	1^-
	η_c $(c\bar{c})$	0	2979.8	0^-

of matter, they have not been observed directly. This phenomenon is referred to the property called color confinement–the naturally existing strongly interacting particles must be formed by quarks as a color singlet. The composites of quarks are therefore actually experimentally observed strong-interaction participants and are referred to as *hadrons*. The hadrons can be further classified in two groups: the baryons, fermions of three quarks composite, and the mesons, bosons of quark-antiquark pair. Some baryons and mesons are listed in Table 1.3 for example.

How the particles strongly interact with each other is to be given by QCD. QCD treats strong interaction in terms of quark and gluon degrees of freedom. In the extremely high energy regime, the *asymptotic freedom* of QCD allows to solve it perturbatively and QCD is well tested. Nevertheless, this perturbative QCD (pQCD) approach is not applicable in the relatively low energy region. Even though the QCD Lagrangian is know, it is difficult to solve analytically because of it's extreme nonlinearity. The only method which allows model-independent QCD calculation to be made from first principles, so-called Lattice QCD, has only recently produced promising results and is still limited by computer performance and other technical issues.

A more practical approach to the problems of physics of strong interactions is to make modifications like replacing quark and gluon degrees of freedom by nucleons and mesons, to construct models that emphasize the most important aspects of QCD, and to test them by confronting them with the experimental data. Therefore, experiments that test various QCD inspired models are essential in improving our knowledge of QCD in the non-perturbative regime.

1.3 Vector meson photoproduction

The photoproduction of light vector meson is of special interest for many reasons. It brings information on the dynamics of particle exchange, structure of baryon resonances, properties of VNN^* interactions, and possible manifestation of the so-called "missing resonances". The study of vector-meson photoproduction is an important subject of the experimental programs at photon and electron facilities such as Thomas Jefferson National Accelerator Facility, GRAAL

at Grenoble, ELSA-SAPHIR at Bonn, and LEPS at SPring-8.

1.3.1   Vector meson dominance model

With all the fundamental particles known, the photon provides unique opportunities for us to investigate the dynamics of the strong interaction between hadrons. Previous experimental results have shown that except for the difference in the magnitude of the cross sections, the real photon-hadron elastic and inelastic reactions behave very similarly to the corresponding hadron-hadron reactions [1]. But unlike the hadrons, the electromagnetic properties of the photon have been fully described by quantum electrodynamics. Thus, photon provides a clean initial state to deal with strong interaction.

Photon, as the force carrier of electromagnetic interaction, can itself turn into electron-positron pair via quantum fluctuation. When the energy of the photon goes up to GeV level, it would possess the ability to fluctuate into a quark and a anti-quark pair. Base on this concept of photon-hadron analogy, the vector meson dominance (VMD) model of photon-hadron interaction is formulated.

As illustrated in Fig. 1.1, the basic vector meson dominance model assumes that photons, real or virtual, interact with hadrons by first changing into neutral vector mesons having the same quantum number with photon ($J^{PC} = 1^{--}$), such as ρ ($u\bar{u} - d\bar{d}/\sqrt{2}$), ω ($u\bar{u} + d\bar{d}/\sqrt{2}$), ϕ ($s\bar{s}$), etc. Sure, this model doesn't provide special insight into the strong interaction; it transfers the photon-hadron-interaction study into a hadron-hadron one. But VMD is rather useful because a fairly specific scheme is provided in this model.
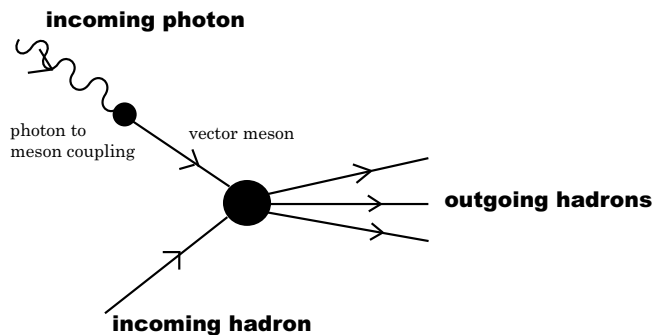
Figure 1.1: The vector meson dominance model for photon-hadron interactions.

Vector-meson photoproduction with small four-momentum transfer squared has originally been described within this VMD model. In this diffractive scattering case, mechanism responsible for the particle interaction should be under non-perturbative regime of QCD. Various interaction mechanisms are subsequently discussed.

1.3.2   Production mechanism

Diffractive hadron-hadron scattering can be described within Regge theory. Regge theory which is formulated in the nineteen-sixties is a pre-QCD approach based on general analyticity and crossing properties of scattering amplitudes [2, 3]. And it is found subsequently that QCD perturbation theory can be organized following the general concepts of Regge theory.

In Regge theory, the exchange of particles in the t-channel is summed coherently to give the exchange of so-called "Regge trajectories". Diffractive scattering is characterized by the exchange of the "Pomeron" trajectory which corresponds to the rightmost singularity in the

complex angular momentum plane and has the quantum numbers of the vacuum. But Regge theory cannot predict if the Pomeron is a single Regge pole along, consists of two Regge poles, and so on.

Although being unobserved, Pomeron trajectory may be identified with a glueball trajectory since the first particle state on the trajectory appears at $m^2 \simeq 4$ GeV^2 with quantum number $J^{PC} = 2^{++}$. Pomeron exchange describes extremely well hadron-hadron interaction in non-perturbative region at high energy. At large momentum transfer, this regime of Pomerons interacting with nucleons must be replaced by gluons interacting with quarks [4]. Attempts on developing an understanding of Pomeron exchange in terms of the quark and gluon degrees of freedom of QCD are also been made, such as discussed in [5].

According to Regge phenomenology, only the exchanging particles that have vacuum quantum numbers would give no vanishing contribution to total cross section with increasing energy. The Pomeron-exchange therefore dominates in the high energy region and give good description for this reason. At low energies however, other contributions such as π-, η-meson exchange would arise and may become detectable.

1.4   φ-meson photoproduction near production threshold

Diffractive photoproduction of $\phi(1020)$-meson near threshold plays a special role in studying the particle exchanging channels of hadronic interaction.

Due to the $s\bar{s}$ valence quark content of ϕ, the common baryon- and meson-exchange amplitudes in the s- and t-channels are first-orderly suppressed by the Okubo-Zweig-Iizuka (OZI) rule. As a consequence, primarily through Pomeron exchange does the scattering take place. Therefore, ϕ photoproduction is commonly utilized as a tool to study the Pomeron exchange dynamics.

At the low-energies of few GeVs, the contribution from Pomeron exchange drops because of the positive power-law scaling of center-of-mass energy property of Pomeron exchange. On the contrary, conventional pseudo-scalar π-, η-meson exchange channel of negative power-law scaling of center-of-mass energy squared can still make significant contribution even they are OZI suppressed.
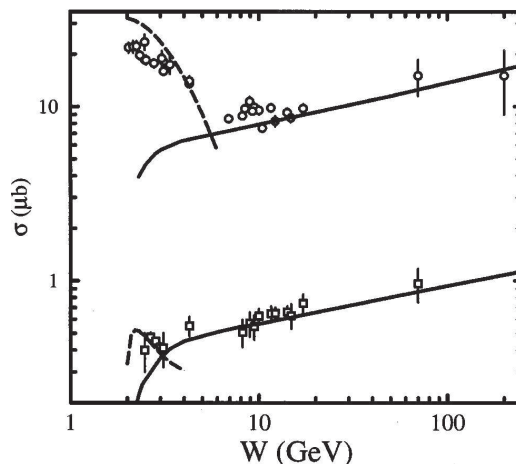
Figure 1.2: Energy dependence of ρ- (top) and ϕ-meson (bottom) photoproduction cross sections [5].

Fig. 1.2 taken from [5] shows the total cross section of ρ (top) and ϕ (bottom) photoproduction as a function of the center-of-mass energy W. The predictions from the Pomeron exchange

are represented by solid curves and the dashed curves are the predictions from meson-exchange. It can be seen that at the Pomeron-exchange-dominating high energies, the cross section increases slowly with increasing energy, and this behavior is shown for both ρ and ϕ photo production. In contrast to this similar trend at high energies, the cross section near threshold behaves differently; In ρ photoproduction, the cross section rises due to dominate contribution from meson exchange. The cross section, however, is not significantly enhanced in the ϕ photoproduction, which is a consequence of the suppression of meson-exchange contribution.

This suppression of dominating meson-exchange near threshold energy gives opportunity to study the property of additional "exotic" trajectories that may be manifested in this low energy region which is not able to be visible in ρ and ω production.

Possible candidates for these trajectories are discussed in many theoretical works, such as scalar meson [6], f_2' tensor meson [7], daughter Pomeron (P_2) inspired by the $J^{PC} = 0^{++}$ glueball predicted by the lattice QCD calculation and dual Ginsburg-Landau model [8, 9], direct $s\bar{s}$ knock-out of the strangeness sea in a nucleon [10], or other exotic channels. These exotic channels make contributions at forward production angles dominantly and decrease rapidly with the increase of incident photon energy. Since the contribution from the Pomeron exchange does not depend strongly on photon energy as predicted in Regge theory, the presence of new mechanics which may not seen at high energies can be uniquely studied. For that relative contributions from these additional channels cannot be well defined within the Regge theory and need to be determined from experimental data. In Fig. 1.3 [11] for example, prediction considering contribution from standard Pomeron (P_1), daughter Pomeron (P_2), π and η, and ϕ radiation is illustrated.
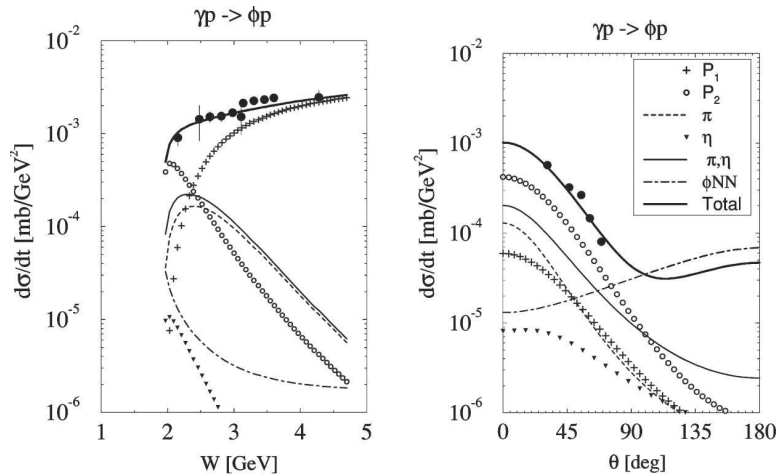
Figure 1.3: Differential cross section for $\gamma\, p \to \phi\, p$ reaction at $\theta = 0$ as a function of W (left) and θ at $E_\gamma = 2$ GeV (right) [11].

1.4.1   Liquid deuterium target

The ϕ-meson photoproduction with liquid hydrogen (LH$_2$) target are investigated in previous experiments such as [12, 13, 14, 15]. Rather than the simple mechanism of photon interacting only with proton by using LH$_2$ target, the liquid deuterium (LD$_2$) provided the chance to retrieve more information of the particle-exchange processes.

The deuteron consists of only a proton and a neutron and this configuration makes itself the simplest of all the nucleon bound states, and the nuclear structure and medium effects are therefore to be best controlled. The π^0 and η photoproduction from the deuteron are studied

previously in [16] and [17]. Now with the virtue of ϕ photoproduction discussed in section 1.4, the particle-exchange dynamics can be investigated more directly.

1.4.2 Incoherent and coherent interaction

There are two kinds of schemes for interaction with deuteron. One is the quasi-elastic scattering or **incoherent scattering** in which reaction the deuteron breaks up to be a proton and a neutron in the final state ($\gamma + d \rightarrow \phi + pn$). The other one that the deuteron remains intact is the **coherent scattering** ($\gamma + d \rightarrow \phi + d$).

The isovector π- and isoscalar η-meson exchange are primary components of meson-exchange channel. Since the deuteron is an isoscalar nucleon, t-channel isovector exchange would be eliminated from possible reaction diagrams in the coherent ϕ photoproduction on deuteron due to isospin conservation, which means that the π exchange contribution is excluded in the reaction process. Therefore, by comparing cross sections between the coherent ϕ production on deuteron and ϕ production on proton, the isovector exchange contribution in the ϕ photoproduction will be identified and it will also allow the extraction of the contribution from the isoscalar part of the production process.

Moreover, π- and η-exchange are both unnatural-parity processes while π-exchange contribution is relatively dominate among them, which can be seen in Fig. 1.3. The coherent ϕ photoproduction among which π-exchanged is removed is expected to be through processes of mostly positive-parity exchange, e.g. Pomeron exchange, as can be seen in 1.4 taken from [18]. In this case, the differential cross section at zero degree which is well described by standard Pomeron trajectory at high energies can be utilized as a benchmark of positive-parity exchange processes. Taking the form factor of deuteron into account, any deviation from the standard Pomeron contribution would reveal the existence of any other process of natural-parity exchange, e.g. the glueball-inspired daughter Pomeron trajectory P_2.
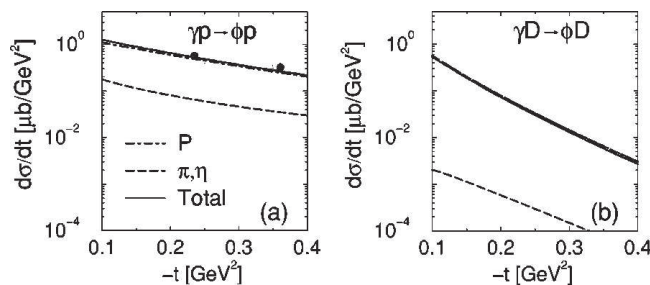
Figure 1.4: Differential cross sections for $\gamma + p \rightarrow \phi + p$ and $\gamma + d \rightarrow \phi + d$ reactions [18].

As shown in Fig. 1.4 taken from [18], although the coherent process would give significant contribution, the incoherent interaction $\gamma + d \rightarrow \phi + pn$ is considered to be dominant still in the ϕ photoproduction from deuterons. For the incoherent ϕ production interaction, the isotopic effect of nucleons can be investigated by comparing with results from existing proton target experiments [11].

In this thesis, the measurement of differential cross section of ϕ-meson photoproduction from liquid deuterium and liquid hydrogen targets is presented. Before this work, there was only one measurement of ϕ photoproduction from deuterons at $E_\gamma = 6.4$ - 9.0 GeV and no separation of coherent interaction from incoherent interaction was made [19]. This analysis is done not only to examine the previous non-monotonic increase of differential cross section with increasing photon energy from LEPS experiment shown in Fig. 1.5 [12], but hopefully to provide more insight into the issue of possible exotic particle-exchange channels. Certainly, measurement of
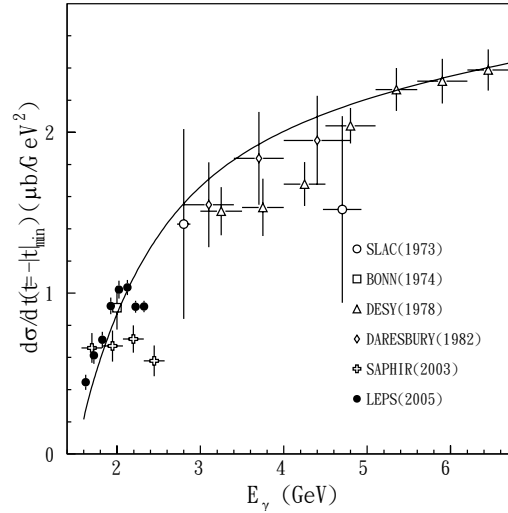
Figure 1.5: Energy dependence of $d\sigma/dt_{t=-|t|_{min}}$ [12].

the cross sections alone can not tell the answer explicitly while spin observables are demanded to provide more information to determine the contribution from different channels such as discussed in [6, 9, 10, 18]. And this can surely be achieved by utilizing the highly polarized photons produced at SPring-8/LEPS facility and the subsequent study on ϕ decay asymmetry Σ_ϕ, but this is beyond the coverage of this dissertation.

This thesis is organized as follows. In chapter 2, the LEPS experiment is introduced. The definitions, methods, and techniques used in the data analysis is discussed in chapter 3 followed by the results and discussion shown in chapter 4. Finally a summary is given in chapter 5.

Chapter 2

Experimental apparatus

The data for was taken at the laser-electron photon facility (LEPS) at SPring-8, Japan. At SPring-8 BL33LEP beamline (LEPS facility), the linearly-polarized photons were produced by Backward-Compton scattering and then conducted to irradiate the liquid hydrogen (LH_2) and the liquid deuterium (LD_2) target. The experimental apparatus of the measurement is described in this chapter.

2.1 SPring-8

In October 1984, the Institute of Physical and Chemical Research (RIKEN) in Japan planned the framework of the large synchrotron radiation (SR) facility for developing materials. Later in October, 1988 Japan Atomic Energy Research Institute (JAERI) and Riken established a collaborative team for the synchrotron radiation facility research and development. Until October 1997, SPring-8, an acronym of **S**uper **P**hoton **ring-8** GeV facility, was finally constructed and began to be utilized for research works.
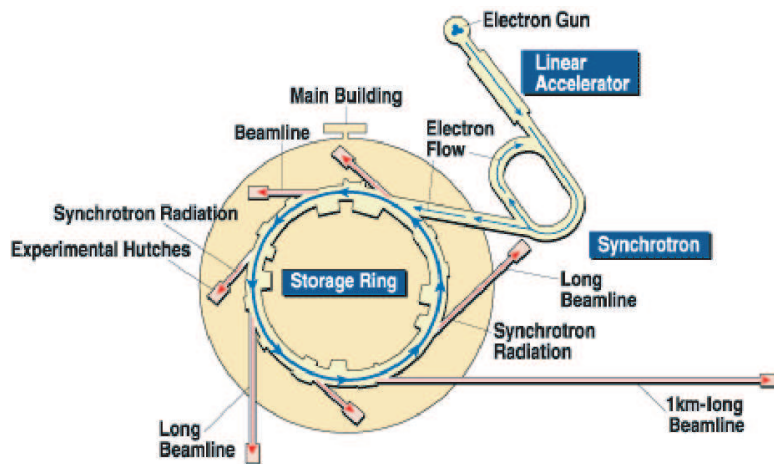
Figure 2.1: Main facilities of SPring-8.

Having the highest electron energy, the largest circumference, and the advanced insertion devices, the SPring-8 facility is the most powerful third-generation synchrotron radiation facility with 62 beamlines now. The main facilities of SPring-8 are shown in Fig 2.1. The electron beam is generated by a thermionic gun made of barium-impregnated tungsten and then be boosted by the 140 m linear accelerator (linac) up to 1 GeV. After that, the beam is transported to the

booster synchrotron of 396 m circumference to be further accelerated to 8 GeV. Finally, the beam is injected into the circular storage ring with energy maintained at 8 GeV.

2.2   Backward-Compton scattering

In 1963, Milburn, Arutyunain, and Tumanian proposed that photons produced by collisions of laser photons with high-energy electrons in the direction of the electrons would reach the same energy scale as the electron. This process is generally referred to as the Backward-Compton scattering (BCS) and the high-energy photons subsequently obtained are called laser-electron photons.
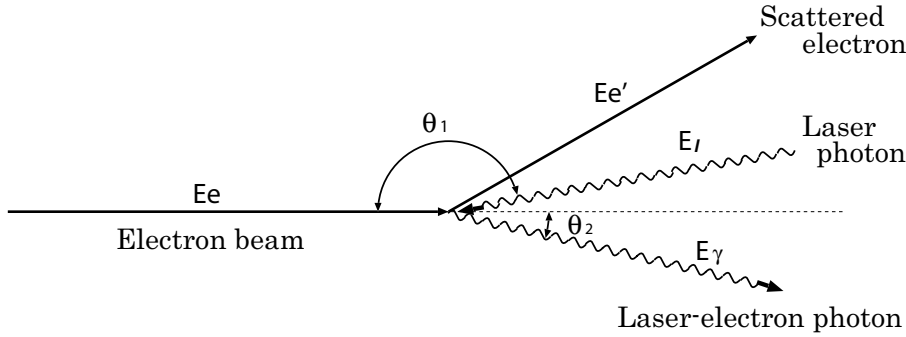
Figure 2.2: Backward Compton scattering process.

Fig 2.2 shows the BCS process. In Fig 2.2, the energy of the energy of the laser photon and the electron are E_l and E_e, θ_1 denotes the angle between the electron and the incident laser photon, and θ_2 denotes the angle between the electron and the scattered photon. The energy of the scattered photon is:

$$E_\gamma = \frac{E_l(1 - \beta \cdot \cos\theta_1)}{1 - \beta \cdot \cos\theta_2 + E_l[1 - \cos(\theta_2 - \theta_1)]/E_e} \tag{2.1}$$

From BCS, photons with energy up to a few GeV are therefore able to be produced by shooting a few eV photons to 8 GeV electrons.
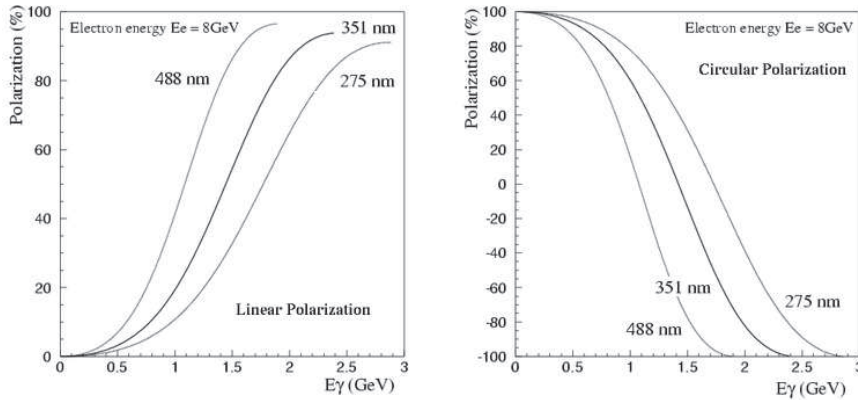
Figure 2.3: Polarization of laser electron photon.

The linear polarization of the photon beam can be easily achieved with polarized laser light. The BCS possesses the ability to preserve the polarization of incident photons, therefore if the

incident laser lights are to be 100 % polarized near the Compton edge, the backward-Compton-scattered photons are highly polarized at the maximum energy. The energy dependence of the polarization is shown in Fig. 2.3. As can be seen, the polarization drops as the photon energy decreases. However, the polarization state of interest can be obtained by changing the energy of laser photons and by handling the direction of the laser polarization.

2.3 Beamline

The Laser-electron photon facility was built at the beamline BL33LEP as shown in Fig. 2.4. The first LEPS beam was produced in 1999 and the first physics run started in 2000 for the quark nuclear physics studies afterwords.
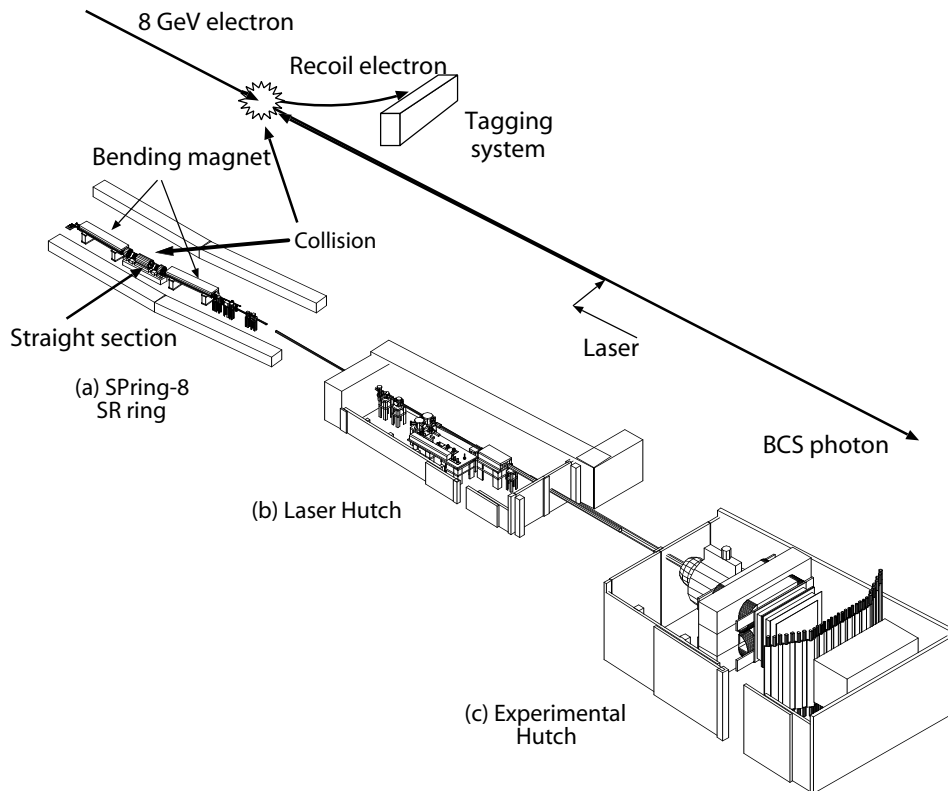
Figure 2.4: LEPS beamline.

The LEPS beamline has a 7.8 m-long straight section of the storage ring between two bending magnets. Polarized laser photons are injected from a laser hutch toward the straight section where BCS of the laser photons from the 8 GeV electron beam occurs. The produced BCS photons can reach the maximum energy of 2.4 GeV and are then transfered through the beam pipe to the experimental hutch 60 m downstream of the straight section where a target and a spectrometer are located.

2.4   The laser system

An Argon-ion laser is used as the photon source. The laser operated with a multi-line mode has the wave lengths ranging from 333.6 to 363.8 nm, which is in the ultraviolet region. The laser beam is almost 100 % polarized due to the property of the laser resonator. The intensity of the laser beam is about 2.5×10^6 photons per second and the typical power is about 5 W.

The emitted laser beam is enlarged by a beam expander and then directed to the storage ring by optical mirrors. The direction of the linear polarization of the laser beam is tuned to be either vertical or horizontal by using a half-wavelength plate. The polarization of the laser light is measured by a Glan-laser prism polarimeter and a photo diode placed at the end of the straight section to determine the polarization angle and degree.

2.5   The tagger

The energy of the BCS photons is determined by measuring the energy of the recoil electrons, which is $E_{e'}$ in Fig 2.2. According to the energy conservation, E_γ is obtained by $E_\gamma = E_e - E_{e'} + E_l$.
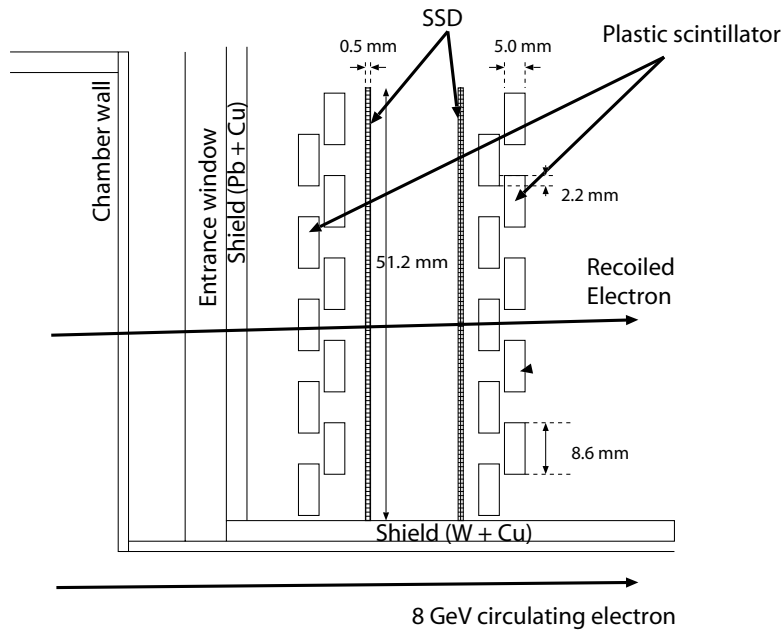
Figure 2.5: The tagging counter.

The recoiled electrons deviate the route of the circulating electrons in the storage ring because of energy loss in BCS. And this deviation is directly related to the corresponding energy of the electrons. The recoiled electrons are thus detected by the tagging system (tagger) located at the exit of the bending magnet of the storage ring next to the straight section. The schematic view of the tagging counter is shown in Fig 2.5.

The tagging counter consists of two layers of plastic scintillator hodoscopes and two silicon strip detectors (SSD). There are 10 segments of plastic scintillators which are 10 mm high, 8.6 mm wide, and 5 mm thick each, stacked with an overlap of 2.2 mm in one layer of the plastic scintillator hodoscope. The hodoscopes provide timing signals of the recoiled electrons and are used to reject accidental events. SSD consists of 512 readout strips with a 0.1 mm pitch.

Precise hit position of a recoiled electron is measured by the SSD strip and the photon energy is obtained.

With the tagging counter, the photon energy coverage is from 1.5 to 2.4 GeV.

2.6 The charged particle spectrometer

A 160 mm-long liquid hydrogen and a 160 mm-long liquid deuterium target were used in the experiment. They were placed in copper cells with a trapezoid shape which was designed not to cause influence on the acceptance of the charged particle spectrometer. The entrance and exit windows of the target cell were made of Aramid foils with thickness of 0.05 mm. The target cell was located right upstream of the charged particle spectrometer as shown in Fig 2.6.
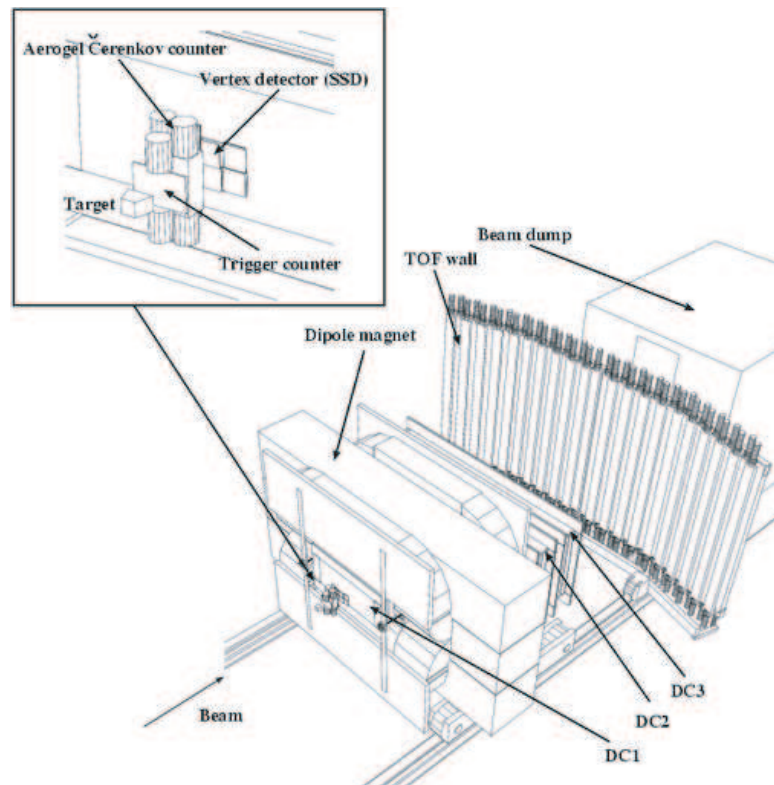
Figure 2.6: The LEPS charged particle spectrometer.

The charged particle spectrometer designed to detect charged hadrons produced at forward angles consisted of an upstream veto counter, a start (trigger) counter (SC), a silica-aerogel Čerenkov counter (AC), a silicon vertex detector (SVTX), a dipole magnet, three multiwire drift chambers (DC1, DC2, and DC3), and a time-of-flight (TOF) wall. The dipole magnet provided the magnetic field of maximum 0.7 T at its center for momentum measurement. The dipole-magnet aperture was 55 cm high and 135 cm wide. The length of the pole along the beam direction was 60 cm. The angular coverage of the spectrometer was about ±0.2 rad and ±0.4 rad in the vertical and horizontal directions.

The upstream veto counter just before the target was a plastic scintillation counter with a thickness of 5 mm, 200 mm high, and 190 mm wide. This veto counter was placed to eliminate the charged particles produced upstream, such as by photons interacting with residual gas in the vacuum beam pipe.

The SC located right behind the target is a 5 mm thick plastic scintillator. It provides the start timing of the trigger of data acquisition system. The silica-aerogel Čerenkov counter located downstream of the start counter had a 60-mm silica-aerogel radiator with a refractive index 1.03 to veto the main e^+e^- pair production background. The Čerenkov threshold momentum for electron, pion, and kaon were 0.002 GeV, 0.57 GeV, and 2.0 GeV respectively. The efficiency of the Čerenkov counter to reject the was higher than 99.9 %.

The silicon vertex detector and three drift chambers were the tracking detectors. SVTX located behind AC was a silicon strip detector with 0.12 mm strip pitch. Half of the strip was placed in vertical direction and the other half in horizontal direction to measure the vertex positions in each direction. By the SVTX, precise vertex positions were obtained.

The drift chambers placed upstream of the dipole magnet (DC1) consisted of 6 layers. Three of the layers are for the vertical direction (x-direction), two are for the +45°and one for the -45°direction with respect to the vertical direction. The wire spacing of DC1 sense wires was 12 mm. The other two drift chambers, DC2 and DC3, were located downstream of the magnet and had 5 layers: two vertical, two at +30°, and one at -30°. The spacing of the sense wires was 20 mm for both DC2 and DC3. The field wires were arranged in a hexagonal shape for all three drift chambers. The active area is 30 cm high × 60 cm wide for DC1 and 80 cm high × 200 cm wide for DC2 and DC3. The efficiency of each layer was about 99 % and the position resolution is about 200 μm.

The TOF wall is positioned downstream of the DC3. It consists of an array of 40 plastic scintillators. Each scintillator counter as 12 cm wide, 4 cm thick, and 200 cm high and is arranged to have a 1 cm overlap with each other. The stop signal for the time-of-flight measurement is provided by the TOF counters and the typical time resolution of the TOF counters was 120 ps. The time-of-flight of the charged particle is thus determined by the start timing signal obtained from the RF signal of the accelerator or from SC, and the stop signal from TOF counters.

Chapter 3

Basic definitions and data analysis

In this chapter, the basics definitions used in the analysis are introduced. The analysis of the LD$_2$ coherent reaction $\gamma + d \rightarrow \phi + d$ and LD$_2$ incoherent reaction $\gamma + d \rightarrow \phi + pn$ are presented with LH$_2$ reaction $\gamma + p \rightarrow \phi + p$ as a contrast.

3.1 Basic definitions

3.1.1 Invariant mass and missing mass

Invariant mass and missing mass are both frequently used physical quantities to identify particles based on energy-momentum conservation. Assume a two body reaction as:

$$p_{initial\mathbf{1}} + p_{initial\mathbf{2}} \rightarrow p_{final} + p_{missing} \rightarrow p_{daughter\mathbf{1}} + p_{daughter\mathbf{2}} + ... + p_{daughter\mathbf{N}} + p_{missing}.$$

The reaction of the two initial particles $p_{initial\mathbf{1}}$ and $p_{initial\mathbf{2}}$ produces p_{final} and $p_{missing}$. The particle p_{final} further decays into **N** secondary particles $p_{daughter\mathbf{1}}$, $p_{daughter\mathbf{2}}$, ..., and $p_{daughter\mathbf{N}}$, as shown in Fig. 3.1. These secondary particles are detected by the detector while the so-called "missing" particle $p_{missing}$ is not.
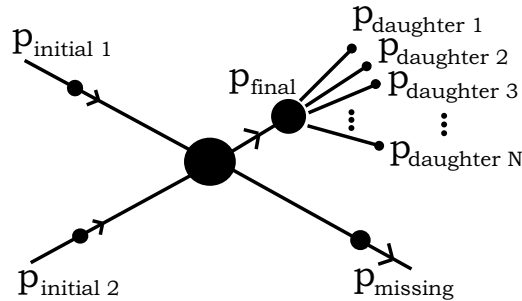
Figure 3.1: Two body reaction followed with the decay.

Define the four-momentum of each particle as capital P and let $P_{initial} = P_{initial\mathbf{1}} + P_{initial\mathbf{2}}$ denotes the total four-momentum in the initial state. By energy-momentum conservation, the relation between these four-momentums goes:

$$P_{initial} = P_{final} + P_{missing},$$
$$P_{final} = P_{daughter\mathbf{1}} + P_{daughter\mathbf{2}} + ... + P_{daughter\mathbf{N}}.$$

The invariant mass M_{inv} of the particle p_{final} and missing mass M_{mis} of the particle $p_{missing}$ then are evaluated as:

$$M_{inv} = \sqrt{(P_{final})^2} = \sqrt{(P_{daughter1} + P_{daughter2} + ... + P_{daughterN})^2}, \qquad (3.1)$$

$$M_{mis} = \sqrt{(P_{initial} - P_{final})^2}. \qquad (3.2)$$

As can be seen in the equation above, when the mother particle is difficult to detect (electrically neutral, life time too short,etc.), invariant mass can be helpful to reconstruct the mass of the mother particle by the detectable decay produced daughters. And missing mass is a tool to identify the undetected particle when a reaction takes place by all the other particles relating to the reaction. Certainly, the missing mass approach can be applied to situation of more than one missing particle.

It is noted that unlike the invariant mass which can be evaluated solely by the four-momentum information of particles produced after the reaction, the missing mass needs both the four-momentum of the particles before and after the reaction. In the case of the reaction with deuteron $\gamma + d \rightarrow \phi + X$, the incident photon interacts with the individual nucleon and the deuteron may break up in incoherent interaction or remain as a whole in coherent interaction. That is, as represented as the formulation above, if $P_{initial1}$ is the four-momentum of the photon P_γ, $P_{initial2}$ can be the four-momentum of the nucleon P_N or the deuteron P_d.

Neglect the mass difference between the proton and the neutron and assume the kinematic behavior of these two nucleons are equivalent when bound as a deuteron, the missing mass evaluated with incoherent mechanics (nucleon target assumed) is denoted as $\mathbf{MM}_p$ and the missing mass evaluated with coherent mechanics (deuteron target assumed) is referred to as $\mathbf{MM}_d$ hereafter.

3.1.2 Mandelstam variables

The Mandelstam variables are Lorentz-invariant variables used to describe the kinematics of particle reactions, in the usual case, of two particles going to two particles. The cross-section may be succinctly expressed in terms of these variables.

Definition of Mandelstam variables s, t, and u

For the reaction of a incident photon and a initial hadron producing a ϕ-meson and a final hadron, $\gamma + h \rightarrow \phi + h'$, define the four-momentum of the incident photon, ϕ, initial hadron, and final hadron as k, q, P,and P' as is shown in Fig. 3.2
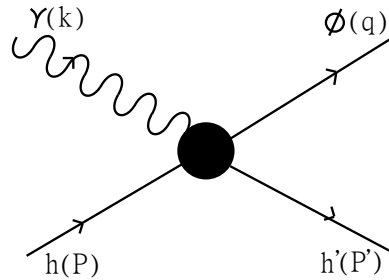
Figure 3.2: $\gamma + h \rightarrow \phi + h'$ process.

The conservation of four-momentum gives:

$$k + P = q + P'.$$

The Mandelstam variables then can be written as follows:

$$s = (k + P)^2 = (q + P')^2, \tag{3.3}$$
$$t = (k - q)^2 = (P' - P)^2, \tag{3.4}$$
$$u = (k - P')^2 = (q - P)^2. \tag{3.5}$$

From which it follows that:

$$s + t + u = \sum_{i=1}^{4} m_i^2. \tag{3.6}$$

The sum of the Mandelstam variables is equal to the sum of the mass square of the particles involved.

From the definitions above, it follows that s is equivalent to the square of the centre-of-mass energy squared of the reaction, t corresponds to the four-momentum transfer squared, and u the crossed four-momentum transfered.
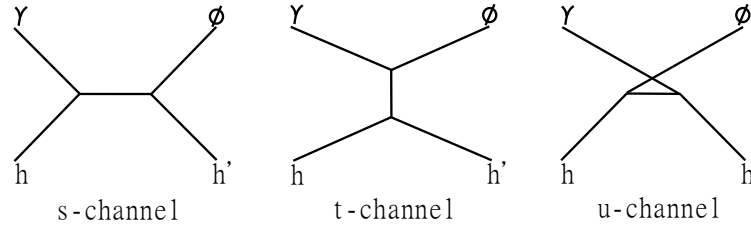
Figure 3.3: Different reaction channels.

These three Mandelstam variables are also used in terms s-channel, t-channel, and u-channel. These channels represent different Feynman diagrams or different possible scattering events and are defined as whether the four-momentum squared of the intermediate particle being exchanged in the interaction equals s, t, or u. The three different channels are shown in Fig. 3.3

More about the t variable

More details of the t of the $\gamma + p \rightarrow \phi + X$ mechanism need to be discussed because of its specialty in the evaluation of $d\sigma/dt$ of incoherent and coherent reaction. First, as is shown in the left plot of Fig. 3.4, define the four-momentum of the incident photon and the initial hadron in the lab.system in explicit form as:

$$k = (E_\gamma, 0, 0, E_\gamma),$$
$$P = (E_h, 0, 0, 0),$$

where the velocity of light c is set to one (which is also the case in the following analysis), the direction of the incident photon is assumed to be aligned to the z direction, and the momentum of the initial hadron is presumed to be negligible. The s variable evaluated by the variables in the lab. system is thus evaluated as:

$$s = (k + P)^2 = ((E_\gamma + m_h)^2 - E_\gamma)^2. \tag{3.7}$$

In the centre-of-mass system (c.m.s.), the four-momentum of these four particles are ex-
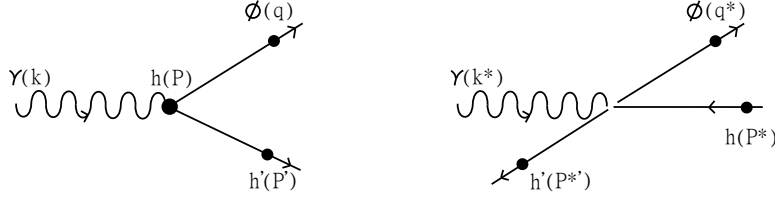
Figure 3.4: $\gamma + h \rightarrow \phi + h'$ process in lab. system and in c.m.s.

pressed with an asterisk added as is shown in the right plot of Fig. 3.4:

$$k^* = (E_\gamma^*, \mathbf{p}_\gamma^*) = (\sqrt{m_\gamma^2 + |\mathbf{p}_\gamma^*|^2}, \mathbf{p}_\gamma^*),$$

$$P^* = (E_h^*, \mathbf{p_h^*}) = (\sqrt{m_h^2 + |\mathbf{p_h^*}|^2}, \mathbf{p_h^*}),$$

$$q^* = (E_\phi^*, \mathbf{p}_\phi^*) = (\sqrt{m_\phi^2 + |\mathbf{p}_\phi^*|^2}, \mathbf{p}_\phi^*),$$

$$P'^* = (E_{h'}^*, \mathbf{p_{h'}^*}) = (\sqrt{m_{h'}^2 + |\mathbf{p_{h'}^*}|^2}, \mathbf{p_{h'}^*}),$$

and note that in c.m.s., $\mathbf{p}_\gamma^* = -\mathbf{p_h^*}$ and $\mathbf{p}_\phi^* = -\mathbf{p_{h'}^*}$. The s variable evaluated in c.m.s. using k^* and P^* is therefore:

$$s = (k^* + P^*)^2 = (\sqrt{m_\gamma^2 + |\mathbf{p}_\gamma^*|^2} + \sqrt{m_h^2 + |\mathbf{p}_\gamma^*|^2})^2.$$

The magnitude of the momentum of the photon can then be deduced:

$$|\mathbf{p}_\gamma^*| = \frac{\sqrt{s^2 + m_\gamma^4 + m_h^4 - 2sm_\gamma^2 - 2sm_h^2 - 2m_\gamma^2 m_h^2}}{2\sqrt{s}}. \tag{3.8}$$

And the magnitude of the momentum of the ϕ-meson can be obtained in the same way:

$$|\mathbf{p}_\phi^*| = \frac{\sqrt{s^2 + m_\phi^4 + m_{h'}^4 - 2sm_\phi^2 - 2sm_{h'}^2 - 2m_\phi^2 m_{h'}^2}}{2\sqrt{s}}. \tag{3.9}$$

The t variable in c.m.s. is:

$$t = (k^* - q^*)^2 = (E_\gamma^* - E_\phi^*)^2 - (\mathbf{p}_\gamma^* - \mathbf{p}_\phi^*)^2$$
$$= (\frac{m_\gamma^2 - m_h^2 - m_\phi^2 + m_{h'}^2}{2\sqrt{s}})^2 - (\mathbf{p}_\gamma^* - \mathbf{p}_\phi^*)^2, \tag{3.10}$$

The value of $|t|$ thus have minimum when $\mathbf{p}_\gamma^*$ and $\mathbf{p}_\phi^*$ are parallel, maximum when $\mathbf{p}_\gamma^*$ and $\mathbf{p}_\phi^*$ are anti-parallel. This minimum and maximum value are denoted as $|t|_{min}$ and $|t|_{max}$ separately. By Eq. 3.10, these two values can be written as:

$$|t|_{min} = -(\frac{m_\gamma^2 - m_h^2 - m_\phi^2 + m_{h'}^2}{2\sqrt{s}})^2 + (|\mathbf{p}_\gamma^*| - |\mathbf{p}_\phi^*|)^2, \tag{3.11}$$

$$|t|_{max} = -(\frac{m_\gamma^2 - m_h^2 - m_\phi^2 + m_{h'}^2}{2\sqrt{s}})^2 + (|\mathbf{p}_\gamma^*| + |\mathbf{p}_\phi^*|)^2. \tag{3.12}$$

Putting Eq. 3.7, 3.8, 3.9, 3.11, and 3.12 all together, using the Lorentz-invariant property of s in the lab. system and c.m.s., it is shown that the value of $|t|_{min}$ and $|t|_{max}$ are coupled with

the masses of the particles involved in the reaction and the photon energy in the lab. system, $E\gamma$. For the incoherent-reaction case $\gamma + d \rightarrow \phi + pn$, the mass of the hadron m_h and $m_{h'}$ should be taken as the mass of proton m_p (neglect the mass difference of proton and neutron), and for the coherent-interaction case $\gamma + d \rightarrow \phi + d$, m_h and $m_{h'}$ should be taken as the mass of deuteron m_d. The minimum and maximum value of $|t|$ of these two kinds of reaction mechanism is denoted as $-|\mathbf{t}|^{\mathbf{p}}_{\mathbf{min}}$, $-|\mathbf{t}|^{\mathbf{p}}_{\mathbf{max}}$, $-|\mathbf{t}|^{\mathbf{d}}_{\mathbf{min}}$, and $-|\mathbf{t}|^{\mathbf{d}}_{\mathbf{max}}$.

With the masses of the particles involved in the interaction determined, the only parameter left is $E\gamma$. Take incoherent interaction as an example, with a specific E_γ, the allowed phase space of t is defined by $-|t|^p_{min}$ and $-|t|^p_{max}$ as is shown in Fig. 3.5. As can be seen in Fig. 3.5, the phase space of t shrinks as E_γ goes down and exhibits a singularity around $E_\gamma = 1.57$ GeV.
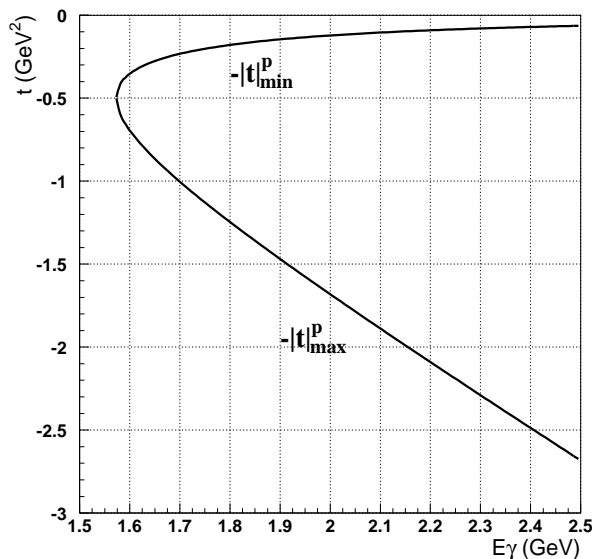
Figure 3.5: Phase space of t as a function of E_γ.

The value of $-|t|^p_{min}$ and $-|t|^d_{min}$ as a function of E_γ is shown in Fig. 3.6 as solid line and dash line separately. The figure indicates that the value of $-|t|^d_{min}$ is greater than $-|t|^p_{min}$ and the difference of $-|t|^p_{min}$ and $-|t|^d_{min}$ rise up as E_γ goes down. This inconsistency is of rather importance in evaluating $d\sigma/dt$ as will be discussed in the subsequent analysis.

3.1.3 Production threshold of ϕ

The energy threshold of E_γ to produce ϕ is evaluated as follows. Using the reaction $\gamma + h \rightarrow \phi + h'$ and the conservation of four-momentum, in the case that E_γ is just at the production threshold, it follows that:

$$(E_{\gamma-threshold} + m_h)^2 - (E_{\gamma-threshold})^2 = (m_\phi + m_h)^2.$$

The threshold value of E_γ is then:

$$E_{\gamma-threshold} = m_\phi + \frac{m_\phi^2}{2m_h}. \tag{3.13}$$

Just like the situation in evaluating $|t|_{min}$, the m_h can be m_p or m_d. $E_{\gamma-threshold}$ is then about 1.573 GeV for incoherent case and 1.296 GeV for coherent case. But 1.296 GeV of the coherent

Figure 3.6: $-|t|^p_{min}$ and $-|t|^d_{min}$ as a function of E_γ.
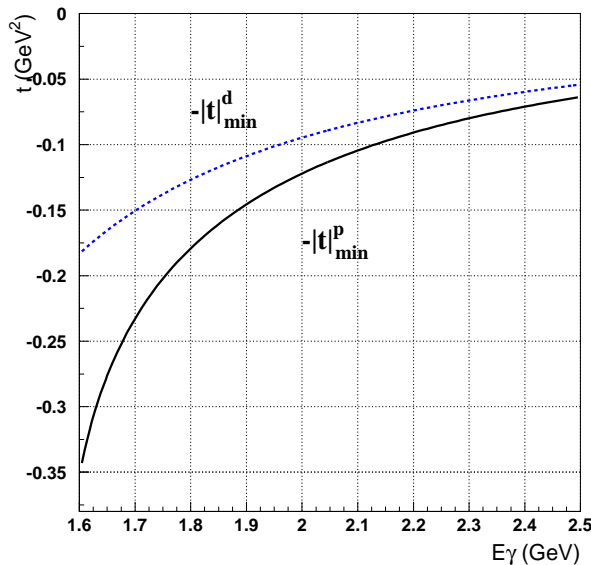
case is not in the accepted E_γ range in the experiment, the production threshold in this analysis is therefore refer to 1.573 GeV only. As can be found here that this threshold energy 1.573 GeV of incoherent process corresponds to the phase space singularity of t mentioned in the previous subsection.

3.2 Monte Carlo simulation

The Mote Carlo simulation is the computer-based simulation used to reconstruct the experimental actualities.

The Monte Carlo simulator for the LEPS spectrometer, **g3leps** is developed based on the CERN program library, GEANT. With the necessary information implemented, the g3leps simulates the generation of the ϕ photoproduction events, the subsequent process during the passing of the particles through the experimental apparatus such as particle decay or multiple scattering. The responses of the detectors like the measured resolution and the efficiency of the detectors are also described.

The Monte Carlo event generator generates possible physical events. The ϕ-meson event generator is utilized to generate ϕ photon production of incoherent reaction on deuteron $\gamma + d \rightarrow \phi + pn$, coherent reaction on deuteron $\gamma + d \rightarrow \phi + d$, and on proton $\gamma + p \rightarrow \phi + p$ with $\phi \rightarrow K^+ K^-$. The event generation is not model-independent and dynamical information of ϕ-meson generation should be pre-defined before generation with user-defined parameterization. The disentangling of convoluted coherent and incoherent events and the acceptance of different reaction mechanism are studied by this Monte Carlo simulator. For the study of the backgrounds, various background-event generation is also done by using other background-event generators.

The Monte Carlo simulation plays an important role in this analysis because the disentangling of coherent and incoherent events strongly depends on it. Different tests and attempts on reliable Monte Carlo simulation are therefore made as will be discussed in the following

sections. And in the following analysis, identical analysis treatment is performed on both the data from Monte Carlo simulation and the real data to ensure the fairness of the reproducibility of Monte Carlo simulation.

3.3 Event selections

The data samples used in the analysis are:

- **LH$_2$ target runs**:
  r23690 (2002.05.23) - r24058 (2002.07.09)
  r25453 (2003.02.27) - r25968 (2003.04.14)

- **LD$_2$ target runs**:
  r24095 (2002.10.18) - r24841 (2002.12.18)
  r25015 (2003.01.30) - r25447 (2003.02.21)
  r26001 (2003.04.20) - r26338 (2003.06.02)

This raw experimental data is first pre-analyzed by the LEPSana offline analysis program. The LEPSana performs necessary calibrations on the raw data and then output the refined data in Ntuple format which can then be accessed by the Physics Analysis Workstation (**PAW**) system [20] to be further analyzed.

This study focus on the reaction, $\gamma + d \to \phi + X$, followed by the ϕ-meson decay, $\phi \to K^+K^-$, with the branching ratio (49.1±0.6) [21]. The presence of K^+K^- mesons are therefore used to identify the photoproduction of ϕ mesons. There are four kinds of event topology based on the detected particles: K^+K^- mode, K^+p mode, K^-p mode, K^+K^-p mode. In the K^+p and the K^-p mode, there is significant background involvement from hyperon decays such as:

$$\gamma + p \to K^+ + \Lambda \to K^+ + p + \pi^-,$$
$$\gamma + p \to K^+ + \Sigma^0 \to K^+ + \Lambda + \gamma \to K^+ + p + \pi^- + \gamma.$$

And the K^+K^-p mode is relatively poor in statistics due to the low probability of the exclusive measurement of all three particles. The most important of all, the coherent interaction would be excluded in other three modes and it is therefore that K^+K^- mode is used for this analysis. The definitions of the selection cuts are described in this section.

3.3.1 The track selection cut

To ensure that it is K^+K^- mode to be studied, the tracks of K^+K^- has to be confirmed and the events with p track contained has to be excluded. The cuts to select "correct" and "good" tracks is explained as follows.

Decay-in-flight cut

The cuts used to reject decay-in-flight tracks are:

- **TOF hit**: $ithtofhit > 0$
  The TOF counter must have more than a hit registered.

- **Difference between reconstructed track and measured track at TOF counter**:
  $| ytof - tofdiff | < 80, | itof - tofid | < 2$
  The difference between the reconstructed and the measured y position is required to be within 80 mm and the difference of the TOF slat number must less than 2.

- **Number of outliers**: $noutl < 7$
  The outliers are the hits of tracking chambers that deviate from the expected trajectories more than the resolution. The outliers are removed from the tracking and the number of the outliers to be less than 7 is required for the track to be accepted.

- **χ^2 probability**: $probchi2 > 0.02$
  The χ^2 probability of the reconstructed track must greater than 0.02.

$K^+ K^-$ identification

The particle identification (PID) is done by the standard procedure as is used in [22], [23]. Using the information of the time of flight and momentum, the mass distribution is obtained. Fig. 3.7 shows distribution of mass square versus momentum for LD_2 data set for example. Band structure consisted of different particles are shown. By setting cut points on this distribution of mass square versus momentum, the tracks of different particles are identified and separated out. The two-track events with identified K^+ and K^- tracks are accepted.
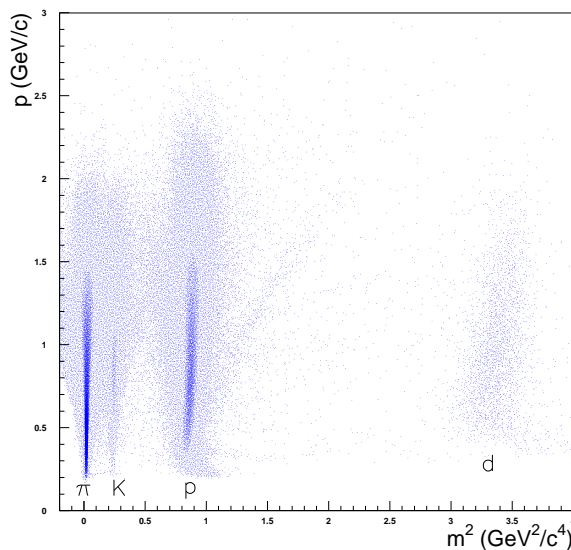
Figure 3.7: Scatter plot of mass square and momentum of LD_2 .

3.3.2 The vertex cut

The life time τ of ϕ-meson is extremely short, which means that once the ϕ-meson is produced, it decays into $K^+ K^-$ in no time. Therefore the distribution of the position of the reconstructed vertex points of the $K^+ K^-$ tracks should be around the target cell to ensure the $K^+ K^-$ mesons come from the reactions at the target, not at the start counter or the target holder. The cuts, -1070 mm < z-coordinate < -920 mm, -15 mm < x-coordinate < 15 mm, and -15 mm < y-coordinate < 15 mm are then applied. Fig. 3.8 shows the vertex cut in different coordinates of LD_2 target events as an illustration.
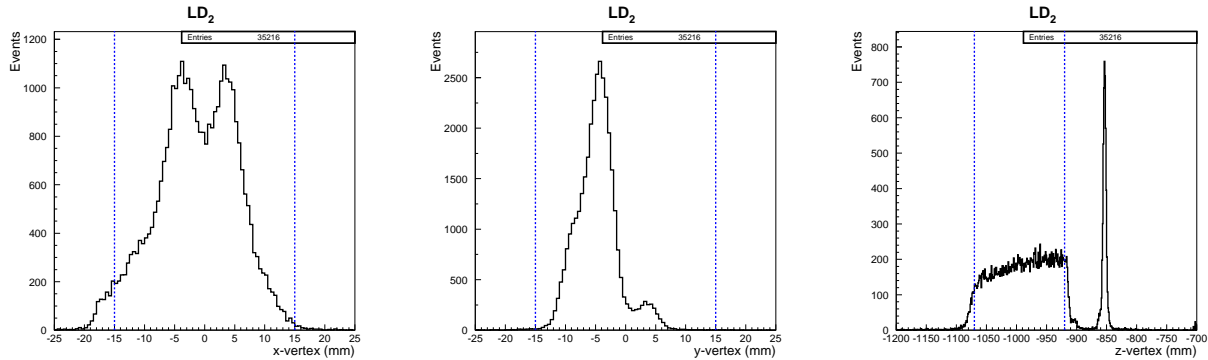
Figure 3.8: Cuts on position of vertex.

3.3.3 The tagger hit cut and E_γ selection

The incident photon energy is obtained by analyzing the tagger signals and the number of valid tagger hits is registered as *ntag*. It is found that there are events that contain non-valid tagger hits ($ntag = 0$) as is shown in Fig. 3.9
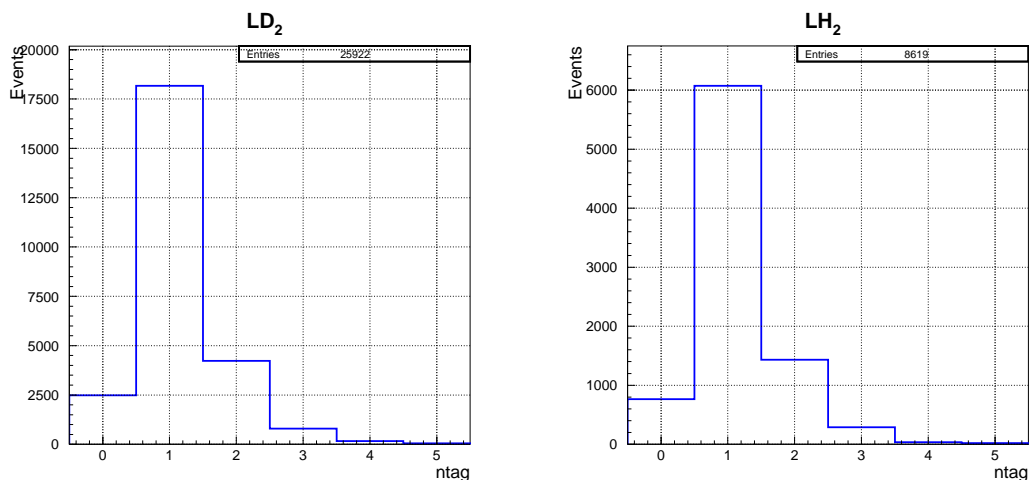
Figure 3.9: Number of valid tagger hits of LD_2 target events (left) and LH_2 target events (right).

Usually, the number of tagger hits is required to be non-zero in order to determine the incident photon energy. As can be seen in Fig. 3.9, there are events with $ntag > 1$. The additional tagger hits may come from electronic noises originate from Bremsstrahlung light emitted by electrons in the storage ring or off-timing accidental hits by electrons scattered by the interaction with the laser photon. To deal with these $ntag > 1$ events, a treatment based on energy-momentum conservation is applied to select one of the tagger hits.

Take the notation of the four-momentum defined in section 3.1.2 to label the four-momentum of the particles. By the relation of energy-momentum conservation, the predicted photon energy E_γ^{pred} is evaluated as:

$$E_\gamma^{pred} = \frac{2E \cdot m_p - m_\phi^2}{2(m_p - E_\phi + p_{\phi z})}. \tag{3.14}$$

The measured value E_γ that has the closest value to E_γ^{pred} is selected to be the energy of the

incident photon.

It need to be mentioned that Eq. 3.14 is derived by assuming $\gamma + p \rightarrow \phi + p$ interaction, and thus the applicability of E_γ^{pred} with LD$_2$ events is questionable. Further, this method is convoluted with the momentum of ϕ-meson, and therefore would involve the resolution of particle momentum [24]. In this analysis, the incident photon energy is determined with ambiguity. The number of tagger hits is therefore required to be one, that is $natg = 1$

3.3.4   Missing mass and K^+K^- invariant mass cut

The missing mass and K^+K^- invariant mass cut are used to make preliminary elimination of possible background events. Firstly, to require that the observed K^+K^- originate from ϕ-meson resonance, cut on invariant mass is applied. For LD$_2$ and LH$_2$ events data, invariant mass M_{inv} of identified K^+K^- is shown in Fig 3.10.
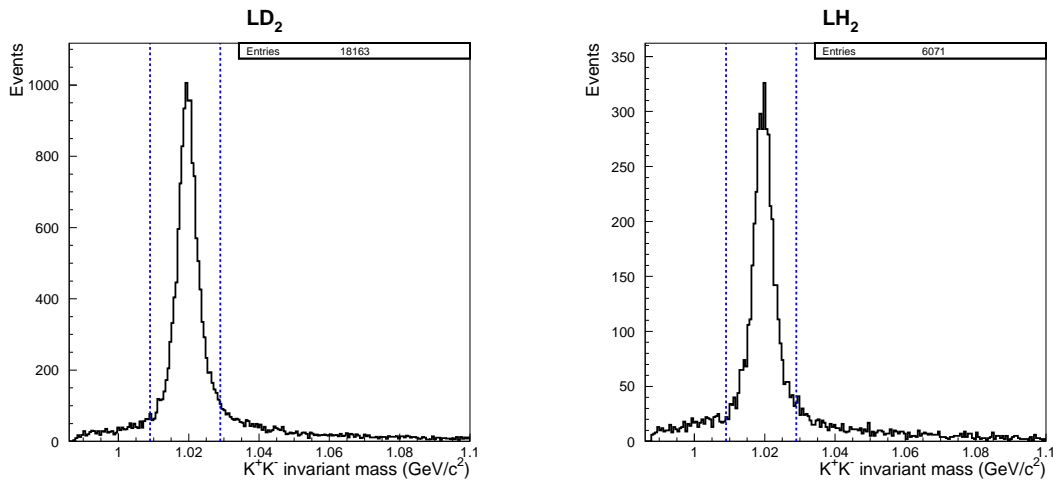
Figure 3.10: Cut on invariant mass.
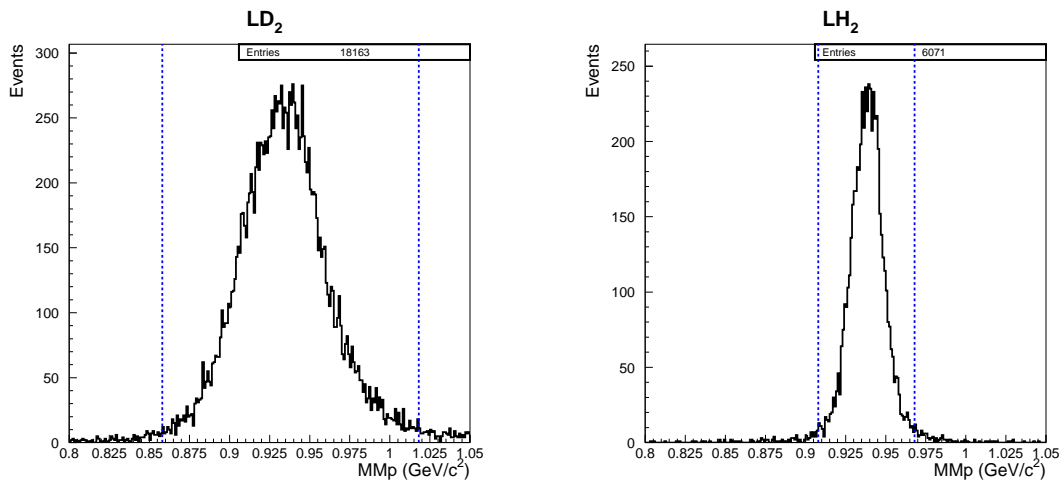
Figure 3.11: Cut on MM$_p$.

As can be seen in Fig 3.10, a prominent peak around ϕ mass (1.019 GeV) is observed in both LD$_2$ and LH$_2$ events. To select possible ϕ events, the cut on invariant mass is set to be 1.009 GeV $< M_{inv} <$ 1.029 GeV, which is illustrated by dash lines in the plot.

Secondly, cut on missing mass is made to require that the events come from the demanded reaction such as $\gamma + d \rightarrow \phi + pn$ or $\gamma + p \rightarrow \phi + p$. Here, it is MM_p to be cut, as shown in Fig 3.11. For the LH_2 events, the MM_p distribution shows a clear peak around the mass of proton, 0.938 GeV. The cut is therefore set to be 0.908 GeV < MM_p < 0.968 GeV on LH_2 MM_p . For the LD_2 events on the other hand, peak is also observed but the width of the peak is significantly wider than that of the LH_2 events. This broadening effect can be understood to be caused mainly by the Fermi motion discussed in subsection 3.7.1 and the additional contribution from coherent interaction in the LD_2 events. The cut on LD_2 MM_p is set to be 0.858 GeV < MM_p < 1.018 GeV and note that this cut is applied only for the incoherent events disentanglement, but not for coherent events. This is because that the coherent contribution is much lower than the dominating incoherent one and this cut would probably make the statistics of the coherent events too poor to be disentangled. Further, as can be seen in Fig. 3.12, strong correlation between MM_d and MM_p is shown, and therefore the cut on MM_p would not affect the ability of disentanglement by MM_d . The detail about the disentanglement procedure will be discussed in section 3.4.
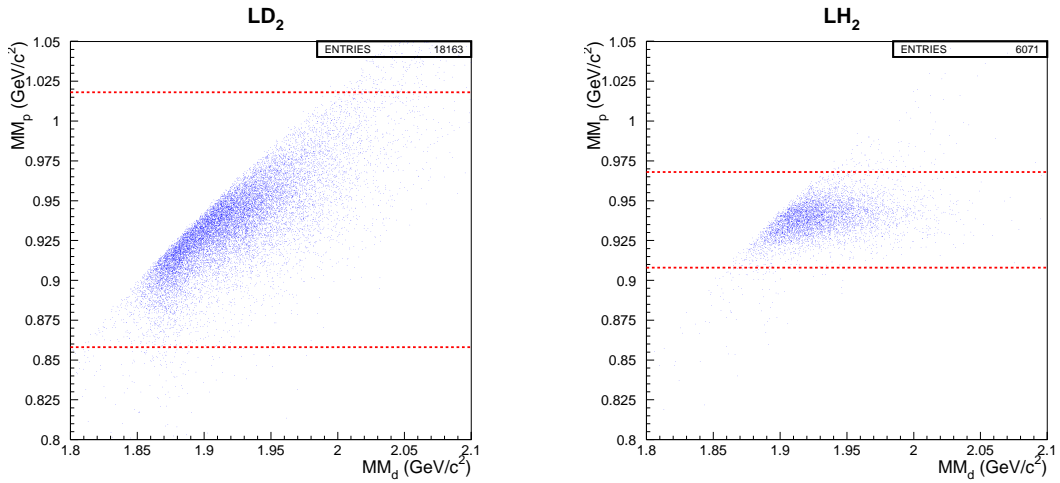
Figure 3.12: Scatter plots of MM_d and MM_p .
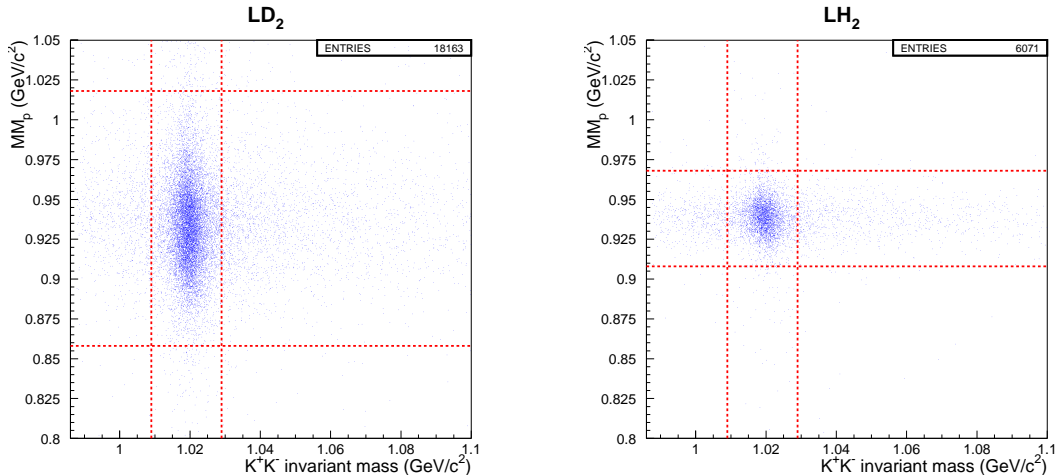
Figure 3.13: Box-cut on K^+K^- invariant mass and MM_p .

The cuts on invariant mass and missing mass for LD_2 and LH_2 target events are shown in all by the box-cut in Fig. 3.13.

3.4   Disentanglement by MM_d

From the definition of coherent and incoherent interaction, one obvious way to distinguish events of coherent interaction from those of incoherent one is to exclusively measure the final state particles to see if the deuteron breaks up into nucleons or not. However, this approach is not appropriate because the LEPS detector at very forward angle would result in extremely poor statistics for the simultaneously detecting mode.

In this analysis, the disentanglement of the coherent interaction contribution and incoherent interaction one is achieved by missing-mass analysis which is somewhat similar to the procedure utilizing missing energy spectra in [16].
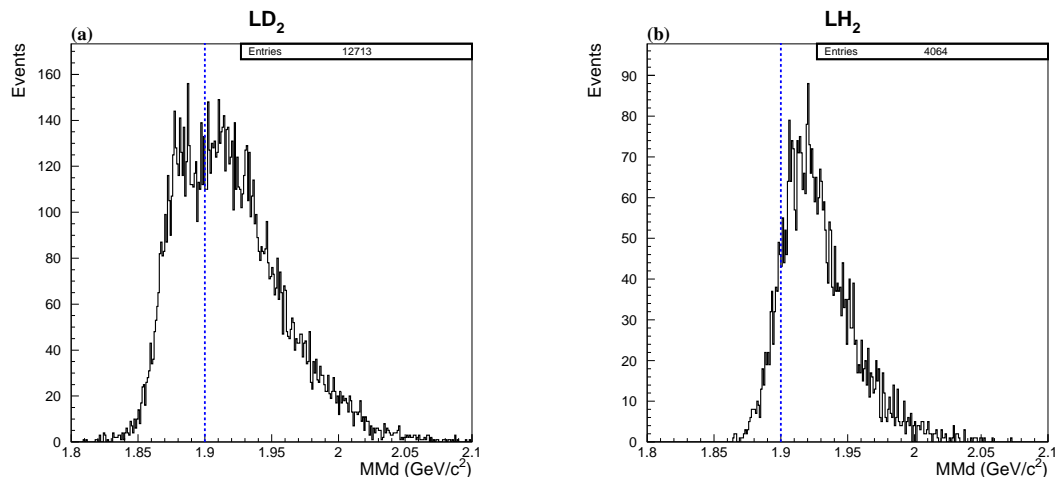
Figure 3.14: MM_d distribution.

The MM_d spectra of LD_2 event data and LH_2 one are shown in Fig. 3.14. By comparing the LD_2 MM_d spectra with the one of LH_2 which reside at the higher MM_d region, a clear peak is seen in the region $MM_d < 0.1.9$ GeV with the peak around the deuteron mass, 1.8756 GeV. This additional structure manifest the presence of the coherent interaction in LD_2 target events.

Another evidence of the contribution from coherent interaction is shown in Fig. 3.15, where the scatter plots of photon energy versus MM_d and MM_p are shown with the lines indicating the proton mass and the deuteron mass. From the plots of LH_2 target events, it can be seen that the MM_p distribution gathers around proton mass with different E_γ and a clear band is formed. On the other hand, the LH_2 MM_d is smeared out and no significant concentration is observed. The reason for this is that reaction mechanism of LH_2 is correctly evaluated with MM_p , not MM_d . Correspondingly, the "right" way to describe the missing mass of coherent interaction is MM_d , and the concentration of coherent MM_d contributes towards the two-peaks distribution of LD_2 MM_d spectra which is not shown in LD_2 MM_p spectra in Fig. 3.11.

For reasons discussed above, the disentanglement can be done by fit the LD_2 MM_d spectra with Monte-Carlo-simulated coherent and incoherent events. Certainly, the disentanglement should not depend on whether it is MM_d or MM_p to be fitted if the Monte Carlo simulation is reliable. The examination on this is presented in Appendix B.1.
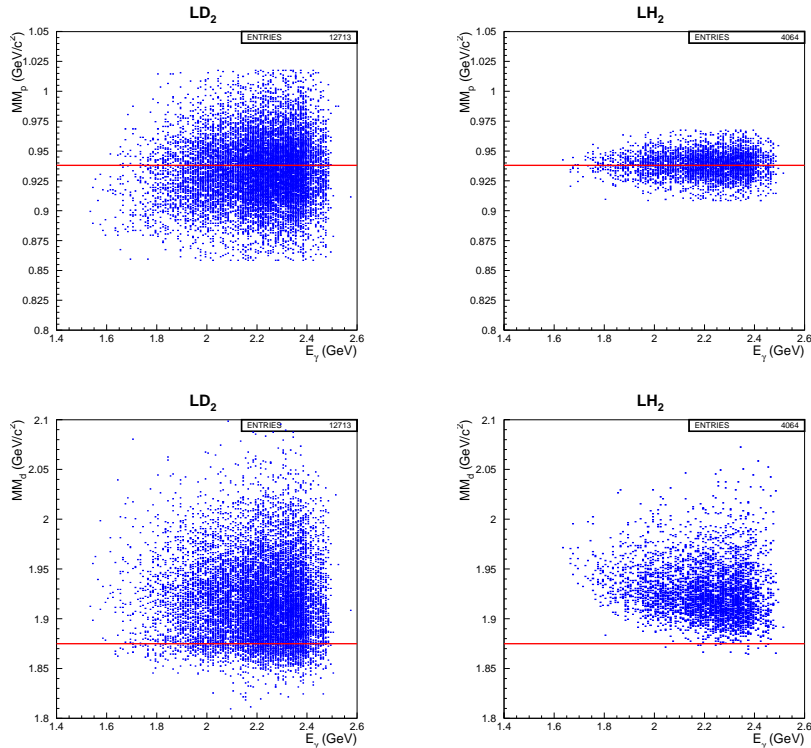
Figure 3.15: Scatter plots of E_γ versus MM_d (top) and MM_p (bottom).

To know the dependence of differential cross section on E_γ and t , the yield of events as a function of E_γ and t need to be extracted. That is, the disentanglement need to be performed in each E_γ and t bin.

Table 3.1: The denotation of E_γ bins

E_γ bin	E_γ (GeV)
E1	1.573 - 1.673
E2	1.673 - 1.773
E3	1.773 - 1.873
E4	1.873 - 1.973
E5	1.973 - 2.073
E6	2.073 - 2.173
E7	2.173 - 2.273
E8	2.273 - 2.373
E9	2.373 - 2.473

As defined in Table 3.1, nine E_γ bins of 0.1 GeV step starting from the production threshold are chosen to be the convention of E_γ binning, and this convention of E_γ binning is frequently used in the following analysis. As to the t binning, more details need to be discussed.

In subsection 3.1.2, it is shown that the upper bound of the allowed phase space of t is defined by $-|t|_{min}$ which is a function of photon energy. To evaluate the unbiased t distribution in different E_γ , this offset must be removed and the t binning is therefore replace by $\tilde{t}$ defined as:

$$\tilde{t} = t + |t|_{min}. \tag{3.15}$$

Further, the $-|t|_{min}$ values for coherent and incoherent events, $-|t|^d_{min}$ and $-|t|^p_{min}$, are different. The fitting of MM_d therefore needs to be separately done in $\tilde{t}$ bins evaluated with $-|t|^d_{min}$ in Eq. 3.15 for coherent-event disentanglement, and with $-|t|^p_{min}$ for incoherent-event disentanglement. In the following, $\tilde{t}$ is referred to as the one corrected with corresponding $-|t|_{min}$ for different interaction processes.

The t variable is the four-momentum transfer, and the magnitude of t can be interpreted as the "violence" of the scattering; With large $|t|$, the collision takes place more violently. Since the deuteron is a loosely bound nucleus, the coherent interaction in which deuteron is not broken up should be more likely to reside in the low $|t|$ region, or in the $|\tilde{t}|$ equivalently. This naïve conjecture is support by the $\tilde{t}$ distribution shown in Fig. 3.16.
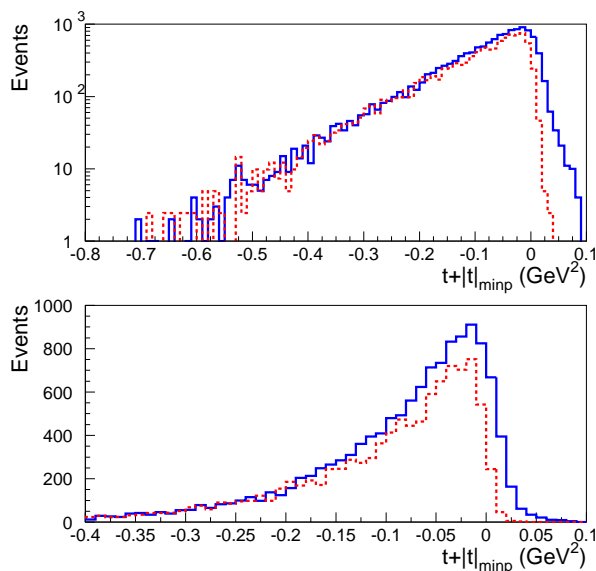
Figure 3.16: LD_2 $\tilde{t}$ distribution (solid) fitted with LH_2 one (dash) in log-scale (top) and linear scale with x-axis zoom-in (bottom).

In Fig.3.16 the solid lines are LD_2 $\tilde{t}$ distribution and are fitted by $\tilde{t}$ distribution of LH_2 events in the region $-1.0 < \tilde{t} < -0.3$ in which the incoherent interaction dominates. The fitting results of LH_2 $\tilde{t}$ distribution are represented by dash lines. From the top plot evaluated in log scale, the fitting of the high $|\tilde{t}|$ tail is acceptable and the χ^2/ndf is 2.226. But significant excess of LD_2 $\tilde{t}$ distribution is observed in the low $|\tilde{t}|$ region from the zoom-in plot in the bottom. This excess therefore provides evidence of the presence of coherent events. Since the coherent interaction takes place mostly with low $|\tilde{t}|$, the disentanglement would only be carried out in the low $|\tilde{t}|$ region.

As discussed above, disentanglement utilizes the Monte-Carlo-generated coherent and incoherent events. The Monte Carlo simulation therefore needs to be repeatedly tested to produce convincing results.

3.5   Examination on particle momentum evaluation

In this and the subsequent sections, various checks to examine the validity of this analysis framework are performed. First, examination on the evaluation of the particle momentum is

made for both real data and Monte-Carlo case.

Particles loss energy during their passage and the rate they loss their energy depends on the material they travel through. The determination of particle momentum is dependent on this energy loss and it is therefore necessary to check calibration such as energy-loss correction is properly implemented.

The invariant mass and missing mass are utilized because they need proper momentum evaluation to be correctly deduced. By making various invariant mass and missing mass distribution, looking over the peak values of these different mass distribution, see if they are consistent with the accredited ones provide in [21], the examination is made.
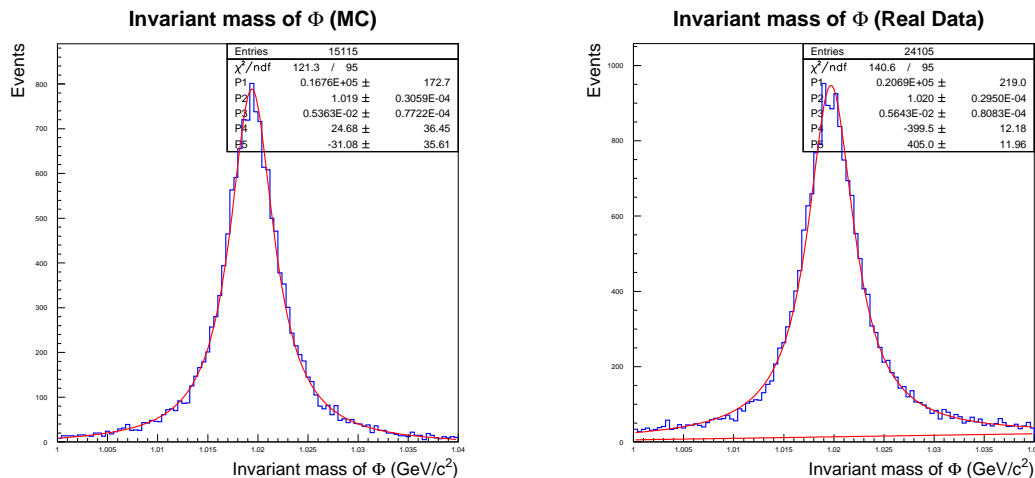
Figure 3.17: Invariant mass K^+K^- of ϕ.

In Fig. 3.17, K^+K^- invariant mass of ϕ-meson from both Monte-Carlo data and LD$_2$ real data are made and fitting of the distribution is made. The purpose of the fitting is to get the peak value, so a naïve fitting function consisting of a Breit-Wigner distribution which is used to describe the cross-section of resonant nuclear scattering:

$$BW(x) = \frac{A}{2\pi} \cdot \frac{\Gamma}{(x - m_0)^2 + (\Gamma/2)^2}, \tag{3.16}$$

plus a first-order polynomial is chosen simply for making reasonable fitting but for solid physical reason. As is shown, the fitting parameters P1 to P5 are A, m_0, Γ, and the coefficients of the polynomial. The value of the peak m_0 of Monte-Carlo data is 1.019 GeV and the peak of the LD$_2$ real data is 1.020 GeV. Both of these two values are acceptable as being compared to the accredited mass value of ϕ, 1.019 GeV.

Fig. 3.18 shows the MM$_p$ value of the Monte Carlo Simulated LH$_2$ data and real LH$_2$ data. The naïve fitting function is chosen to be a Gaussian distribution:

$$G(x) = \frac{A}{\sigma \sqrt{2\pi}} \cdot exp[-\frac{1}{2}(\frac{x - \mu}{\sigma})^2], \tag{3.17}$$

plus a first-order polynomial and P1 to P5 denotes A, μ, σ, and the coefficients of the polynomial. Still both of the peak values μ are 0.939 GeV which are acceptable as the accredited value of the mass of proton is 0.938 GeV.

An additional check on the invariant mass K^-p of LD$_2$ real data to get the $\Lambda(1520)$ resonance distribution as is shown in Fig. 3.19. By fitting the distribution with a Breit-Wigner distribution
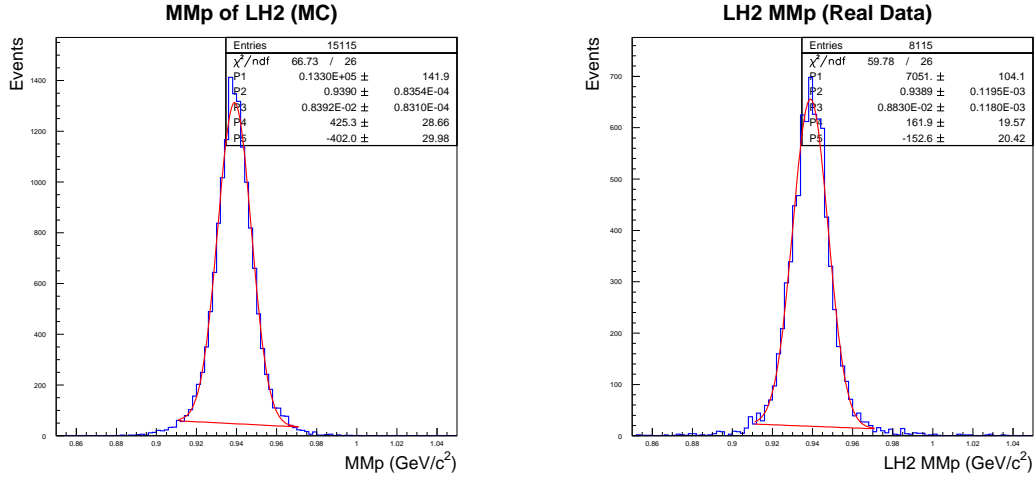
Figure 3.18: MM_p on LH_2 target.
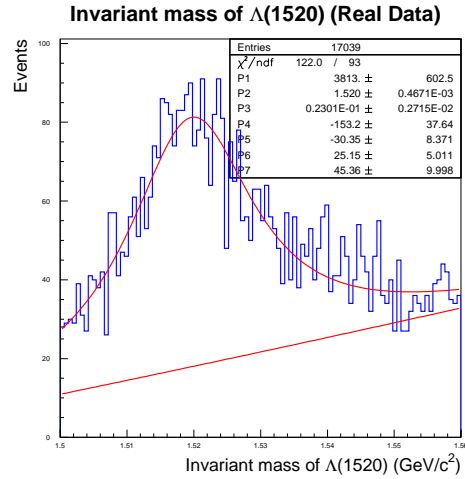
Figure 3.19: Invariant mass K^-p of $\Lambda(1520)$.

plus a third-order polynomial, the extracted peak value P2 is 1.520 GeV, just the same as the accredited value of the mass of $\Lambda(1520)$.

Supplementary survey on the stability of the momentum resolution is given in Appendix A. using PID related approach and the stability of the momentum resolution appeared stable during the runs of the data sample used.

3.6   Smearing of photon energy

The photon energy E_γ is determined by the procedure discussed in the previous subsection 3.3.3. The measured photon energy is not precisely be the actual photon energy due to inevitable experimental inaccuracy and thus definite resolution of photon energy is expected.

In Monte Carlo simulation, however, the photon energy E_γ^{MC} is known because E_γ^{MC} is given by the event generator. To imitate the the effect of the experimental indeterminacy of photon energy E_γ , a smearing procedure is performed on the Monte-Carlo-generated photon energy

E_γ^{MC} .

The smearing of E_γ^{MC} is done by randomly modulating the E_γ^{MC} value to be $E_{\gamma-smeared}^{MC}$ in the range of ($E_\gamma^{MC} \pm 5\sigma$), with a Gaussian probability distribution P_{gauss}^{smear} defined as:

$$P_{gauss}^{smear} = exp[-\frac{1}{2} \cdot (\frac{E_{\gamma-smeared}^{MC} - E_\gamma^{MC}}{2\sigma})^2]$$

The σ value is then the adjustable degree of the smearing, in other words, the user-defined resolution of E_γ^{MC} .

It should be noted that the resolution of E_γ is coupled with the momentum resolution due to Eq. 3.14 as is reported in [24]. With the stable momentum resolution as is checked in Appendix A, it is attempted to set a stable smearing to give the appropriate simulation. Three kinds of σ values is chosen:

- $\sigma_{10MeV} = 10$ MeV

- $\sigma_{15MeV} = 15$ MeV

- $\sigma_{composite} = 8$ MeV(72%) + 21 MeV(28%)

The first option comes from previous results of LEPS measurements and are reported for example in [25, 26]. The third option which may appear confusing at the first glance comes from the fitting of the MM_p distribution of the real data because the MM_p distribution would be better fitted with two Gaussian of different widths [27]. This option is somewhat close to the one setting the σ to be $8 \times 0.72 + 21 \times 0.28 = 11.64$ MeV directly.

The MM_p of LH_2 data is utilized to make the examination because MM_p is evaluated with incident photon energy and because of its simplicity of reaction mechanics. A simple conjecture is that the different smearing way would exhibit their effect in the width of MM_p distribution– the severer the smearing applied, the wider of the MM_p distribution is obtained.

The MM_p distribution from LH_2 real data and from Monte Carlo simulation with the three ways of E_γ^{MC} smearing are separately generated in nine different E_γ bins defined in Table 3.1. The MM_p -distribution histograms of real data are then fitted with the ones from Monte Carlo. The results of the fitting are give in Fig. 3.20, Fig. 3.21, and Fig. 3.22 with the real data depicted in solid line and data from Monte Carlo depicted in dash line.

It is found that in the E9 bin, all the three kinds of smearing ways give poor fitting and the whole shape of the MM_p distribution from Monte Carlo is shifted toward higher value. The reason is that the smearing of the photon energy is made after the event is generated, and the reaction takes place with the unsmeared E_γ^{MC} . The E9 bin is the highest energy bin and there are events with E_γ^{MC} near the boundary of the generated E_γ^{MC} distribution. To coerce the E_γ^{MC} value of these events to take arbitrary variation would cause some of the smeared photon energy cross the boundary. This overestimate effect of can't be equally compensated by the underestimate one because there are no events with E_γ^{MC} higher than the boundary. This over-estimation effect is not found in MM_p distribution of real data because the resolution of E_γ wouldn't have preference to overestimate or underestimate, it is only the inability to ascertain what the real E_γ is.

Fig. 3.23 gives a clearer illustration to show the overestimation effect of Monte-Carlo generated MM_p distribution. In the plot, the MM_p distribution in E9 bin is further divided in to five smaller bins ranging from 2.373 GeV to 2.423 GeV with 0.01 GeV step size. With the increase of the energy bin, shifting of the MM_p distribution occurs significantly.

From Fig. 3.20 to Fig. 3.22, the fitting of σ_{10MeV} and $\sigma_{composite}$ smearing give better over-all χ^2/ndf values than the σ_{15MeV} one.
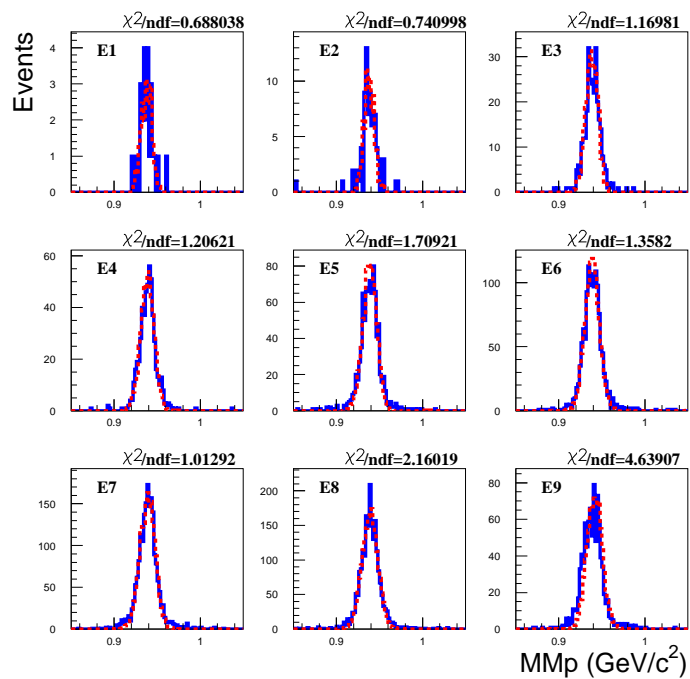
Figure 3.20: Fitting of LH$_2$ MM$_p$ of σ_{10MeV}.
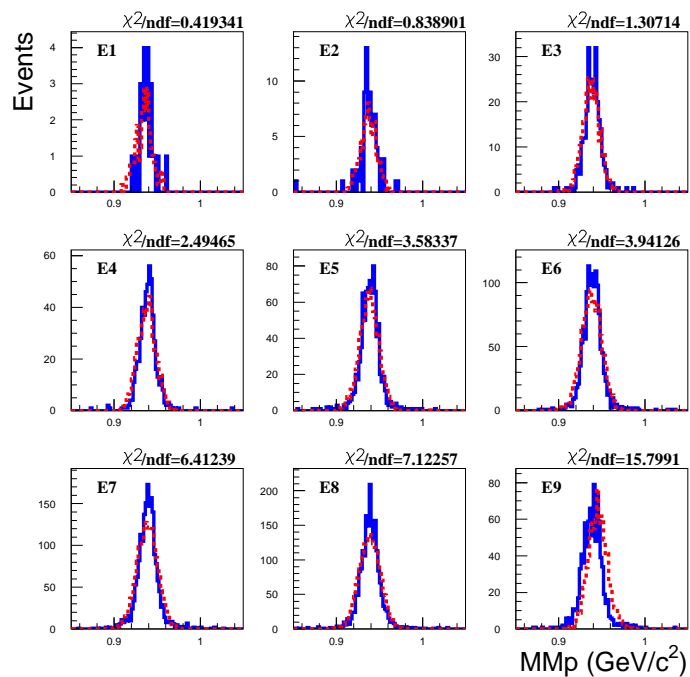
Figure 3.21: Fitting of LH$_2$ MM$_p$ of σ_{15MeV}.
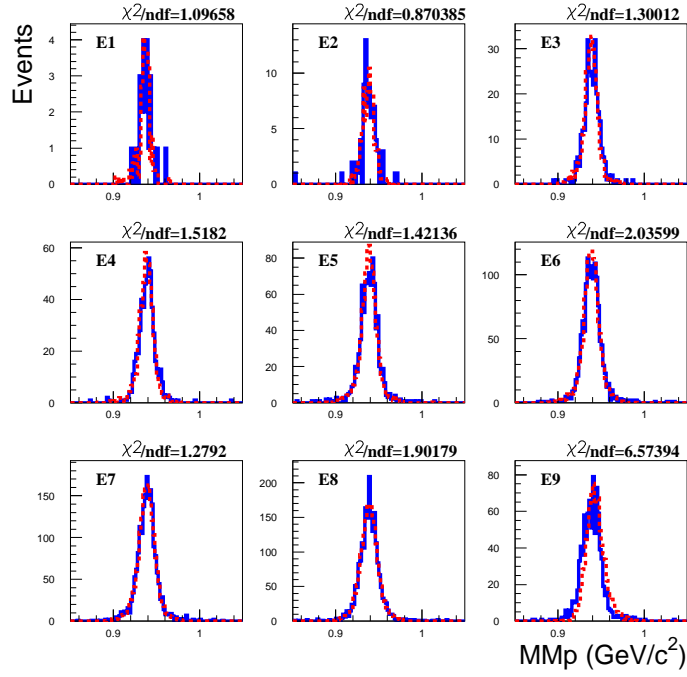
Figure 3.22: Fitting of LH$_2$ MM$_p$ of $\sigma_{composite}$.
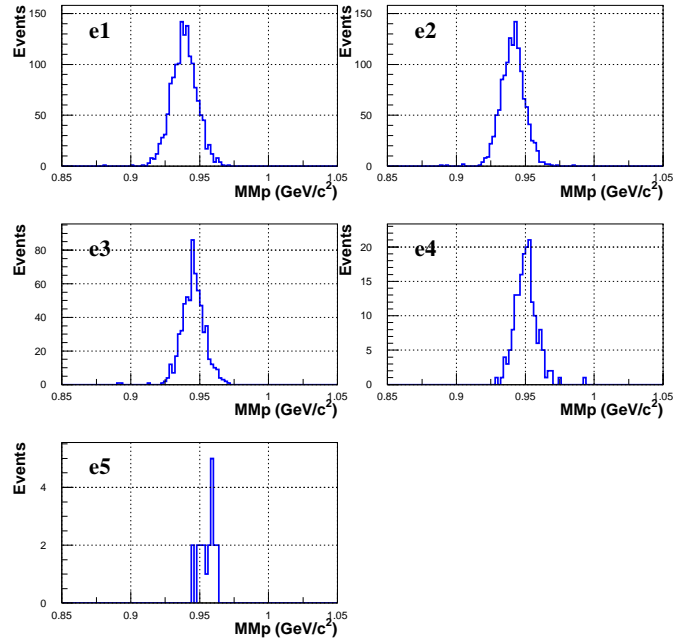
Figure 3.23: Monte Carlo generated LH$_2$ MM$_p$ of σ_{10MeV} in E9 bin.

Another check is performed by fitting the MM_p in each E_γ bin with Gaussian distribution defined as Eq. 3.17. The peak value μ and the width σ of the Gaussian is given by the fitting. The μ and σ values of the three different smearing are then compared with the ones from the real data as shown in Fig. 3.23.
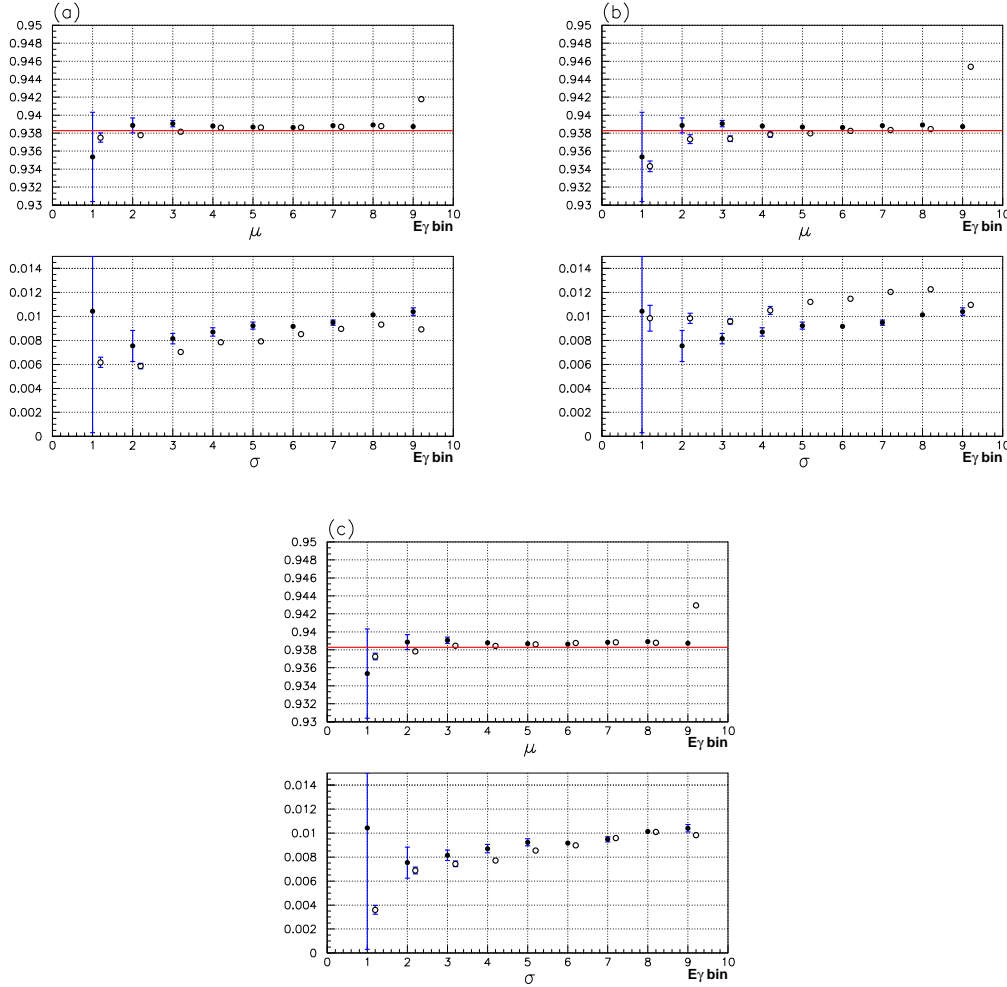
Figure 3.24: Values of peak and width of the LH_2 MM_p distribution.

Fig.3.24 (a), (b), and (c) show the result of smearing of σ_{10MeV}, σ_{15MeV}, and $\sigma_{composite}$ separately. The upper half of each plot is the mean value μ with the proton mass 0.938 lined up and the lower half is the width σ. With the values of real data denoted as closed circles and values from Monte-Carlo data denoted as open circles, the three different ways of smearing give reasonable coincidence for μ values. But the $\sigma_{composite}$ smearing matches σ values of real data better than the other two ways of smearing.

From the two examinations above, $\sigma_{composite}$ gives the best description of the shape of LH_2 MM_p of real data. The option $\sigma_{composite}$ is therefore chosen as the way of smearing of photon energy.

The breakdown of the smearing in E9 bin observed here should be regarded as a warning of the necessity to give up the physical result of this photon-energy bin.

3.7 Bound nucleons

The Monte Carlo simulation of coherent events is relatively simpler because incoherent inter-action of deuteron involves the interaction with bound proton and neutron kinematically. The kinematic property of the bound nucleons is therefore necessary to be taken into account to make proper Monte Carlo simulation. Two features of the bound nucleons, Fermi motion and off-shell effect, are discussed and the treatment of Monte Carlo simulation of them is explained in this section.

3.7.1 Fermi motion

The nucleus is not a object with static nucleons inside. For example, by comparing the energy spectrum of electrons elastically scattered off free nucleons and bound nucleons, it is observed that broader peak appears when the nucleon is bound [28]. This broadening of the maximum gives a manifestation that the nucleon bound inside the nucleon moves around quasi-freely inside the nucleus. This motion is call the Fermi motion and it would bring a change in the kinematics compared to scattering off a nucleon at rest.

The typical momentum value of Fermi motion of nucleons bound in a deuteron is around 100 MeV/c. The momentum distribution of nucleons inside the deuteron target of Monte Carlo simulation is implemented using the PARIS N-N potential [29].

3.7.2 Off-shell effect

The nucleon in nucleus is not free but in a status constantly interacting with other nucleons. This in-medium effect would cause the property of the nucleon to deviate the regulations of classical mechanics and is referred to as off-shell effect.

The off-shell property of nucleon has been investigated but no solid theoretical formulation has been established. The treatment to the effect for now simply bases on model construction and phenomenological parameterization [30, 31].

For the proton and neutron bound inside the deuteron, their mass is not on their mass shell and their distance to the mass shell is related to the binding energy which is 2.225 MeV for ground state deuteron. This mass off-shell effect would cause the MM_d distribution of incoherent events to be slightly shifted.
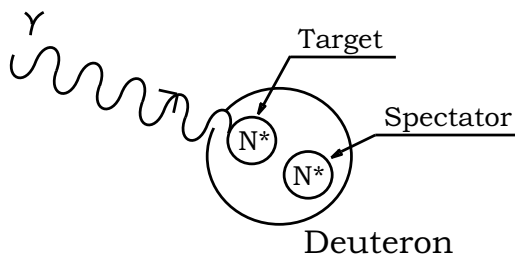
Figure 3.25: Photon interact with one target nucleon.

But note that the disentanglement depends on the MM_d distribution of incoherent and coherent Monte Carlo simulation. The separation between the two peaks of LD_2 MM_d distri-bution shown in Fig. 3.14 is only around 35 MeV, and therefore the disentanglement is indeed sensitive to the MM_d distribution to the scale of a few MeV. Difference in the shifting of the MM_d distribution of different off-shell-effect-implemented incoherent Monte Carlo simulation

would make significant variation between extracted yield of coherent and incoherent events. For this reason, the off-shell effect should be carefully handled.

Fig. 3.25 shows the graphical illustration of incoherent reaction with off-shell nucleons denoted as N*, the nucleon struck by the incident photon referred to as target nucleon, and the other nucleon referred to as spectator nucleon. Eight types of off-shell schemes are tried out as [32]:

- **Scheme 1**:
  Set-(a): The target nucleon is assigned to take fully the off-shell effect and the spectator nucleon be on-shell. The target nucleon returns on-shell after interacting with the photon.
  Set-(b): The same with set (a) except that the target nucleon remains off-shell after interacting with the photon.

- **Scheme 2**:
  Set-(a): The target and the spectator nucleon set to be equally off-shell. The target nucleon returns on-shell after interacting with the photon.
  Set-(b): The same with set (a) except that the target nucleon remains off-shell after interacting with the photon.

- **Scheme 3**:
  Set-(a): The target and the spectator nucleon are both on-shell and modify the incident photon energy in order to conserve the total energy. The target nucleon returns on-shell after interacting with the photon.
  Set-(b): The same with set (a) except that the target nucleon remains off-shell after interacting with the photon.

- **Scheme 4**:
  Set-(a): The target and the spectator nucleon set to be equally off-shell and an additional -5 MeV potential is imposed on the target nucleon. The target nucleon returns on-shell after interacting with the photon.
  Set-(b): The same with set (a) except that the target nucleon remains off-shell after interacting with the photon.

To determine the most appropriate off-shell scheme, the MM_d of real LD_2 data is fitted in each conventional E_γ bin with the Monte-Carlo-generated incoherent events in the high mass region of $MM_d \geq 1.9$ GeV which is shown in section 3.4 to contain mostly the incoherent events. The fitting incoherent events are then subtracted from the MM_d of real LD_2 data and the residual obtained is considered to be the coherent component of the real data. This residual is then fitted with Gaussian distribution, Eq. 3.17, to obtain the peak and width value of the residual. Also, the Gaussian fitting is applied as well on Monte-Carlo-simulated coherent events and the consistency of the peak and width between the residual distribution of real data and the Monte-Carl-simulated coherent events is then utilized as the criteria to select out the best scheme.

Fig. 3.27 shows the peak and width values with the open circles denoting the results from Monte-Carlo-simulated coherent data and the closed circles denoting those from LD_2 residual. The line in the plot of the peak values indicates the mass of deuteron, 1.8756 GeV. Only the results of scheme 1-(a) and scheme 2-(a) are illustrated because these two schemes give the best agreement of the peak and width values.
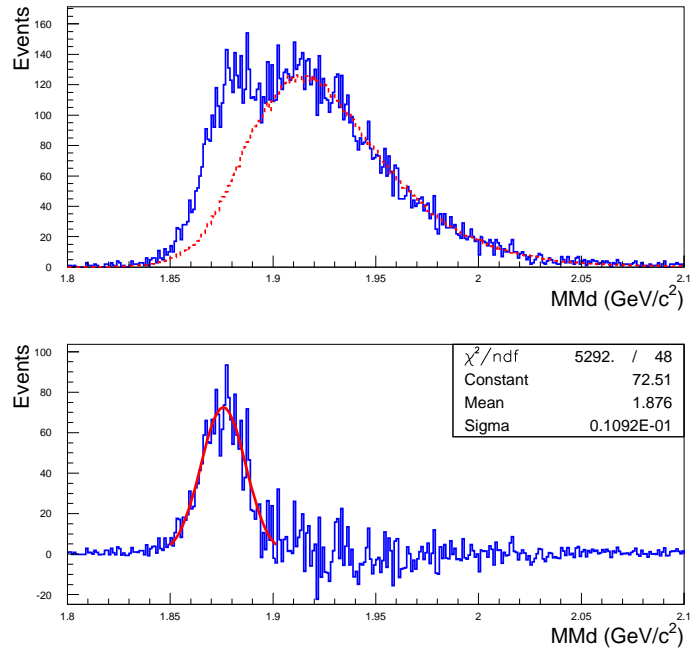
Figure 3.26: Off-shell effect examination on peak and width in different E_γ bin.
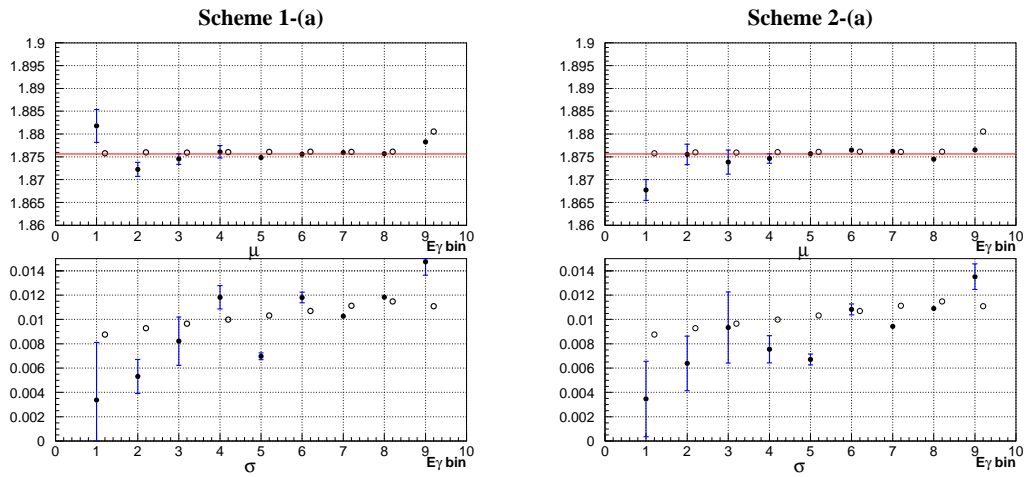
Figure 3.27: Off-shell effect examination on peak and width in different E_γ bin.
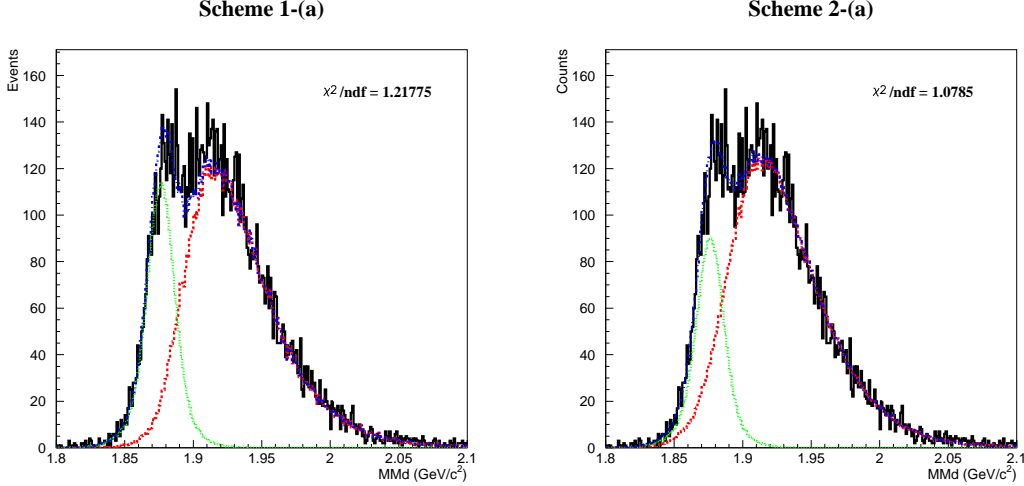
Figure 3.28: Off-shell effect examination on MM_d fitting.

Another examination is then preformed. As shown in Fig. 3.28, the MM_d fitting of LD_2 real data by Monte-Carlo-simulated coherent events and incoherent events of scheme 1-(a) and scheme 2-(a). As can be seen, scheme 2-(a) gives the better χ^2/ndf value still.

Because of the best agreement among all the examinations, scheme 2-(a) is therefore selected to be the off-shell treatment of Monte Carlo simulation of incoherent events. The results of the schemes other than 1-(a) and 2-(a) can be found in Appendix E.1.

3.8 t resolution

3.8.1   Rough estimation

To determine the reasonable bin size of t for the evaluation of $d\sigma/dt$, the resolution of t need to be estimated. First, the resolution of t can be conjectured base on the understanding of the resolution of E_γ discussed in section 3.6. As is reported in [24], the typical momentum resolution is around 1.3 MeV which is small compared to the E_γ resolution obtained in section 3.6. It's fairly enough to attribute the t resolution to the resolving ability of E_γ .

Same as the previous treatment, the four-momentum of the incident photon can be written as $k_{real} = (E_\gamma, 0, 0, E_\gamma)$. The measured E_γ deviates from this real photon energy in the amount of the resolution of photon energy, σ_γ, approximately. The four-momentum of the measured E_γ can then be written as:

$$k_{measured} = (E_\gamma \pm \sigma_\gamma, 0, 0, E_\gamma \pm \sigma_\gamma). \tag{3.18}$$

The four-momentum of ϕ-meson is defined as $q = (E_\phi, p_{\phi x}, p_{\phi y}, p_{\phi z})$. Because the setup of LEPS spectrometer is at the very forward angle, the ϕ-meson produced with momentum of larger z-direction component would be accepted. Therefore the x- and y-component are neglected and the four-momentum of ϕ-meson can be rewritten as $q = (E_\phi, 0, 0, p_{\phi z})$. Assume the resolving ability of t is limited solely by the resolution of E_γ , the resolution of t is thus deduced as:

$$\sigma_t = t_{real} - t_{measured} = (k_{real} - q)^2 - (k_{measured} - q)^2. \tag{3.19}$$

Together with Eq. 3.18, Eq. 3.19 gives:

$$\sigma_t = \pm\, 2\sigma_\gamma(p_{\phi z} - E_\phi).$$

And this equation can be further reduced to:

$$\sigma_t = \pm \; \sigma_\gamma \frac{M_\phi^2}{p_{\phi z}}. \tag{3.20}$$

Take the E_γ resolution acquired in section 3.6 as $\sigma_\gamma \simeq 11$ MeV, typical $p_{\phi z} \simeq 1.2$ GeV/c, and M_ϕ, the resolution of t is then deduced approximately as $\sigma_t \simeq 10$ MeV^2

3.8.2 Examination by Monte Carlo simulation

Estimation of t resolution can also be made by utilizing the Monte Carlo simulation.

Let the t evaluated from the event generator is denoted as t_{gene} and this value represents the exact t value of the physical event. On the other hand, t_{meas} denotes the t value obtained with the experimental uncertainties considered and then processed by the same procedure as is done on the real data. Make the distribution of $t_{gene} - t_{meas}$ and then fit the distribution with Gaussian distribution, Eq. 3.17. The σ value of the Gaussian fitting is then the resolution of t .
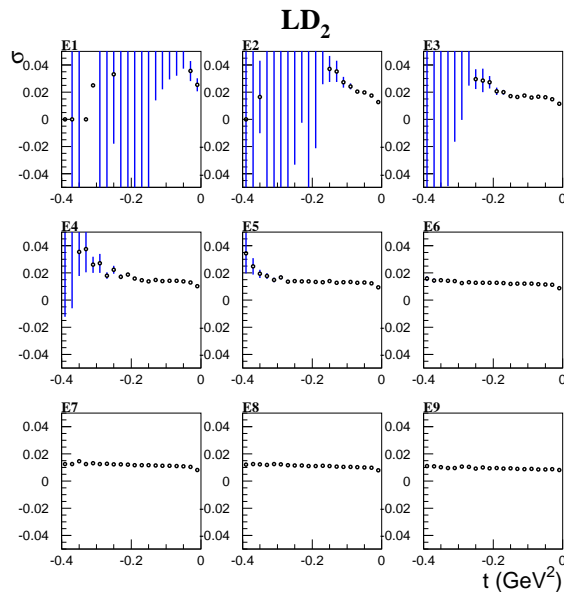
Figure 3.29: The t resolution of LD$_2$ data.

Fig. 3.29 and Fig. 3.30 show the σ_t values in different E_γ bin as a function of t in the region $-0.4 \; GeV^2 \leq t \leq 0.0 \; GeV^2$ for the LD$_2$ and LH$_2$ data from Monte Carlo simulation. As can be seen in the plots, in the low E_γ bins, the σ_t values fluctuate violently and large error bar appeared due to the insufficient statistics in these E_γ regions. This fluctuation is smoothen in the high E_γ bins and the σ_t values approach a steady distribution of value lower than 0.02 GeV^2 in both cases. The resolution of t is therefore concluded to be somewhat better than 0.02 GeV^2 or 20 MeV^2, which coincides the result of the rough deduction in subsection 3.8.1.
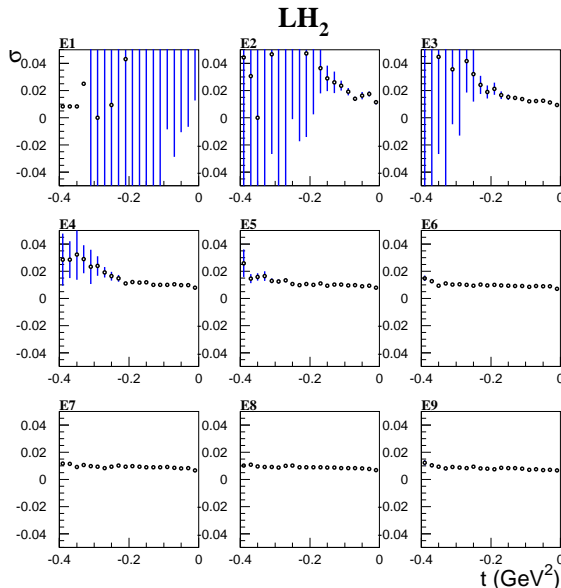
Figure 3.30: The t resolution of LH_2 data.

3.9 Background subtraction

3.9.1 Possible backgrounds

The ϕ-meson is identified by the invariant mass of K^+K^- . It can be seen that there are events away from the main peak distribution of ϕ, these events that are not from those produced ϕ are called the backgrounds.

Backgrounds come in two categories. The first type of backgrounds come from specific reactions which are not of interest but may occur with the same initial state and result in same final state particles. These kinds of backgrounds can likely be understood by theoretical approach and handled with Monte Carlo simulation. The other possibility of backgrounds, on the other hand, come from sources that can't be identified such as random noises of the electronic equipments. Here, only the first type of backgrounds are discussed and the second type of backgrounds are assumed to be suppressed to the scale that can cause only minor effect to the real ϕ signals.

The main backgrounds come from two types of reaction known; the non-resonant KKN production and the $\Lambda(1520)$ production:

$$\gamma + N \rightarrow K^+ + K^- + N, \tag{3.21}$$
$$\gamma + p \rightarrow \Lambda(1520) + K^+ \rightarrow K^- + p + K^+. \tag{3.22}$$

The K^+K^- produced from non-resonant KKN production wouldn't form resonance, they are produced only from phase space. The $\Lambda(1520)$ hyperon would decay into K^-p with the branching ratio of 23 and therefore makes contribution to the K^+K^- final state.

Among these two backgrounds, non-resonant KKN production should take the majority of the backgrounds which is illustrated in [13] or other previous studies of LEPS group. Especially in the K^+K^- mode used for this analysis, the K^--mesons generated from $\Lambda(1520)$ decay are more likely to deviate from the spectrometer and have less probability to be detected because most of the momentum of $\Lambda(1520)$ would be taken away by the heavier proton. The $\Lambda(1520)$

contribution in K^+K^- mode is therefore suppressed for this reason.

The Monte-Carlo simulated K^+K^- invariant mass distribution for non-resonant KKN and $\Lambda(1520)$ backgrounds are shown in Fig. 3.31. It can be seen that no peak around mass of ϕ (1.019 GeV) is observed.
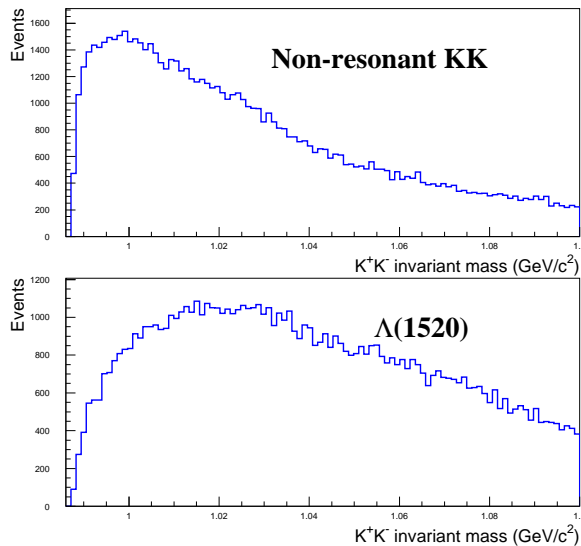
Figure 3.31: Monte Carlo simulated K^+K^- invariant mass of backgrounds.

Attempts to reproduce the real data with these Monte-Carlo-simulated backgrounds gave unsatisfactory results. One of the possible reasons could be that the physical process of the non-resonant KKN background is unknown. Simultaneous fitting on different spectra of real data was performed as shown in Fig. 3.32 by utilizing the **MINUIT** package [33] and unsatisfactory results of fitting was obtained. The simultaneous fitting would give better χ^2/ndf in smaller phase space, that is, with E_γ and $\tilde{t}$ binning. But the result is questionable due to low statistics in individual bin.
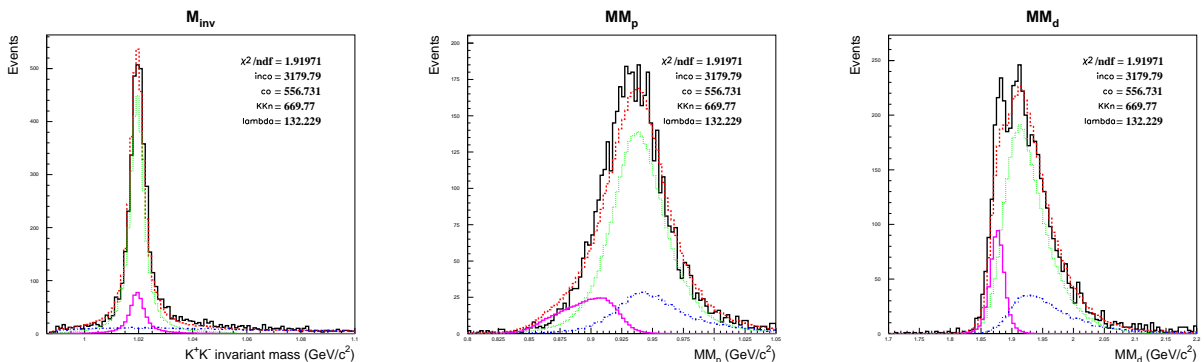
Figure 3.32: Simutaneous fitting with Monte Carlo simulated backgrounds in E8 bin.

Undeniably, the background treatment with Monte Carlo simulation claims on entire understanding of the background properties and this may be the cause of the failure of the Monte-Carlo-simulation treatment. Another approach using phenomenological description of

the background is therefore adopted.

3.9.2   Phenomenological approach

The phenomenological approach assumes that the distribution of the background events are continuous and smooth in the invariant mass region considered. Under this assumption, by fitting the invariant mass distribution away from the signal peak which can all be considered to be background events, the backgrounds contained in the signal peak are extrapolated.

A phenomenological background function with a polynomial of leading order of 2 is suggested in the previous measurement of ϕ-meson [34]. The background function is therefore chosen to be a second-order polynomial. A preliminary fitting of LD_2 and LH_2 K^+K^- invariant mass with a Breit-Wigner distribution representing the signal plus a second-order polynomial background is shown in Fig. 3.33 and the results are tabulated in Table 3.2. In Fig. 3.33, the K^+K^- invariant mass distribution from real data are denoted as cross symbols and the fit result with background distribution together are the solid lines. The vertical lines in the plots indicate the invariant mass cut (1.009 GeV $< M_{inv} < 1.029$ GeV) discussed in section 3.3.4.
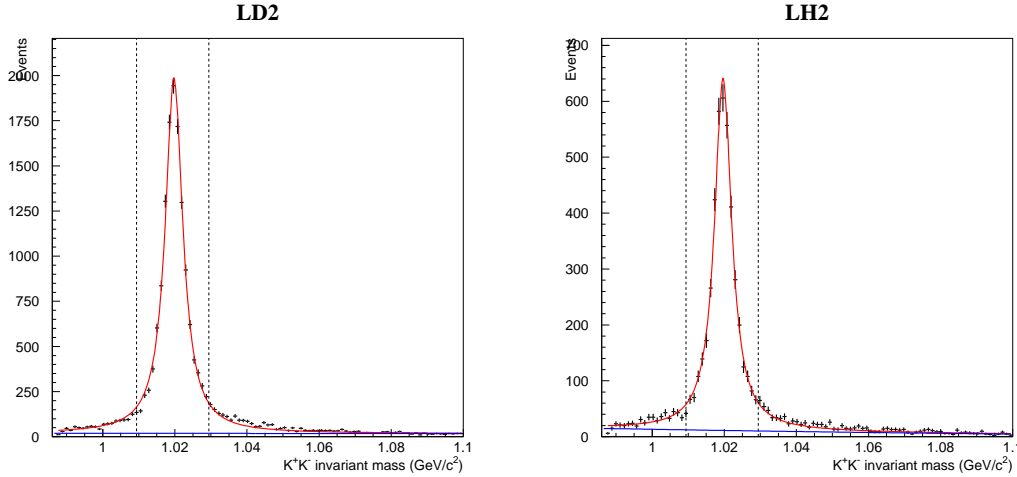
Figure 3.33: Fitting of K^+K^- invariant mass with background.

Table 3.2: LD_2 fitting result and extracted background in different E_γ bin

Data set	Peak (GeV)	χ^2/ndf	N_{signal}	N_ϕ	N_{BG}	N_{BG}/N_{signal}
LD_2	1.0198	3.0961	13588	13231	357	0.0263 ± 0.0014
LH_2	1.0197	1.4591	4370	4156	214	0.0490 ± 0.0033

As can be seen in Fig. 3.33, there are only few background contributions in both LD_2 and LH_2 events. This can also be seen by the low background-to-signal ratio N_{BG}/N_{siganl} listed in Table 3.2 where N_{siganl}, N_{BG}, and N_ϕ are the original event signals, the extracted backgrounds, and the background-subtraction obtained ϕ signals in the 1.009 GeV - 1.029 GeV invariant mass region. The relation between these quantities is:

$$N_{signal} = N_\phi + N_{BG}. \tag{3.23}$$

Same procedure is then applied to the invariant mass distribution in different E_γ bin to

extract background components in different E_γ bin. Still, a small number of backgrounds are observed in every E_γ bin.

As can be seen in Eq. 3.21 and Eq. 3.22, these two main backgrounds comes from the incoherent interaction. Therefore, the extracted backgrounds from LD_2 invariant mass spectra would only be subtracted from the LD_2 incoherent events.
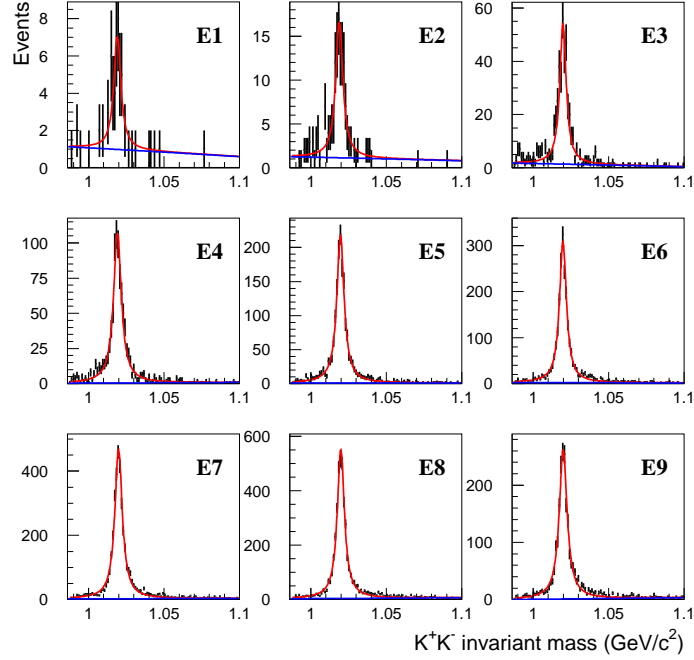
Figure 3.34: Fitting of LD_2 invariant mass with background in different E_γ bin.

Table 3.3: LD_2 fitting result and extracted background in different E_γ bin

E_γ bin	Peak (GeV)	χ^2/ndf	N_{signal}	N_ϕ	N_{BG}	N_{BG}/N_{signal}
E1	1.0191	0.2587	47	29	18	0.3896 ± 0.0704
E2	1.0189	0.4551	127	106	21	0.1695 ± 0.0332
E3	1.0198	1.1749	372	346	26	0.0720 ± 0.0134
E4	1.0191	0.9766	787	777	10	0.0131 ± 0.0040
E5	1.0196	0.8787	1468	1450	18	0.0124 ± 0.0029
E6	1.0197	1.1950	1997	1954	43	0.0218 ± 0.0033
E7	1.0199	1.7720	3229	3180	49	0.0154 ± 0.0022
E8	1.0199	1.8937	3679	3604	75	0.0206 ± 0.0023
E9	1.0199	1.3883	1874	1855	19	0.0105 ± 0.0024
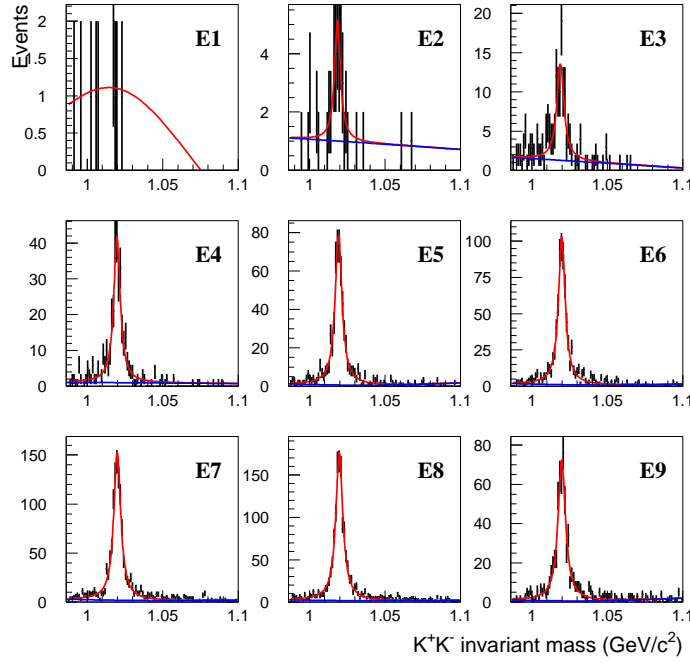
Figure 3.35: Fitting of LH$_2$ invariant mass with background in different E_γ bin.

Table 3.4: LH$_2$ fitting result and extracted background in different E_γ bin

E_γ bin	Peak (GeV)	χ^2/ndf	N_{signal}	N_ϕ	N_{BG}	N_{BG}/N_{signal}
E1	1.0200	0.1499	5	34	-29	0.0000 ± 0.0000
E2	1.0185	0.2678	33	14	19	0.5600 ± 0.0851
E3	1.0189	0.5975	116	92	24	0.2077 ± 0.0375
E4	1.0196	0.7885	288	269	19	0.0661 ± 0.0146
E5	1.0192	0.6777	521	509	12	0.0242 ± 0.0067
E6	1.0198	0.9572	669	648	21	0.0317 ± 0.0068
E7	1.0198	1.4786	1036	1000	36	0.0356 ± 0.0058
E8	1.0197	1.1231	1178	1143	35	0.0300 ± 0.0050
E9	1.0198	0.9124	517	505	12	0.0240 ± 0.0067

3.10 The acceptance

If physical events of a total number of N occurs and n events are observed among them, the relation between the expectation values of N and n can be expressed as:

$$< n >= A_{ccep} \cdot < N >,$$

where A_{ccep} is the acceptance. In this general definition, the acceptance included the detecting efficiency of the detector and the acceptibility due to geomertical set up, which is to say, the acceptance includes all possible effects that cause losses of physical events: the finite size of

detectors, the inefficiencies of detectors and of off-line event reconstruction, dead times, effects of veto counters, etc.

The acceptance for the LEPS spectrometer is obtained by the Monte Carlo simulation. Events of ϕ photoproduction are generated in the Monte Carlo simulation and let N_{gene} be number of the generated events. Apply the same selection cuts discussed in section 3.3 on the Monte-Carlo-generated data, and the number of accepted events then are obtained as N_{accep}. The acceptance is subsequently given as:

$$A_{ccep} = \frac{N_{accep}}{N_{gene}} \tag{3.24}$$

The acceptance may be a function of one or more physical variables such as particle momentum, the path of particle passing throught the detectors, etc. In this analysis, only the dependence of acceptance on E_γ and t is considered and dependence on other variables are considered to give average effect.

In addition, the spin-density-matrix elements that governs the decay angular distribution of K^+K^- would affect the acceptance. The LEPS charged particle spectrometer has larger geometrical acceptance in the horizontal direction and K^+K^- would be more likely to be recorded if they were produced in a plane that is closer to the horizontal plane. As can be seen in Appendix D, since the numbers of the vertically polarized and horizontally polarized incident photons are close to each other in both LD_2 and LH_2 target runs, the overall effect of the spin-dencity-matrix elements is considered to be cancelled out in the unpolarized cross section, which is to be determined in this analysis.

From the result of previous experimental data, in the small t region, it is observed that the differential cross section of diffravtive interaction exhibits an exponential t-dependence in the following form [1]:

$$\frac{d\sigma}{dt} = a \cdot exp\,(b\tilde{t}\,), \tag{3.25}$$
$$\tilde{t} = t + |t|_{min}.$$

where a is the intercept at $t = t_{min}$ and b is the exponential slope. Theoretical approaches to it can be described by VMD applying Regge model and simple pole picture, as discussed in [15] for example. This phenomenological parameterization to describe the near-threshold behavior of differential cross section can also be found such as in [12, 13]. This dynamical formulation of t-distribution is implemented into the event generator for generating ϕ photoproduction events and the exponential slope b needs to be pre-defined.

Different acceptance distributions generated with Eq. 3.25 are obtained seperately for LD_2 coherent, incoherent events and LH_2 events.

3.11 Iteration

As described in section 3.10, the Monte Carlo event generator generates ϕ photoprdoduction events according to Eq. 3.25. But the slope parameter can't be obtained in advance because it's the physical variable to be determined in this analysis work.

Iteration on the analysis is therefore done. Firstly the Monte Carlo event generator generates events with flat t distribution, that is, set exponential slope $b_{input} = 0$. The whole analysis framework is performed and a preliminary slope $b_{obtained}$ is obtained. This $b_{obtained}$ is then input into the event generator and the same procedure repeats to obtain renewed slope parameter iteratively till b_{input} and $b_{obtained}$ converge.

The b after iteration is set to be **15** GeV^{-2} for LD$_2$ coherent events, **4** GeV^{-2} for LD$_2$ incoherent events, and **3.5** GeV^{-2} for LH$_2$ events. These b values are reprodeuced withing an acceptable deviation as repsented in section 4.1.

Chapter 4

Results and discussions

4.1 Results of differential cross section

In this section, the results of the measurement of the differential cross section of for LD_2 coherent, incoherent events and LH_2 events are presented.

4.1.1 Disentanglement of coherent and incoherent events

As discussed in section 3.4, the disentanglement would be achieved by fitting MM_d distribution of LD_2 real data in low $\tilde{t}$ region. The photon energy dependence of the yield of events is measured in nine E_γ bins as defined in Table 3.1.

Table 4.1: The denotation of $\tilde{t}$ bins

$\tilde{t}$ bin	$\tilde{t}$ (GeV)	$\tilde{t}$ bin	$\tilde{t}$ (GeV)
T1	-0.40 - -0.38	T11	-0.20 - -0.18
T2	-0.38 - -0.36	T12	-0.18 - -0.16
T3	-0.36 - -0.34	T13	-0.16 - -0.14
T4	-0.34 - -0.32	T14	-0.14 - -0.12
T5	-0.32 - -0.30	T15	-0.12 - -0.10
T6	-0.30 - -0.28	T16	-0.10 - -0.08
T7	-0.28 - -0.26	T17	-0.08 - -0.06
T8	-0.26 - -0.24	T18	-0.06 - -0.04
T9	-0.24 - -0.22	T19	-0.04 - -0.02
T10	-0.22 - -0.20	T20	-0.02 - -0.00

From the result of t-resolution obtained in section 3.8, the reasonable size of $\tilde{t}$ bin should be larger than 20 MeV^2. In the main framework of this analysis, the bin size of $\tilde{t}$ is chosen to be 20 MeV^2 in the $\tilde{t}$ region set to be $-0.4 < \tilde{t} < 0.0$ as defined in table 4.1. This choice of $\tilde{t}$ range is presumed to be wide enough to include most of the coherent events and is cross checked with the acceptance results discussed in section 4.1.2. The results of using other $\tilde{t}$ range, $\tilde{t}$ bin size and different approaches for evaluating the differential cross section are presented in Appendix B.

Fig. 4.1 shows the MM_d fitting in E8 energy bin and the $\tilde{t}$ range from -0.08 GeV^2 to 0.00 GeV^2 as a demonstration. The MM_d of LD_2 is denoted as solid histograms and the fitting histograms are the dash ones . The χ^2/ndf of the fitting, individual yields of incoherent and coherent components, and corresponding errors are labeled on the plots. The MM_d fitting results in each E_γ and $\tilde{t}$ bin are shown in Appendix E.2.
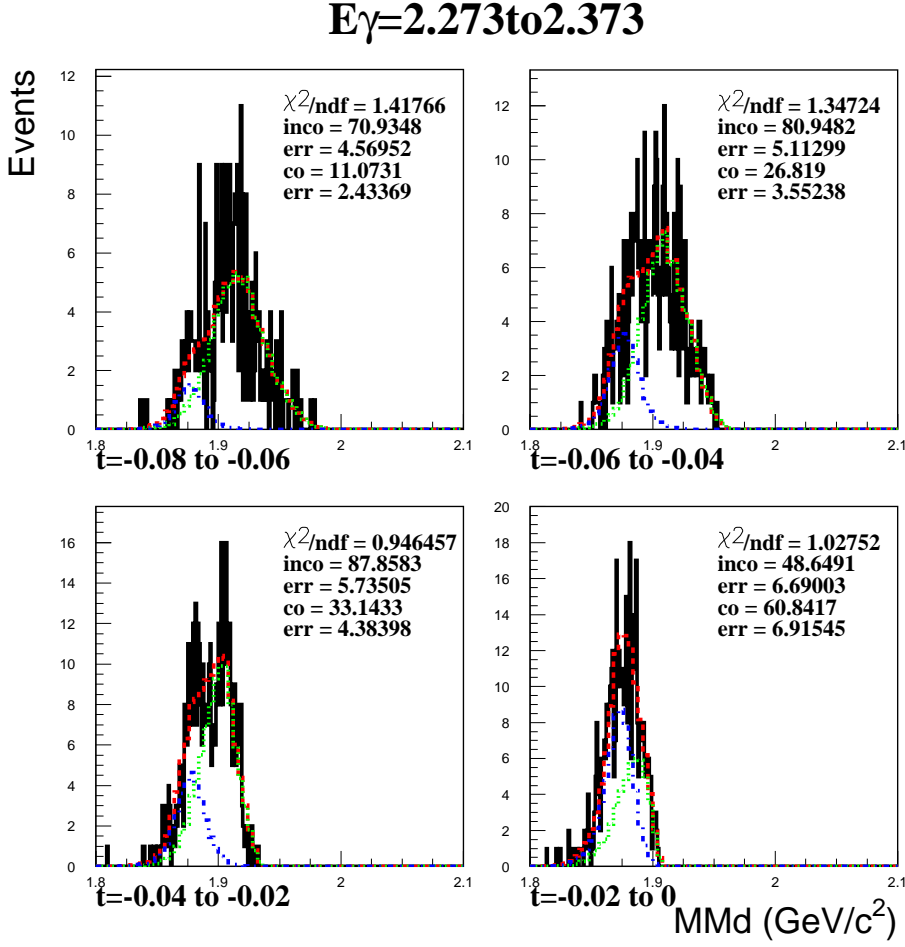
Figure 4.1: Demonstration of MM_d fitting.

As can be seen in Fig. 4.1, the coherent MM_d components of LD_2 increase significantly as $\tilde{t}$ approaches 0. This behavior is consistent with the previous conjecture that the coherent events take place mainly in high $\tilde{t}$ region.

The yield of incoherent and coherent events are extracted as a function of $\tilde{t}$ in each E_γ bin. In the case which $\tilde{t}$ is below -0.4 GeV^2, it is considered that nearly no coherent events survives, therefore the $\tilde{t}$ distribution of LD_2 below -0.4 GeV^2 in each E_γ bin is further attached to the distribution of the disentangled incoherent events to supply distribution of incoherent yield in this $\tilde{t} < -0.4$ GeV^2 region. And the $\tilde{t}$ bin size is change to a wider 0.1 GeV^2 size in this region to provide more statistics.

For the yield of ϕ events of LH_2 data, the $\tilde{t}$ distribution with $\tilde{t}$ bin size 0.1 GeV^2 in the region $-1.0 < \tilde{t} < 0.0$ is made in the conventional E_γ bins.

4.1.2   Acceptance as a function of $\tilde{t}$ in different E_γ bin

The acceptance of the LEPS detector as a function of E_γ bin and $\tilde{t}$ bin for LD_2 coherent, incoherent events and LH_2 events are shown respectively in Fig. 4.2, 4.3, and 4.4. The $\tilde{t}$ bin size is changed in the $\tilde{t}$ region for the acceptance of incoherent events to be in agreement with the distribution of the yield.
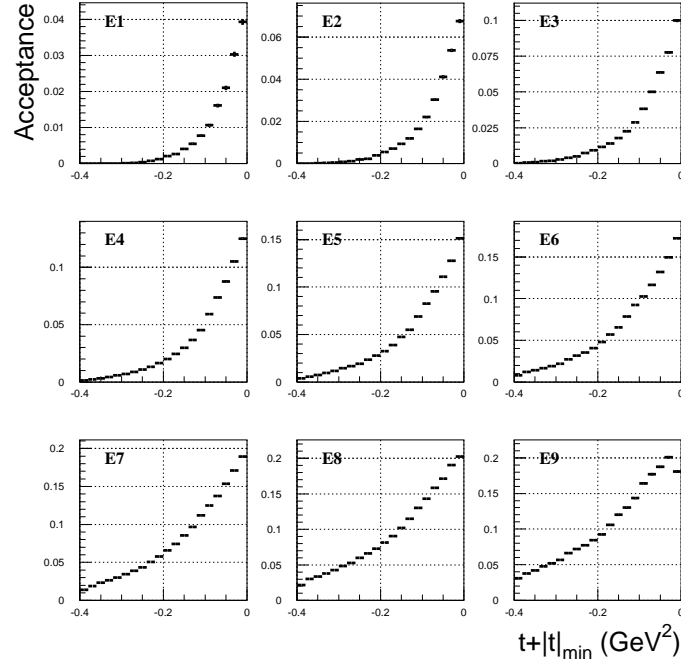
Figure 4.2: Acceptance for the LD_2 coherent events.
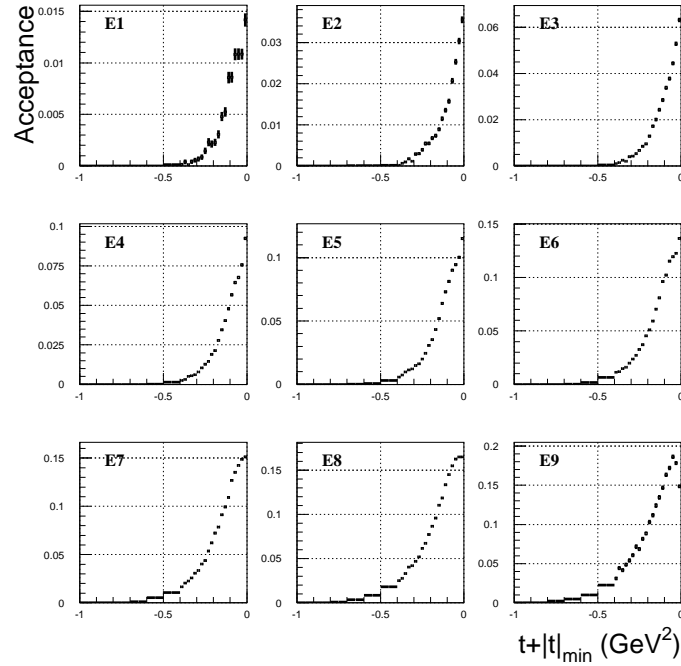
Figure 4.3: Acceptance for the LD_2 incoherent events.
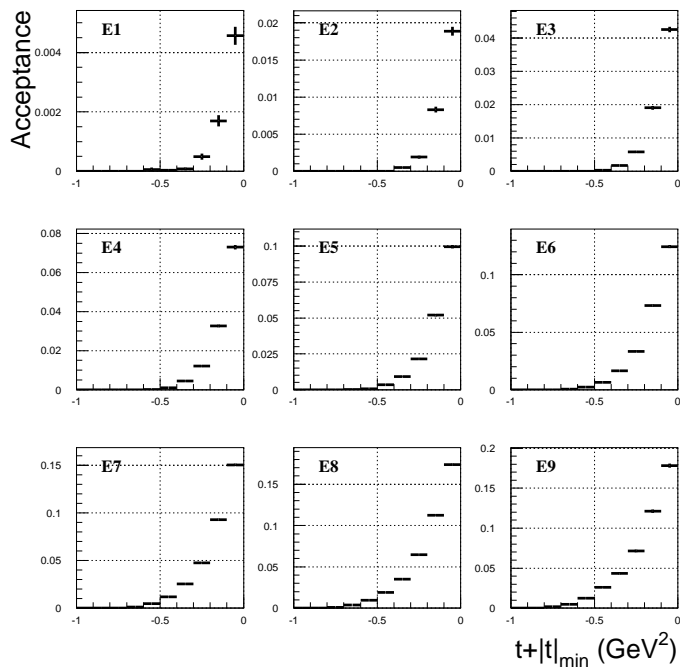
Figure 4.4: Acceptance for the LH$_2$ events.

As shown in the plots, the acceptance exhibits a rapid decay with the decrease of $\tilde{t}$ in all these three different reactions and can be understood by the fact that the set up of LEPS detector is at very forward angle in the direction of the incident photon. With higher $\left|\tilde{t}\right|$, particles after the interaction would deviate more from this direction and are less probable to be detected by the detector.

In Fig. 4.2 the acceptance of coherent interaction drops to the minimum value in the lowest $\tilde{t}$ bin. The acceptance in this $\tilde{t}$ bin is around 0.025 at best. Together with the formulation that the differential cross section drops with decreasing $\tilde{t}$, the presumption that coherent events are fairly to be observed in $-0.4 < \tilde{t} < 0.0$ is ensured.

4.1.3 The fitting of $\tilde{t}$ distribution

The $\tilde{t}$ distributions in different E_γ bin are first normalize by the $\tilde{t}$ bin size. The dN/dt distribution of different interaction is then obtained where N denotes the event yield in each $\tilde{t}$ bin. These dN/dt distributions are fitted with a acceptance-convoluted function in the following form:

$$N_0 \cdot exp(b\tilde{t}\,) \cdot A_{ccep} \tag{4.1}$$

where N_0 and b are the fitting parameters and A_{ccep} is the acceptance. The N_0 and b here individually indicate the intercept at $\tilde{t} = 0$ and the exponential slope of the dN/dt distribution.

The results of the fit to the $\tilde{t}$ distribution is shown in Fig. 4.5, 4.6, and 4.7 and are tabulated in Table 4.2, 4.3, and 4.4. The open circles represent the dN/dt distribution and the dashed lines are the results of the fit. The fitting gives good match with the $\tilde{t}$ distribution in LD$_2$ incoherent case and in LH$_2$ case. For LD$_2$ coherent case on the other hand, discrepancy appears in low $\tilde{t}$ region especially in lower E_γ bins. This may be caused by the fact that the statistics of

coherent events is significantly low in these regions and the yield of events would be easily influenced by statistical fluctuation.

Note that the fitting of LH$_2$ $\tilde{t}$ distribution fails in the E1 bin and unreasonably high χ^2/ndf value is given due to poor statics in this E_γ bin.
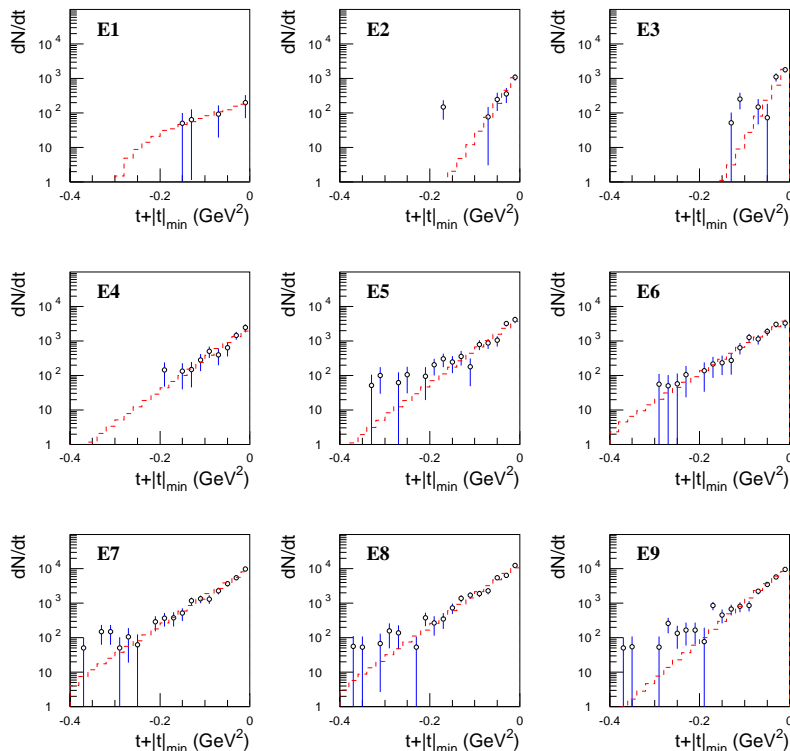
Figure 4.5: LD$_2$ coherent $\tilde{t}$ distribution fitted with acceptance-convoluted function.

Table 4.2: Results of $\tilde{t}$ fitting of LD$_2$ coherent events

E_γ bin	N_0 (events/0.02 GeV^2)	b (GeV^{-2})	χ^2/ndf
E1	4322 ± 3086	-6.592 ± 9.743	0.0526
E2	21171 ± 6871	30.481 ± 13.664	1.1593
E3	27964 ± 6588	40.667 ± 11.286	2.3900
E4	17473 ± 4871	10.972 ± 4.511	0.6076
E5	27333 ± 6147	13.362 ± 3.462	1.4508
E6	24378 ± 4163	11.337 ± 1.999	0.3518
E7	48866 ± 5605	13.051 ± 1.470	0.8535
E8	61163 ± 5899	15.573 ± 1.312	1.2100
E9	56511 ± 6474	20.766 ± 2.180	1.8078
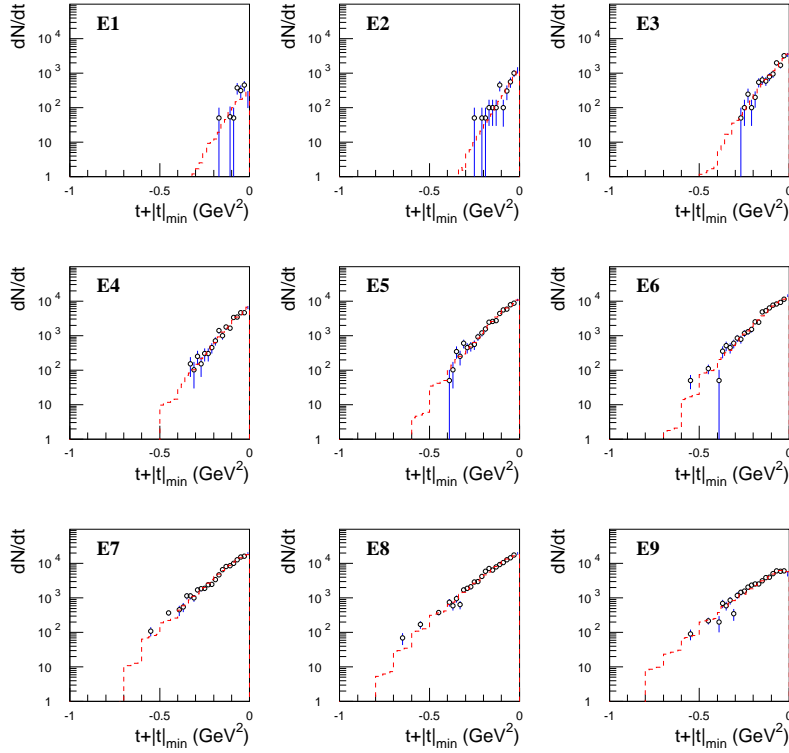
Figure 4.6: LD$_2$ incoherent $\tilde{t}$ distribution fitted with acceptance-convoluted function.

Table 4.3: Results of $\tilde{t}$ fitting of LD$_2$ incoherent events

E_γ bin	N_0 (events/0.02 GeV^2)	b (GeV^{-2})	χ^2/ndf
E1	23550 ± 7939	7.730 ± 5.359	1.8469
E2	38053 ± 8304	10.886 ± 3.696	0.9588
E3	61255 ± 5987	6.216 ± 1.118	0.9009
E4	76332 ± 5282	4.898 ± 0.667	0.9238
E5	97406 ± 5027	4.448 ± 0.441	0.7680
E6	105568 ± 4455	4.538 ± 0.321	1.4274
E7	124344 ± 4670	3.945 ± 0.264	1.5269
E8	113035 ± 3897	3.824 ± 0.215	1.8100
E9	39774 ± 2074	3.052 ± 0.284	1.3777
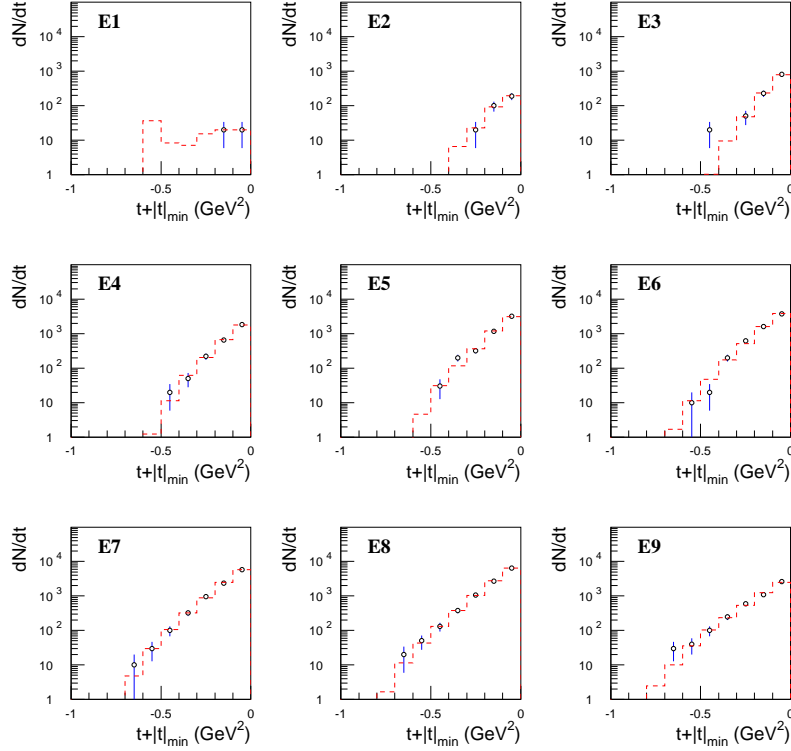
Figure 4.7: LH$_2$ $\tilde{t}$ distribution fitted with acceptance-convoluted function.

Table 4.4: Results of $\tilde{t}$ fitting of LH$_2$ events

E_γ bin	N_0 (events/0.02 GeV^2)	b (GeV^{-2})	χ^2/ndf
E1	2679 ± 3264	-9.873 ± 13.167	9999.0000
E2	9810 ± 3120	-0.835 ± 2.796	0.1098
E3	23273 ± 4088	4.157 ± 1.819	0.9186
E4	27312 ± 2689	1.980 ± 0.802	0.2686
E5	36620 ± 2778	3.033 ± 0.610	1.4597
E6	36895 ± 2228	3.544 ± 0.431	1.6004
E7	45631 ± 2336	3.618 ± 0.358	0.3875
E8	45875 ± 2206	4.168 ± 0.331	0.1551
E9	16260 ± 1225	3.124 ± 0.460	0.9346

4.1.4   The slope parameter

The coverage of E_γ of this this analysis is 1.573 GeV to 2.473 GeV and this is not a wide E_γ range. From previous experimental results [1], the structure of $\tilde{t}$ distribution exhibits no strong energy dependence which can also be observed from Fig. 4.5, 4.6,and 4.7. It is therefore reasonable to presume that the slope parameter b is constant over all the E_γ bins.

This trend of steady slope distribution with E_γ is seen if E9 bin is removed due to the unreliability discussed in section 3.6 and neglect the significant fluctuation in first three E_γ bins as a result of low statistics in these bins.

For this reason, the slope parameters are fitted by a constant distribution to evaluate the average of b and the results are tabulated in Table 4.5. Note that the fit is made with E9 bin excluded.

The energy dependence of the slope parameter is shown in Fig. 4.8, 4.9, and 4.10 by the closed circles for three different data sets. The result of the fit is represented with the open triangle.

Table 4.5: The averaged slope parameters

Data set	b (GeV^{-2})	χ^2/ndf
LD$_2$ Coherent	13.784 ± 0.830	2.2215
LD$_2$ Incoherent	4.136 ± 0.136	1.8940
LH$_2$	3.619 ± 0.192	1.6520
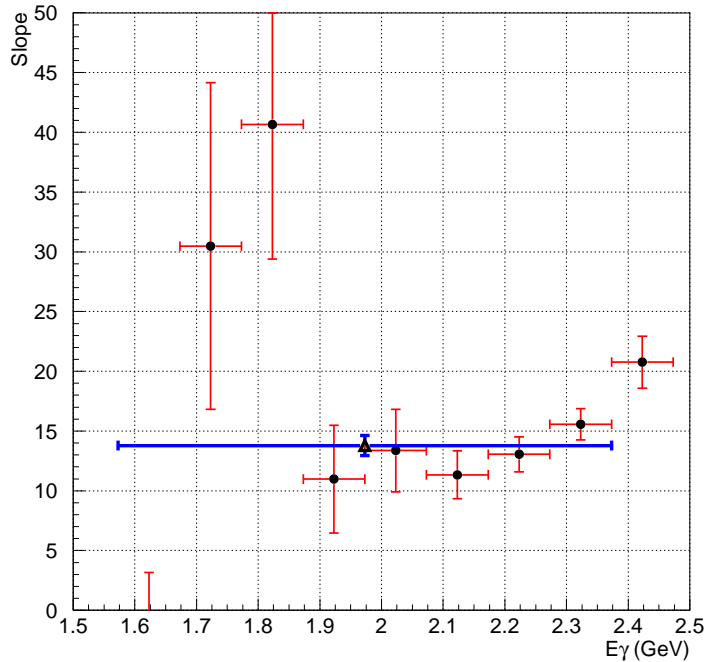
Figure 4.8: Slope parameter of LD$_2$ coherent events
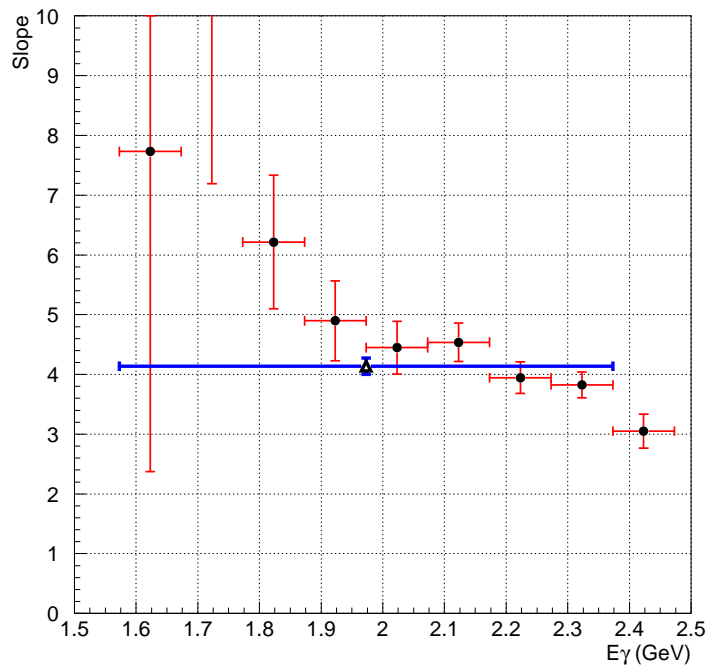
Figure 4.9: Slope parameter of LD_2 incoherent events.
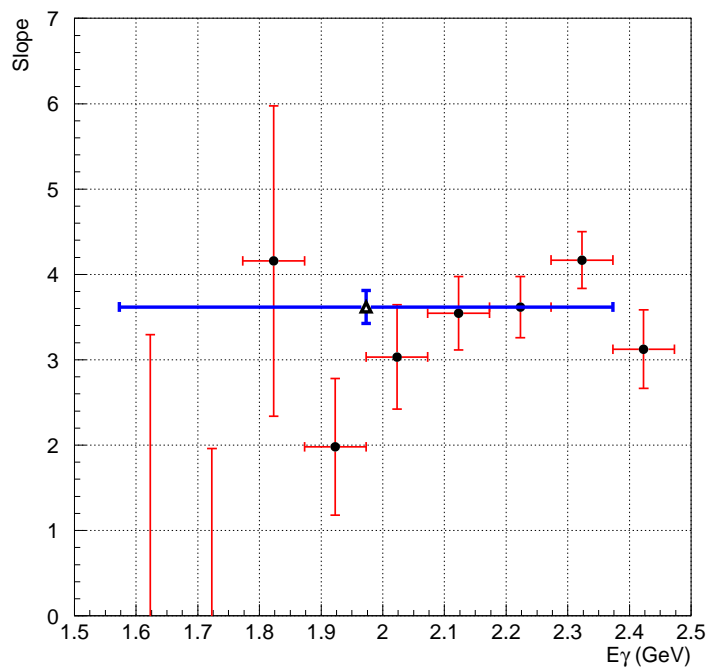
Figure 4.10: Slope parameter of LH_2 events.

4.1.5   Differential cross section

The intercept N_0 obtained from the $\tilde{t}$ fitting needs to be background-subtracted to obtain N_0^ϕ, the intercept of pure ϕ events. With the background-to-signal ratio obtained in section 3.9, N_0^ϕ can be evaluated as:

$$N_0^\phi = N_0 \times (1 - \frac{N_{BG}}{N_{signal}}).$$ (4.2)

Note that this background-subtraction procedure is applied only on intercept of LD$_2$ incoherent events and LH$_2$ events as discussed in section 3.9.

With the intercept N_0^ϕ obtained, the differential cross section at $\tilde{t} = 0$ can be deduced by correcting N_0^ϕ with various normalization constants such as the number of target particles, the number of incident photons, etc.

Also, other correcting factors need to be included, such as the inefficiency of the incident photon beam due to photons interacting with the gas in the beam pipe, the tagger efficiency, and the others. Putting all these normalization constants and correcting factors together, the differential cross section at $\tilde{t} = 0$ GeV^2 is derived as [35]:

$$\frac{d\sigma}{dt}\Big|_{\tilde{t}=0} = \frac{N_0^\phi \cdot F_{norm}}{R_{branch} \cdot N_{target} \cdot (N_{beam} \cdot F_{beam} \cdot \eta_{trans} \cdot P_{ntag1})}$$ (4.3)

where the parameters in the equation are defined as:

- $Fnorm$: The normalization factors to correct tagger PL inefficiency, Tagger SSD dead strips, and $ntag = 1$ inefficiency due to accidental hits.

- R_{branch}: The branching ratio of $\phi \to K^+ K^-$.

- N_{target}: The number of target nucleons.

- N_{beam}: The number of tagged photons.

- F_{beam}: The fraction of the number of photons at each energy bin.

- η_{trans}: The transmission rate of photon beam from storage ring to the target.

- P_{ntag1}: The probability of $ntag = 1$ after correcting the inefficiencies of tagger.

From Eq. 4.3 the differential cross section at $\tilde{t} = 0$ is derived in the unit of μb. The list of the value of each parameter for LD$_2$ and LH$_2$ data is included in Appendix D.

The results of the energy dependence of differential cross section at $\tilde{t} = 0$ is shown in Fig. 4.11, 4.12, and 4.13 and are also tabulated in Table 4.6, 4.7, and 4.8. With the fluctuation in few E_γ bins, different patterns of $d\sigma/dt|_{\tilde{t}=0}$ in each kind of event arise clearly.
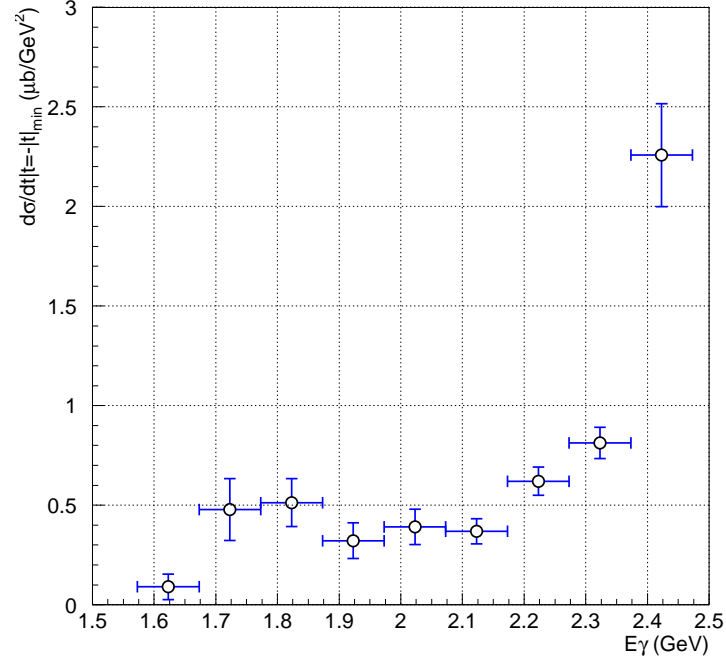
Figure 4.11: Differential cross section at $\tilde{t} = 0$ of LD_2 coherent events.

Table 4.6: Differential cross section at $\tilde{t} = 0$ of LD_2 coherent events

E_γ bin	$d\sigma/dt|_{\tilde{t}=0}$ ($\mu b/\text{GeV}^2$)
E1	0.090 ± 0.064
E2	0.478 ± 0.155
E3	0.513 ± 0.121
E4	0.322 ± 0.090
E5	0.391 ± 0.088
E6	0.370 ± 0.063
E7	0.620 ± 0.071
E8	0.812 ± 0.078
E9	2.258 ± 0.259
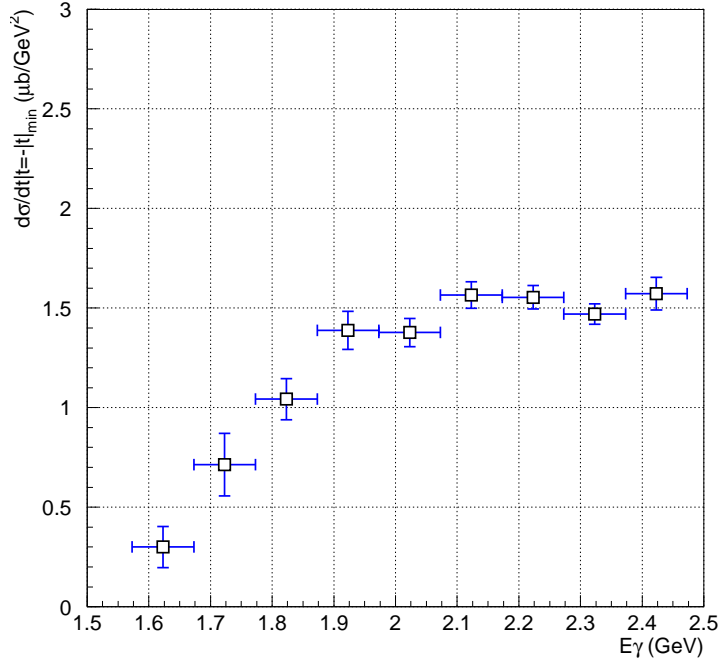
Figure 4.12: Differential cross section at $\tilde{t} = 0$ of LD_2 incoherent events.

Table 4.7: Differential cross section at $\tilde{t} = 0$ of LD_2 incoherent events

E_γ bin	$d\sigma/dt|_{\tilde{t}=0}$ $(\mu b/\text{GeV}^2)$
E1	0.300 ± 0.103
E2	0.714 ± 0.158
E3	1.043 ± 0.103
E4	1.388 ± 0.096
E5	1.377 ± 0.071
E6	1.566 ± 0.066
E7	1.554 ± 0.058
E8	1.470 ± 0.051
E9	1.572 ± 0.082
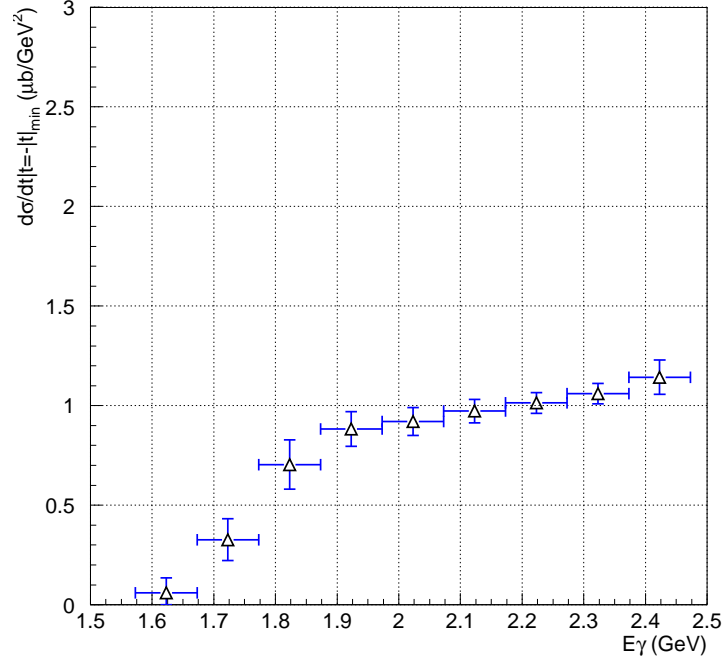
Figure 4.13: Differential cross section at $\tilde{t} = 0$ of LH$_2$ events.

Table 4.8: Differential cross section at $\tilde{t} = 0$ of LH$_2$ events

E_γ bin	$d\sigma/dt\vert_{\tilde{t}=0}$ ($\mu b/\mathrm{GeV}^2$)
E1	0.061 ± 0.074
E2	0.327 ± 0.105
E3	0.704 ± 0.124
E4	0.883 ± 0.087
E5	0.920 ± 0.070
E6	0.973 ± 0.059
E7	1.014 ± 0.052
E8	1.061 ± 0.051
E9	1.143 ± 0.086

4.2   Discussions

4.2.1   The slope parameter

From section 4.1.4, it is observed that the slope parameter exhibits no strong energy dependence for the three different kind of reactions. In Fig. 4.14, the average slope parameters b as a function of photon energy obtained from LD_2 coherent, incoherent, and LH_2 events are presented with the open circle, the open square, and the open triangle.
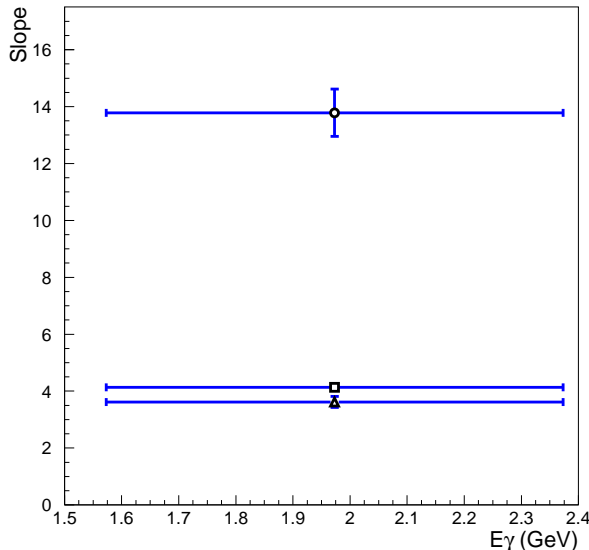
Figure 4.14: Slope parameters as a function of photon energy.

The slope parameter of LD_2 coherent events is about 14 GeV^{-2}, and basically in the range of 3-5 for interaction with nucleons. As can be seen, the slope of LD_2 coherent events is significantly higher than those of LD_2 incoherent and LH_2 events. This feature of large t-slope can be understood by the form factor of deuteron. Because the charge distribution of deuteron is wider in space than that of nucleons, the form factor of deuteron would exhibits a steeper momentum-transfer dependence. The result is consistent with the theoretical prediction [18] and the form factors for the natural exchange amplitude $S_{1,0}^N$ discussed in Appendix C.

4.2.2   Differential cross section

The differential cross section at $\tilde{t} = 0$ GeV^2 as a function of photon energy of LD_2 coherent, incoherent, and LH_2 events are shown in Fig 4.15 and are represented respectively with open circles, open squares, and open triangles. Further, the results of previous LEPS experiment using 50 mm LH_2 target [12] is also overlaid with closed circles. Note that results of E9 bin is abandoned.

From section 4.1.3, the differential cross section exhibit forward peaking shape at the forward angles within the LEPS acceptance of very forward direction for LD_2 coherent, incoherent, and LH_2 interactions. This fact confirms that in ϕ photoproduction at forward angles, the diffractive t-channel exchange is the dominate contribution.

As to the isotopic effect of π-η interference, since π and η are isovector and isoscalar particles, the π pp and η pp coupling have the same sign while π nn and η nn are of the opposite
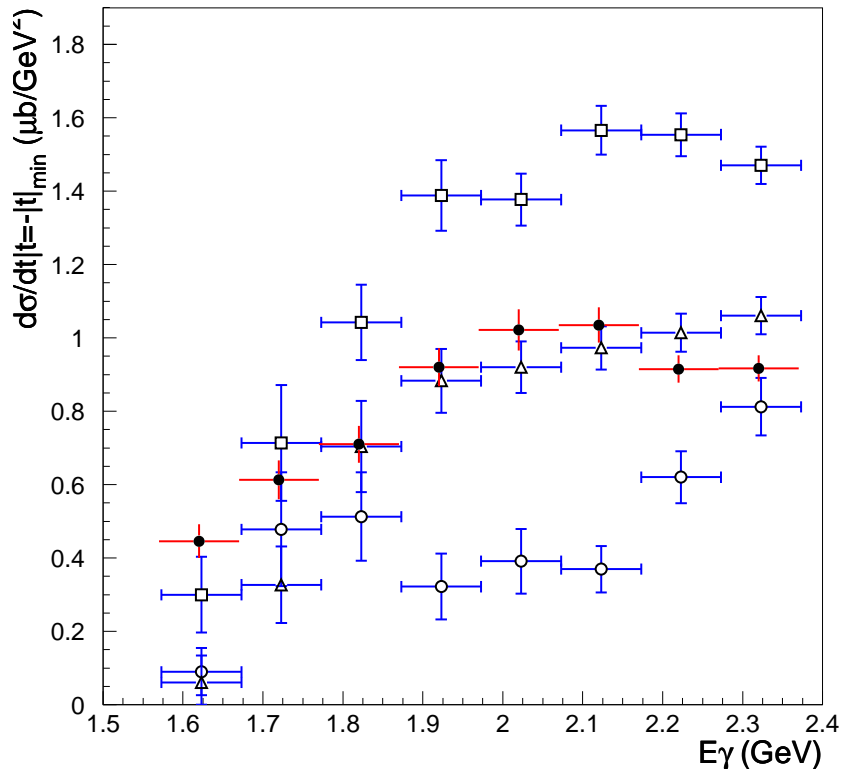
Figure 4.15: Differential cross section at $\tilde{t} = 0$ as a function of photon energy.

sign. Therefore a constructive interference between π-exchange and η in the $\gamma + p \rightarrow \phi + p$ interaction and destructive interference in the $\gamma + n \rightarrow \phi + n$ interaction are expected. In the LD_2 incoherent reactions, the measurement is performed without identifying $\gamma + p \rightarrow \phi + p$ and $\gamma + n \rightarrow \phi + n$, so the experimental observable is considered to be the coherent sum of these two reaction channels. If there were no π-η interference, the differential cross section at $\tilde{t} = 0$ of LD_2 incoherent events would close to that of the interaction with nucleons doubled, which is not seen in Fig 4.15. This fact suggests the cross section of $\gamma + n \rightarrow \phi + n$ is 20-30% lower than that of $\gamma + p \rightarrow \phi + p$ interaction which is somehow inconsistent with the prediction of [9] but may still provide information of π- and η-exchange contribution to be further analyzed.

The differential cross section at $\tilde{t} = 0$ of LD_2 coherent events increases with the photon energy. For the differential cross section at $\tilde{t} = 0$ of LD_2 incoherent events and LH_2 coherent, although not so significant for the LH_2 events, local maximum similar to the previous LEPS result is seen around $E_\gamma = 2.2$ GeV. Together with the analysis on decay asymmetry discussed in [36] which shows the dominating natural-parity exchanges contribution, the scenario of manifestation of other exchanges of natural-parity particles such as the daughter Pomeron exchange is suggested.

Since the formulation of differential cross section of LD_2 coherent events is basically different from that of the interaction with nucleons by the form factor of deuteron, the results of coherent interaction and interaction with nucleons can be compared on the same basis by correcting the differential cross section of coherent events with deuteron form factor. In Fig. 4.16, open circles represent the differential cross section of LD_2 coherent events corrected by the deuteron form

factor and related phase-space factors discussed in Appendix C.
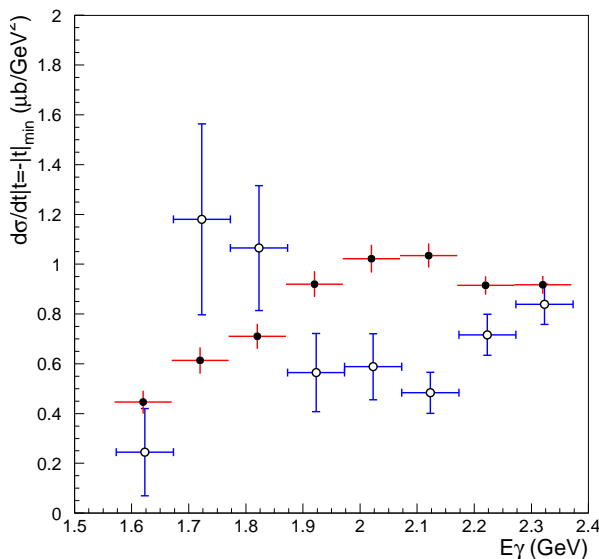
Figure 4.16: Corrected differential cross section at $\tilde{t}$ =0 of LD$_2$ coherent events comparing with LH$_2$ result.

Compared to the result of LH$_2$ events of [12] represented with closed circles, the corrected differential cross section of LD$_2$ coherent events is lower than that of the LH$_2$ events. This is resonable because of the absence of π-meson exchange in the coherent interaction. However, the trend of the result of LD$_2$ coherent events doesn't drop with the photon energy but rather retains at the value around 0.6 μb. As discussed before, the Pomeron exchange is expected to take the majority of the particle exchange process if the π exchange is eliminated. Pomeron exchange contribution is understood to go down with decreasing photon energy and therefore the observed non-decreasing behavior can't be simply interpreted by the scenario of a dominance of natural-parity Pomeron exchange. According to the decay-asymmetry analysis of **??**, the LD$_2$ coherent interaction is dominated by natural-parity exchange process. Thus, the non-decreasing behavior can't caused by unnatural-parity η exchange but comes from other natural-parity particle exchange.

In the future work, since the LD$_2$ coherent reaction is conjectured to be dominated by natural-parity exchanges. The form factors $\mid S_{1.0}^{N}\mid^2$ of deuteron can be implemented into the predicted cross section of $\gamma + p \rightarrow \phi + p$ at $\tilde{t} = 0$ from Pomeron exchange and any deviation from this measurement of LD$_2$ coherent events will indicates the existence of other process of natural-parity exchange at E_γ =1.573 - 2.373 GeV. Further, by using polarized target, more informative observables such as the beam-target asymmetry may be obtained [6, 9, 18]. New measurement at higher energies ($E_\gamma > 2.4$ GeV) can also be performed to establish an overall exhibition of the non-monotonic structure of the cross section near threshold.

Chapter 5

Summary

The differential cross section of the photoproduction of ϕ meson from deuterium target has been studied and compared with the results from hydrogen target in the energy range from the production threshold to $E_\gamma = 2.4$ GeV.

The diffractive photoproduction of ϕ meson provides an good opportunity to observe non-conventional particle-exchange processes due to the OZI suppression. By using the LD_2 target, natural-parity exchange contribution can be further extracted by isospin conservation. Isospin effect can also be studied

Clear contribution from coherent reactions was observed in the LD_2 MM_d spectra, and therefore the disentanglement was achieved by fitting the MM_d spectra with those of Monte-Carlo-simulated coherent and incoherent events in each E_γ and $\tilde{t}$ bin. Various examinations were done to verify the validity of the Monte-Carlo simulation for disentanglement. Also, the background subtraction, acceptance, and other issues need to be nailed down were studied with Monte-Carlo simulation.

The properly determined Monte-Carlo-simulated MM_d spectra fitted the real data with reasonably good agreement. For the disentangled LD_2 coherent, incoherent events, and the LH_2 events, no strong energy dependence was observed. The LD_2 coherent differential cross section was observed to have a large t-slope which can be understood by the form factor of deuteron. And the differential cross section at $\tilde{t} = 0$ of LD_2 coherent events shows a constant increase with the photon energy.

As to the differential cross section of LD_2 incoherent events, the result shows a strong isospin effect. Together with the differential cross section of LH_2 events, consistent exponential slopes were obtained and the peaking structure around $E\gamma = 2.2$ GeV observed in the previous LEPS analysis with liquid hydrogen target is also shown in both kinds of reactions. Together with the study on decay asymmetry of another LEPS analysis, the presence of the peaking structure in the cross section may be interpreted as the manifestation of additional natural-parity exchange processes, such as the daughter Pomeron trajectory.

In the future, the comparison of the predicted differential cross section of $\gamma + p \rightarrow \phi + p$ at $\tilde{t} = 0$ from Pomeron exchange and that of the LD_2 coherent interaction can be proceeded to discriminate the possible natural-parity contribution. Further, more informative observables such as the beam-target asymmetry may be obtained by using polarized target. New measurement at higher energies is also crucial to pin down and establish the non-monotonic-increase structure of the cross section near threshold.

Appendix A

Survey of stability of momentum resolution

The particle identification (PID) involves the determination of the momentum and the time of flight of different particles. The momentum resolution is therefore involved in the procedure of PID. Here the momentum resolution is examined in different runs to see if there is any run dependence of it by utilizing the same framework as discussed in [23].

From experiment, the momentum p of a particle can be measured by the bending angle of it when passing through the bending magnet. And the flight-path length and the time of flight (TOF) together gives the velocity β of the particle. With these two information the mass m of the particle can be determined as:

$$m = [p^2(\frac{1 - \beta^2}{\beta^2})]^{1/2} \tag{A.1}$$
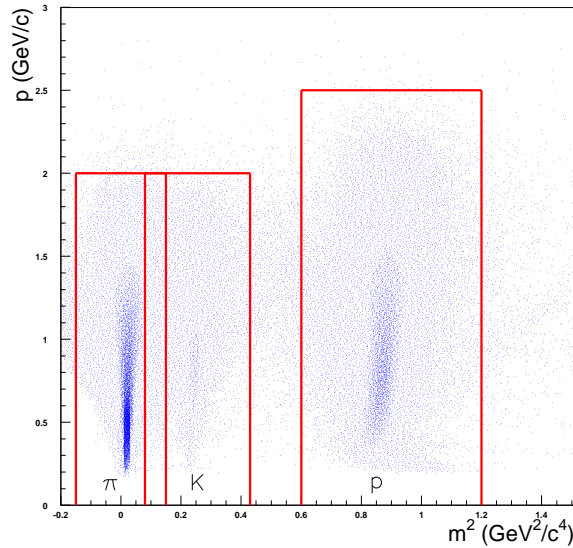
Figure A.1: Scatter plot of Momentum square and momentum.

The 2-d scatter plot of mass square and particle momentum is shown in Fig. A.1 using the data taken from LD_2 target events. Bands representing pions, kaons, and protons can be seen

separately. It can also be seen that the distribution of the band is not uniform at different momentum and this non-uniformity comes from the resolution of momentum and TOF.

Define the width of the band as σ_{m^2} and this reconstructed mass resolution can be parameterized as [37]:

$$\sigma_{m^2}^2 = 4m^4(\frac{\sigma_p}{p})^2 + \frac{4p^4}{\beta^2}(\frac{\sigma_{TOF}}{L})^2. \tag{A.2}$$

where σ_p, σ_{TOF}, and L are the momentum resolution, TOF resolution, and the flight-path length.

To obtain the momentum resolution by utilizing Eq. A.2, the mass resolution as a function of particle momentum need to be obtained first. The bands corresponding to each type of particle is cut out as defined by the box region depicted in Fig.A.1. The selected mass distributions are then sliced into different momentum region as defined in Table A.1.

Table A.1: The definition of momentum slices.

Particle	Range of m (GeV^2)	Range of p (GeV/c)	Number of slices
Pion	-0.15 - 0.15	0.0 - 2.0	20
Kaon	0.08 - 0.43	0.0 - 2.0	20
Proton	0.60 - 1.20	0.0 - 2.5	25

Each slice of mass distribution is then fitted with a Gaussian distribution plus a first-order polynomial as is illustrated in Fig. A.2 by taking the LD$_2$ proton-band case for example.
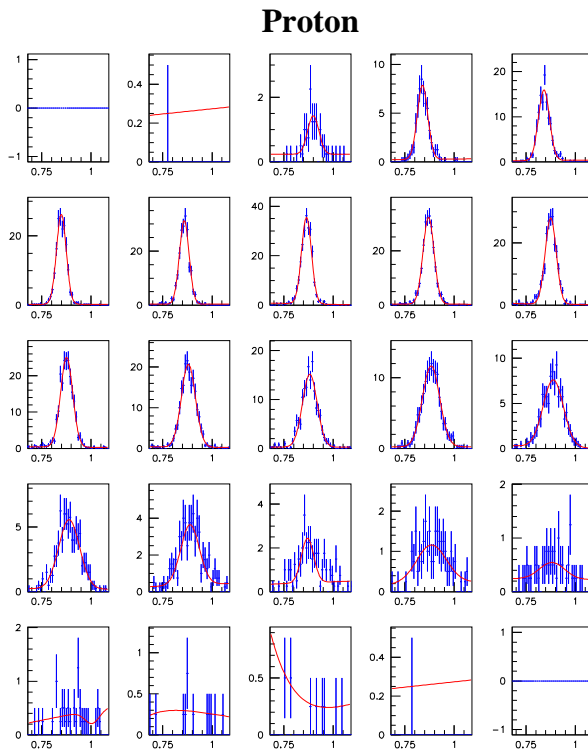
Figure A.2: Fitting of proton mass distribution in each momentum slice.

The mean value and the width of the Gaussian fitting in each momentum region are then obtained from the fitting. The Gaussian width values are assigned to be the mass resolution σ_m and the momentum resolution can subsequently be derived.

The momentum resolution σ_p in Eq. A.2 can be decomposed into two terms relating to spectrometer resolution and multiple scattering separately. The momentum resolution and TOF resolution are thus parameterized as:

$$(\frac{\sigma_p}{p})^2 = a_1^2 \cdot p^2 + \frac{a_2^2}{\beta^2},\tag{A.3}$$

$$a_3 = \frac{\sigma_{TOF}}{L}.\tag{A.4}$$

The parameter a_1 dominates in high p region and is related to the spectrometer resolution. It would be altered by the aging of sensing wire, the variation of the gas of the chamber, and other possibles effects. The parameter a_2, on the other hand, dominates in low p region and is affected by the multiple scattering process relating to the material through which particle passes.

Substitute Eq. A.1, A.3 and A.4 into Eq. A.2, the mass resolution can be expressed as:

$$\sigma_{m^2}^2 = 4m^2p^2 \cdot a_1^2 + 4m^4(1 + \frac{m^2}{p^2}) \cdot a_2^2 + 4p^2(m^2 + p^2) \cdot a_3^2.\tag{A.5}$$

Set a_1, a_2, and a_3 as fitting parameters, the measured Gaussian widths in different momentum region are fitted with Eq. A.5 as a function of momentum p as is shown in Fig. A.3 by using LD_2 proton-band case still as an illustration.
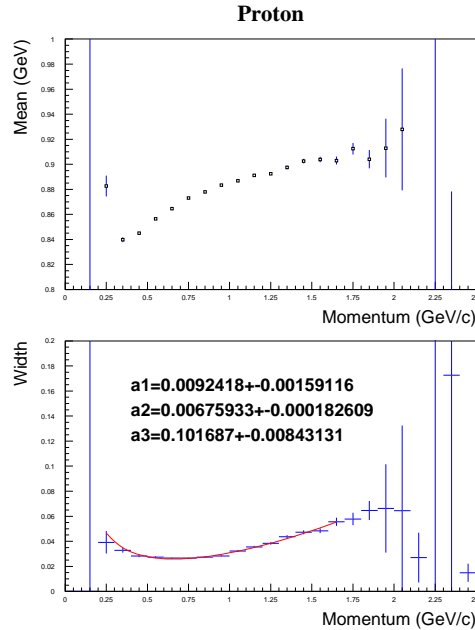
Figure A.3: Fitting of Gaussian width of the mass distribution.

The three parameters obtained by different particle band given by the fitting are then shown in Fig A.4, A.5, and A.6. Putting LD_2 target runs and LH_2 target runs all together, the parameters are presented in different runs with the LD_2 target runs denoted by closed circles and LH_2 target runs denoted by open circles.

As shown in Fig. A.4, A.5, and A.6, the momentum resolution related parameters; a_1 and a_2, exhibits no significant run dependence and fluctuates around a stable value within error bar in all three kind of particle bands utilized.

Neglect the results from low-statics kaon band, one problem is that the values a_2 from pion band are almost zero. This may be under stand by the fact that π is relatively light particle and the probability of multiple scattering for π is low. Therefore the pion band is not sensitive enough to produce proper a_2.

Another problem is that the parameters shouldn't depend on which particle band used. But as can be seen that these three parameters derived from pion, kaon, and proton differ from each other. The explanation for this problem is not well understood in this analysis work. But even though this inconsistency appears, the stability of the momentum is evidenced.
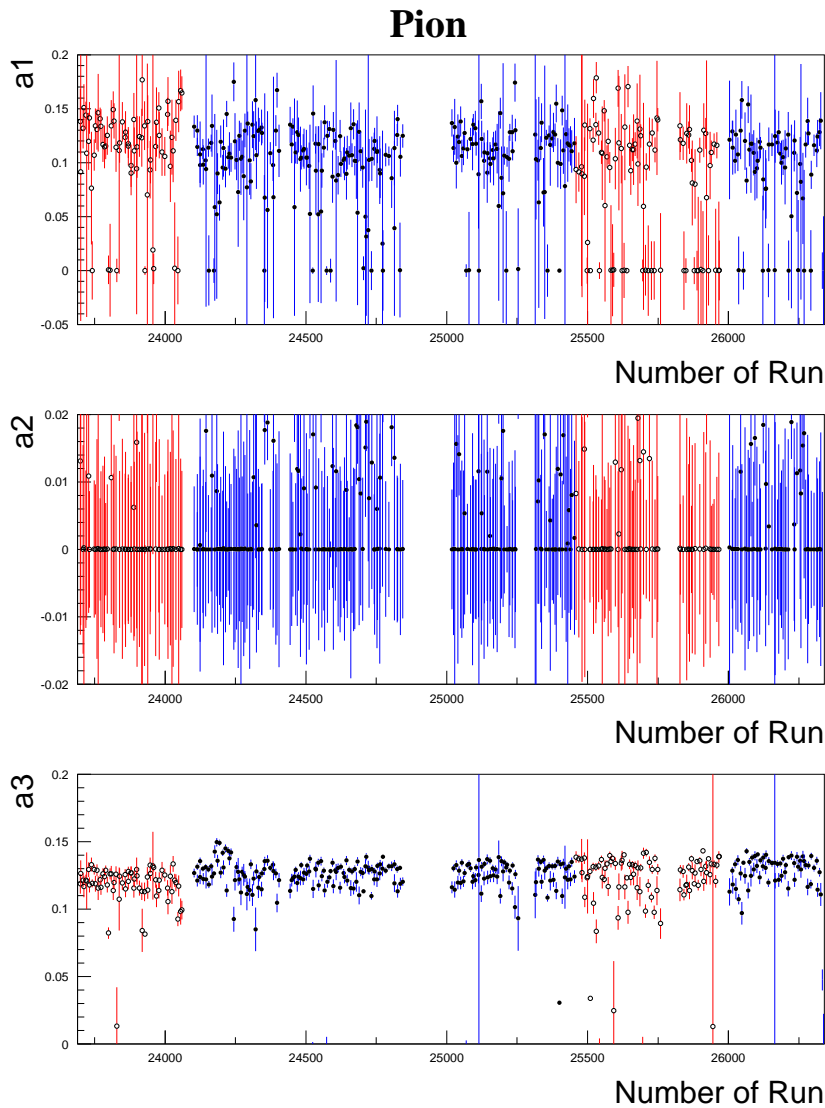
Figure A.4: Three fitting parameters in different runs evaluated with pion band.
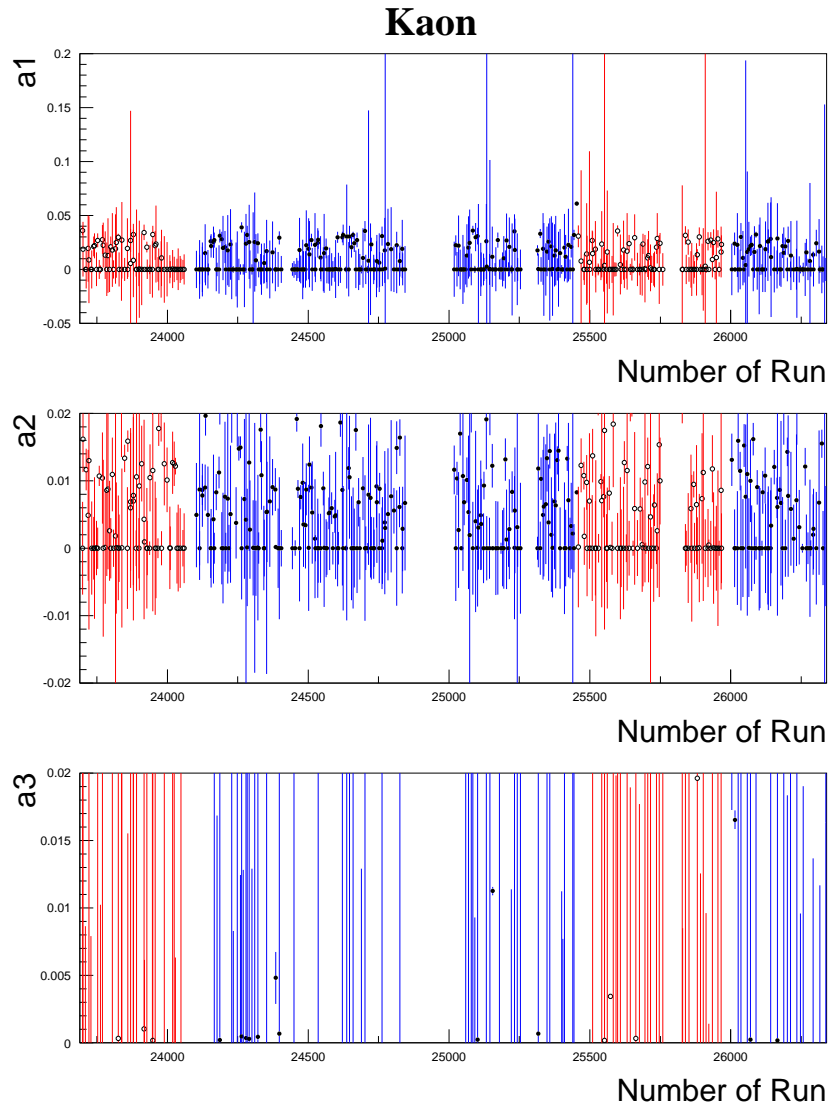
Kaon

Figure A.5: Three fitting parameters in different runs evaluated with kaon band.
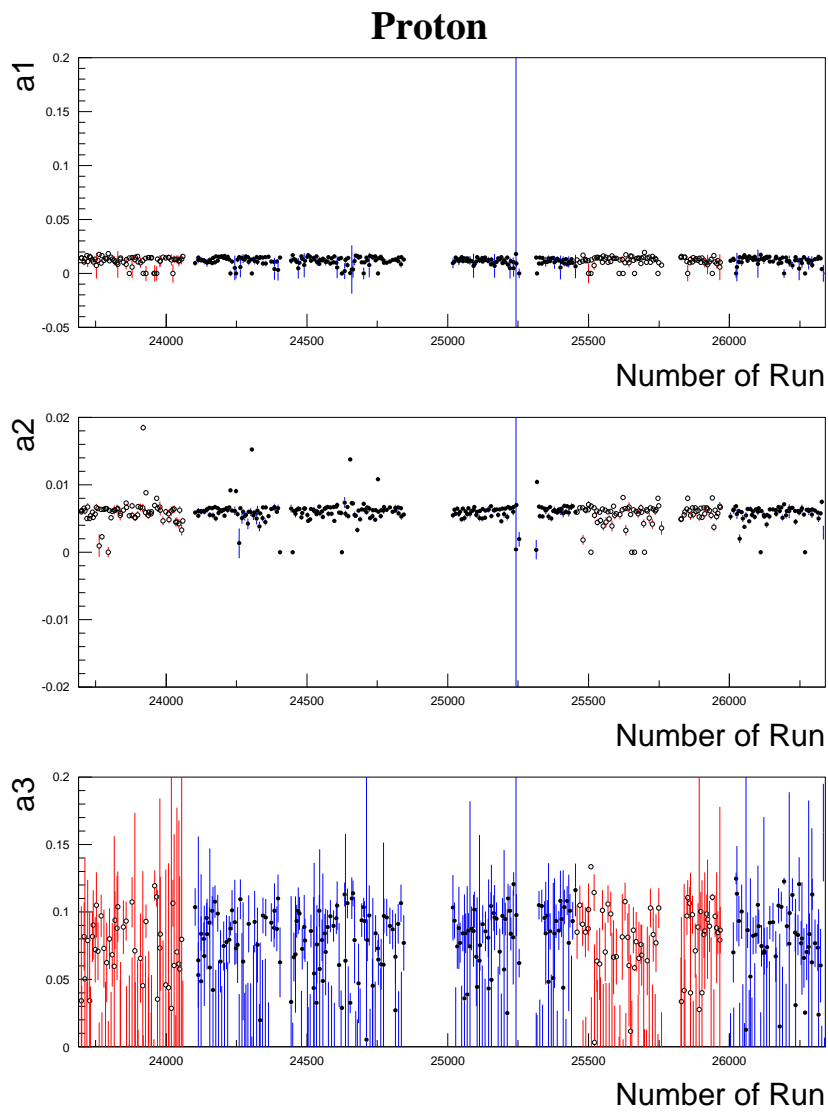
Figure A.6: Three fitting parameters in different runs evaluated with proton band.

Appendix B

Systematic examinations

Different systematic examination is explained in this appendix to test the authenticity of the differential cross section. Consistency between different approaches is shown.

B.1 Cross check on disentanglement

If the Monte-Carlo simulation is valid and reliable, the disentanglement should not depend on whether it is MM_p or MM_d spectra to be fitted. Therefore, the same procedure used to disentangle coherent and incoherent contribution by MM_d fitting is applied on MM_p .
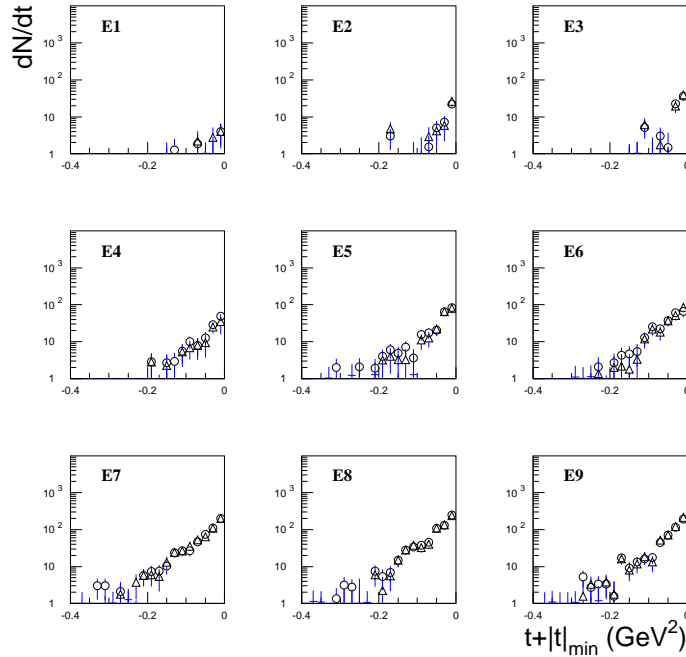
Figure B.1: LD_2 coherent $\tilde{t}$ distribution disentangled from MM_p and MM_d spectra.

In Fig. B.1 and Fig. B.2, LD_2 coherent, incoherent $\tilde{t}$ distribution in each E_γ bin are shown with the open circles representing the MM_d disentangled components and open triangles representing MM_p disentangled ones. Within error bar, clear consistency is verified between the

disentanglement by MM_p and by MM_d fitting.
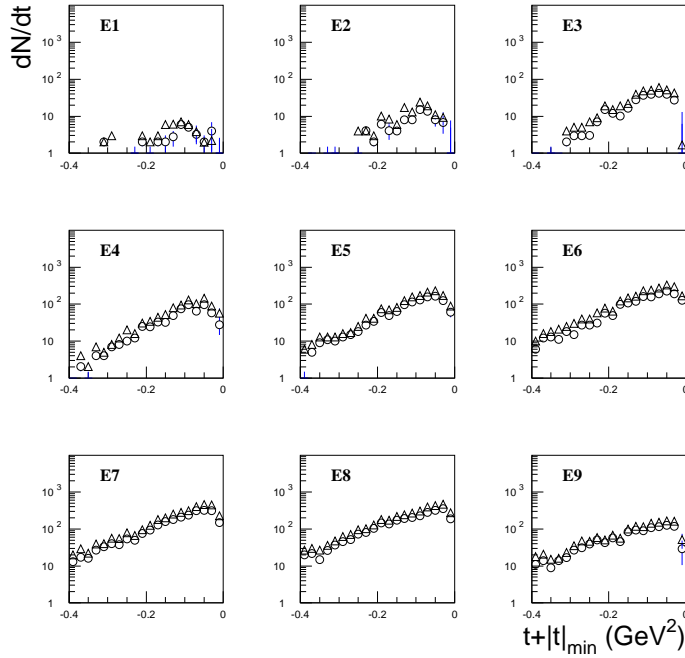
Figure B.2: LD_2 incoherent $\tilde{t}$ distribution disentangled from MM_p and MM_d spectra.

Since the disentanglement by MM_p and MM_p show good agreement with each other, the MM_d and MM_p spectra from real data (backgrounds within) must be dominantly contributed from demanded coherent and incoherent events and can thus be successfully extracted by the non-background-contaminated Monte-Carlo simulated events. This indicates the fact of rare contamination of backgrounds in the events before background subtraction.

B.2   Bin-size dependence

The choice of range and bin size of $\tilde{t}$ to perform disentanglement of LD_2 coherent and incoherent events is rather arbitrary.

The distribution of coherent events concentrates in low $\tilde{t}$ region and is considered to be well included if this $\tilde{t}$ region is set to be wide enough. But if the t range is set too wide, the statistics of MM_d distribution in low $\tilde{t}$ part would become too poor to give reasonable MM_d fitting due to the exponential $\tilde{t}$ dependence of the differential cross section.

The bin size of $\tilde{t}$ is limited to the t resolution. With smaller $\tilde{t}$ bin size, the dependence on $\tilde{t}$ of the yield of events can be obtained in more t-bins and provides more degrees of freedom as constraint of the exponential fitting. The problem still is that with smaller $\tilde{t}$ bin size, the statistics of MM_d in each $\tilde{t}$ bin would decrease and thus the MM_d fitting would provide larger error.

The result of differential cross section by different range and the bin size of $\tilde{t}$ is presented with two different options listed in Table. B.1

Table B.1: Different options of range and bin size of $\tilde{t}$

	$\tilde{t}$ range (GeV^2)	$\tilde{t}$ bin size (GeV^2)	Number of $\tilde{t}$ bins
Option 1	-0.3 - 0.0	0.03	10
Option 2	-0.4 - 0.0	0.04	10

B.3   Different approaches

As is discussed, the structure of the $\tilde{t}$ distribution is not sensitively dependent on E_γ energy which is shown in sub-section 4.1.4. Another way of fitting parameterization referred to as **common-slope fitting** is then made by setting the b parameter to be a single parameter among all the E_γ bins. This method is also employed in [22].

Common-slope fitting in a sense helps to correct the fitting result in the low E_γ bins of poor statistics by utilizing the constraint provided by the higher E_γ bins. However, it is shown in section 3.6 that the result in E9 bin is rather untrustful due to the breakdown of E_γ smearing. The E9 bin is therefore forsaken to avoid the influence it would bring into the over all fitting.

Due to the low statistics in low E_γ bins shown, another approach to merge the merge the lowest three E_γ bins is performed. The E1, E2, and E3 bins are merged to **E*** bin of range 1.573 GeV to 1.873 GeV with other E_γ bin definition kept the same. And then the same analysis process such as acceptance evaluation and disentanglement is made. The approaches in all are summarized as:

- **Approach 1**: Conventional nine E_γ binning, slope as an unstrained parameter.

- **Approach 2**: Conventional nine E_γ binning, common slope.

- **Approach 3**: E1, E2, and E3 are merged to be E*, slope as an unstrained parameter.

- **Approach 4**: E1, E2, and E3 are merged to be E*, common slope.

Here, the results of $\tilde{t}$ fitting using another approach combining with other bin size of $\tilde{t}$ are presented in various plots. Note that in the plots of LD$_2$ coherent and incoherent events, the results of different $\tilde{t}$ bin size are overlaid with the convention:

- **Open squares**: 0.02 GeV^2

- **Open circles**: 0.03 GeV^2

- **Open triangles**: 0.04 GeV^2
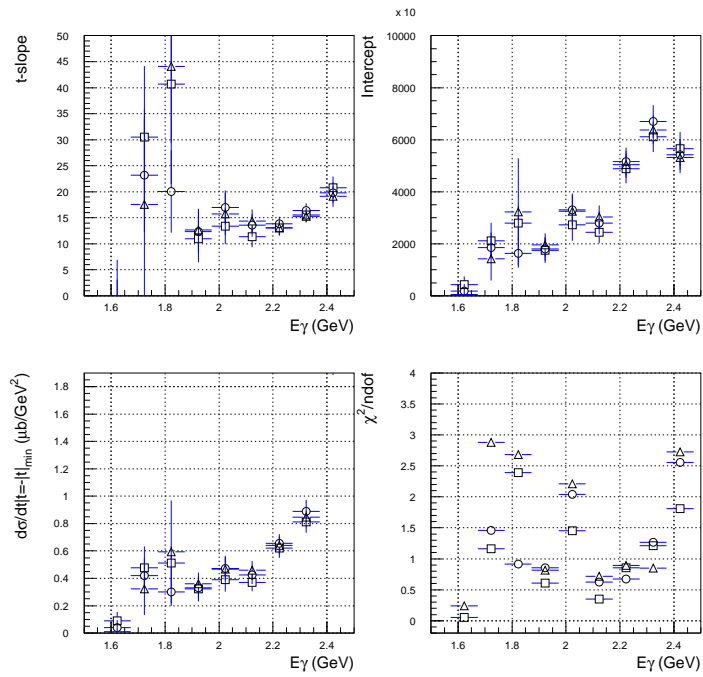
Figure B.3: Results of Approach 1 of LD_2 coherent events.
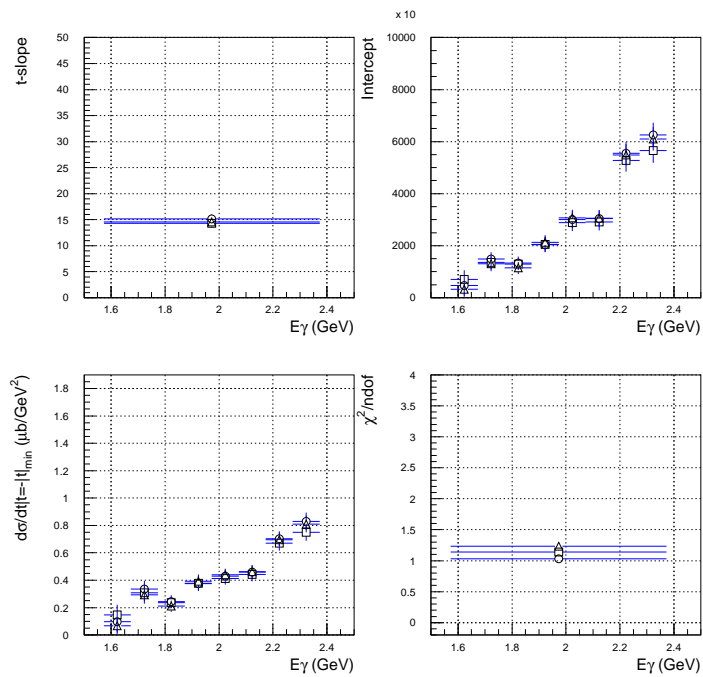
Figure B.4: Results of Approach 2 of LD_2 coherent events.
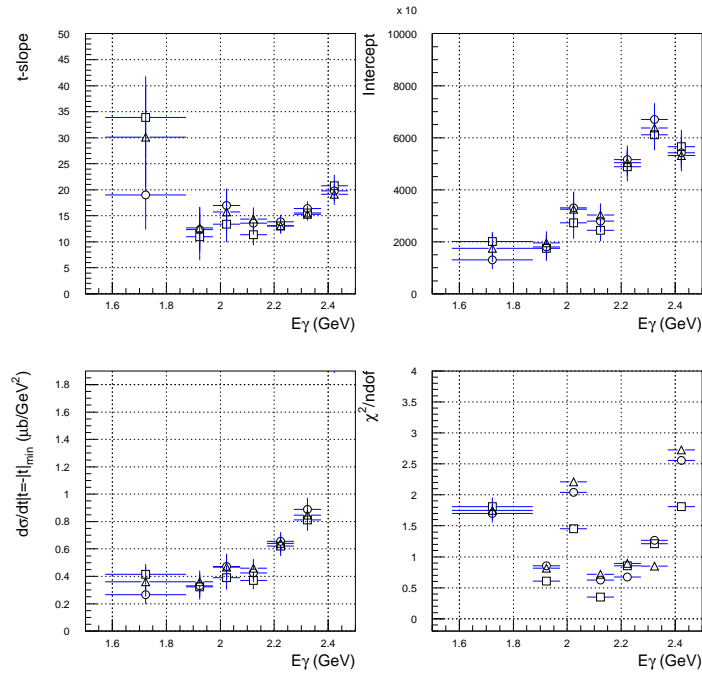
Figure B.5: Results of Approach 3 of LD_2 coherent events.
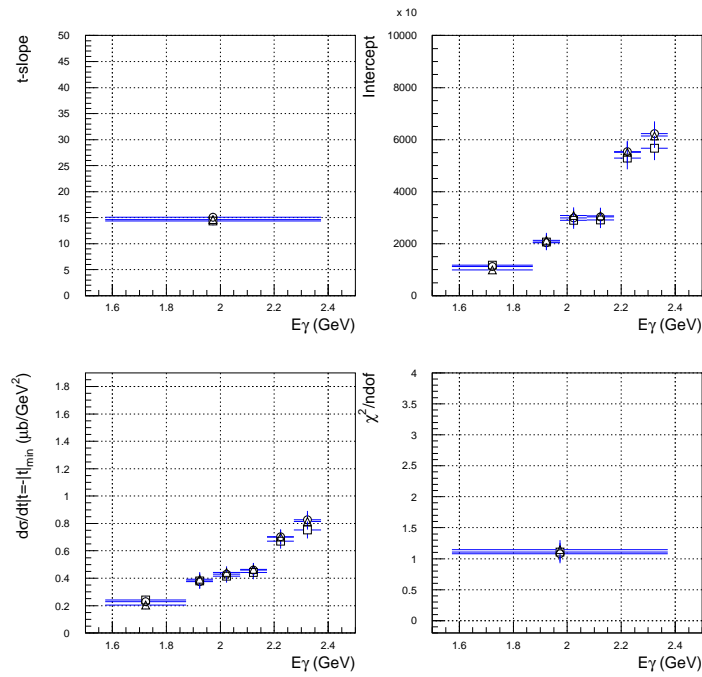
Figure B.6: Results of Approach 4 of LD_2 coherent events.
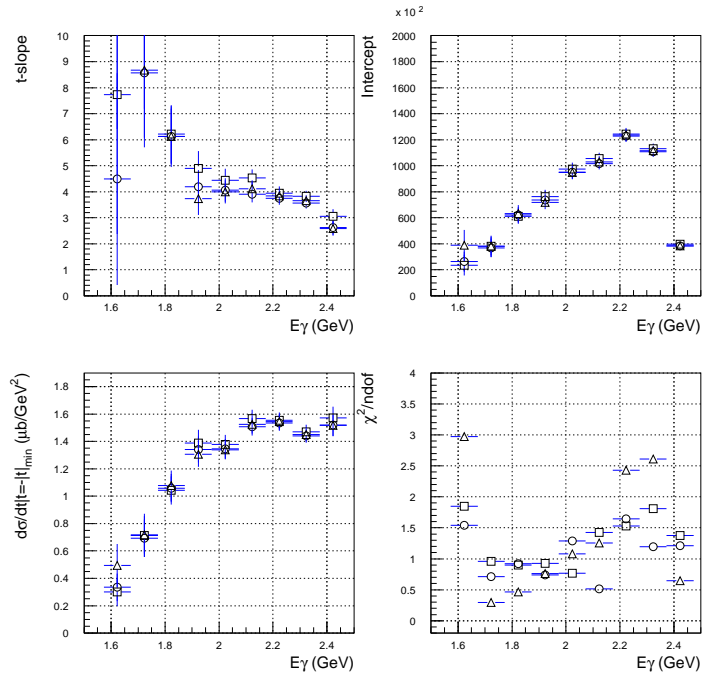
Figure B.7: Results of Approach 1 of LD$_2$ incoherent events.
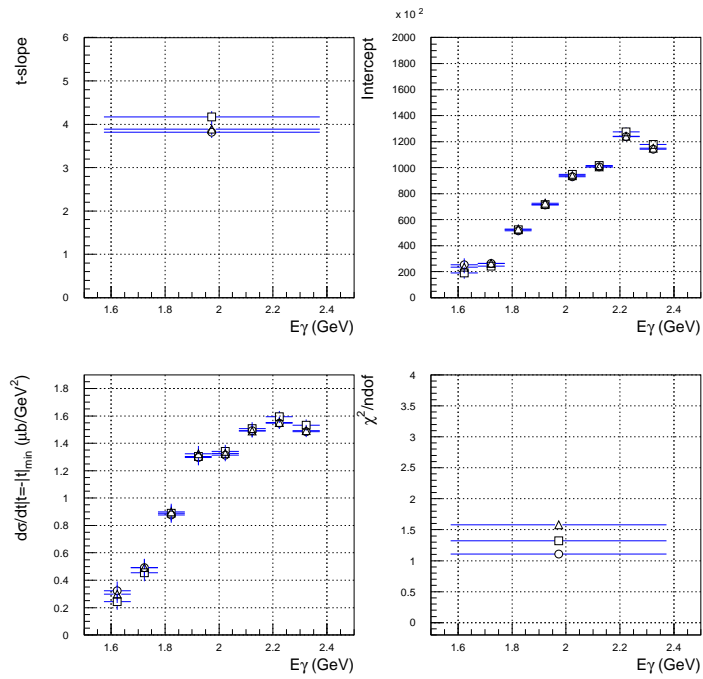
Figure B.8: Results of Approach 2 of LD$_2$ incoherent events.
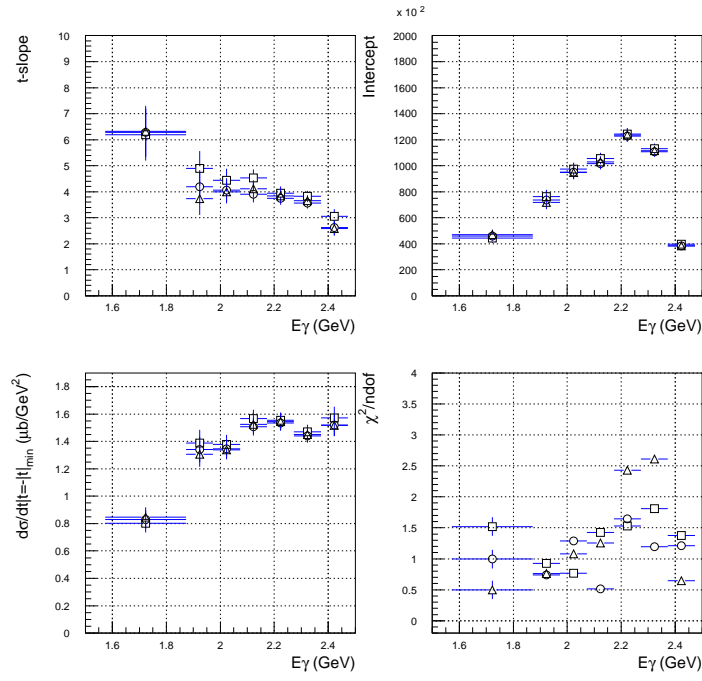
Figure B.9: Results of Approach 3 of LD_2 incoherent events.
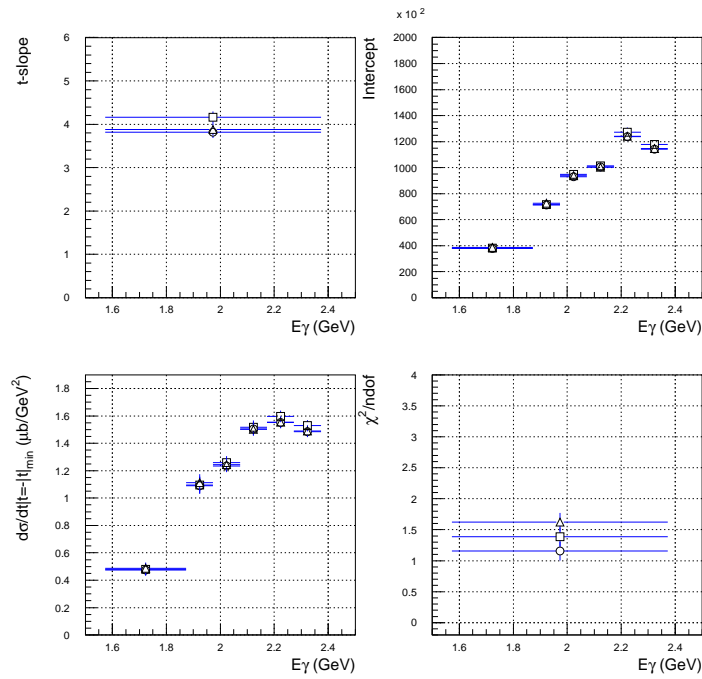
Figure B.10: Results of Approach 4 of LD_2 incoherent events.
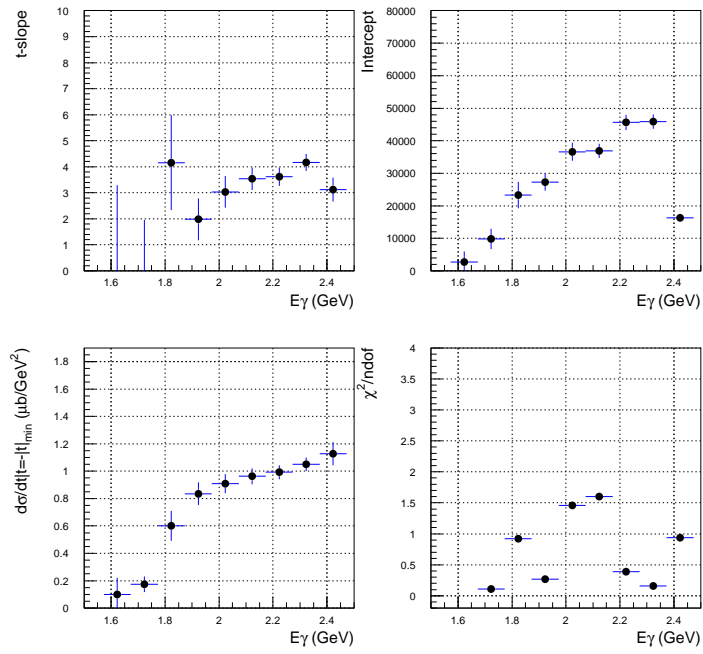
Figure B.11: Results of Approach 1 of LH_2 events.
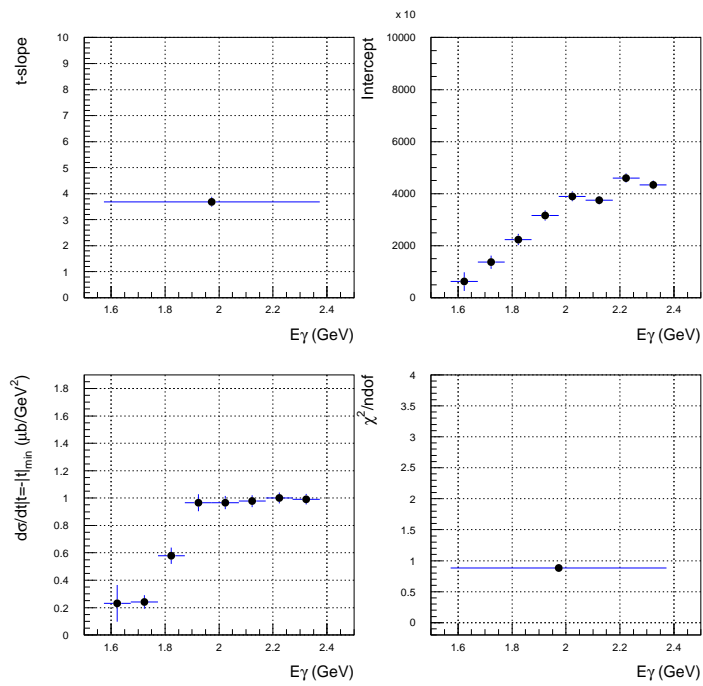
Figure B.12: Results of Approach 2 of LH_2 events.
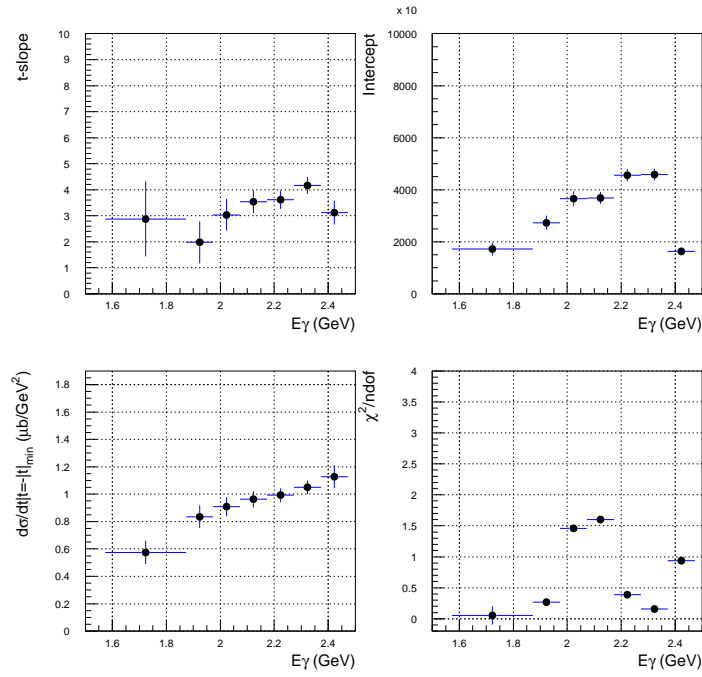
Figure B.13: Results of Approach 3 of LH_2 events.
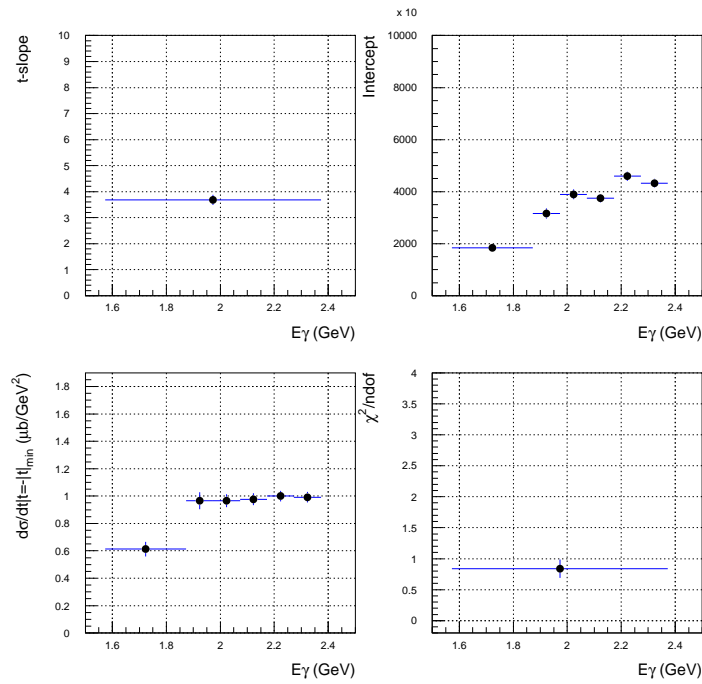
Figure B.14: Results of Approach 4 of LH_2 events.

Appendix C

Deuteron form factors

The cross sections of scattering experiments with nuclei or nucleons are determined by the form factors which contain all the information about the spatial distribution of the charge of them. The form factors can be interpreted as the probability for going from one particular initial state to a particular final state when a fix amount of three momentum $\mathbf{q}$ is transfered and can determine how the scattering rate is reduced from its value for a point-like scattering case.

At present, there is no decisive theoretical model for the form factor of deuteron. The adopted way of evaluating deuteron form factor in this analysis work is explained below in usual notations.

The radial wave function components of deuteron are parameterized with PARIS potential [29, 38]:

$$U(r) = \sum_{J=1}^{13} C_J \cdot exp(-m_J r), \tag{C.1}$$

$$W(r) = \sum_{J=1}^{13} D_J \cdot exp(-m_J r)(1 + \frac{3}{m_J r} + \frac{3}{m_J^2 r^2}), \tag{C.2}$$

where $U(r)$ and $W(r)$ are s- and d-wave functions of the deuteron state, C_J and D_J are coefficients of the parameterized deuteron wave function components as listed in Table C.1. The masses m_J are defined as $m_J = \alpha + (J-1)m_0$, with $m_0 = 1$ fm^{-1} and

$$\alpha = (2m_R \cdot |E_D|)^{1/2}/\hbar = 0.23162461 \text{ fm}^{-1}$$

where m_R and E_D are the neutron proton reduced mass and the deuteron binding energy. The wave functions are shown in Fig. C.1 with $U(r)$ represented in solid line and $W(r)$ in dash line.

With the deuteron wave functions formulated as Eq. C.1 and Eq. C.2, the deuteron charge form factor F_C, the quadrupole form factor F_Q, and the magnetic form factor F_M can be evaluated as is suggested in [18, 39, 40, 41]:

$$F_C(q) = [G_{Ep}(q) + G_{En}(q)] \int_0^\infty dr[U^2(r) + W^2(r)]j_0(\frac{qr}{2}), \tag{C.3}$$

$$F_Q(q) = 2[G_{Ep}(q) + G_{En}(q)] \int_0^\infty dr W(r)[U(r) - \frac{W(r)}{\sqrt{8}}]j_2(\frac{qr}{2}), \tag{C.4}$$

$$F_M(q) = [G_{Ep}(q) + G_{En}(q)] \int_0^\infty dr[U^2(r) + \frac{W^2(r)}{2}]j_0(\frac{qr}{2})$$
$$+ [\sqrt{2}U(r)W(r) + W^2(r)]j_2(\frac{qr}{2}), \tag{C.5}$$
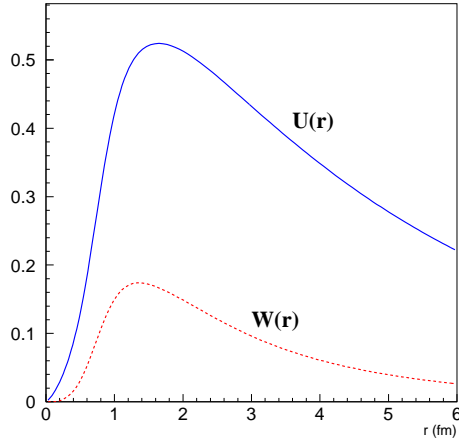
Figure C.1: Deuteron wave function components.

where j_n is spherical Bessel function of order n, G_{Ep}, and G_{En} are the proton and neutron electric and magnetic form factors defined as:

$$G_{Ep}(q) = (1 + \frac{q^2}{18.235 \text{ fm}^{-2}})^{-2},$$
$$G_{En}(q) = 0.$$

The absolute value of the electromagnetic form factors as the function of q^2 is shown in Fig. C.2 with $|F_C|$ represented by solid line, $|F_Q|$ by dash line, and $|F_M|$ by dot line.
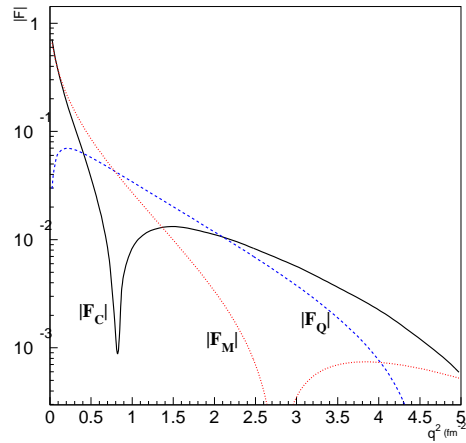
Figure C.2: Deuteron electromagnetic form factors.

The deuteron form factors for the natural and unnatural parity-exchange amplitude are

similar to the deuteron electromagnetic form factors and can be written as [18]:

$$S_1^N(q^2) = F_C(q^2) - \frac{1}{\sqrt{2}} F_Q(q^2), \tag{C.6}$$

$$S_0^N(q^2) = F_C(q^2) + \sqrt{2} F_Q(q^2), \tag{C.7}$$

$$S_1^U(q^2) = F_M(q^2). \tag{C.8}$$

The $S_M^{N,U}$ stands for the natural and unnatural parity-exchange form factors of the deuteron with spin projection M and are shown as the function of q^2 in Fig. C.3. The solid line is $S_1^N(q^2)$, the dash line is $S_0^N(q^2)$, and the dot line is $S_1^U(q^2)$. From Fig. C.3, it can be seen that form factors $S^{N,U}$ decrease rapidly with q^2 and S_1^N shows a dip around $q^2 = 5$ GeV^2
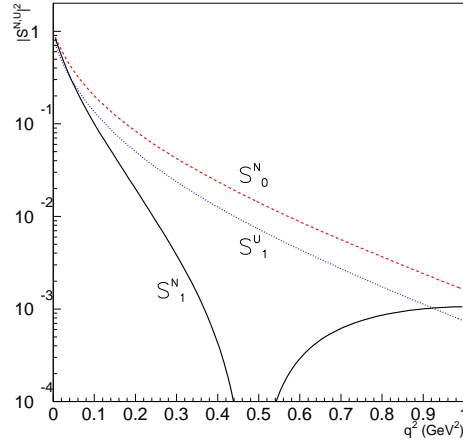
Figure C.3: Deuteron form factors of natural and unnatural exchange amplitude.

Table C.1: The coefficients of the parameterized deuteron wave function components

C_J (fm$^{-1/2}$)	D_J (fm$^{-1/2}$)
0.88688076×10^0	$0.23135193 \times 10^{-1}$
-0.34717093×10^0	-0.85604572×10^0
-0.30502380×10^1	0.56068193×10^1
0.56207766×10^2	-0.69462922×10^2
-0.74957334×10^3	0.41631118×10^3
0.53365279×10^4	-0.12546621×10^4
-0.22706863×10^5	0.12387830×10^4
0.60434469×10^5	0.33739172×10^4
-0.10292058×10^6	-0.13041151×10^5
0.11223357×10^6	0.19512524×10^5
-0.75925226×10^5	-0.15634324×10^5
0.29059715×10^5	0.66231089×10^4
-0.48157368×10^4	-0.11698185×10^4

The differential cross section of $\gamma + p \to \phi + p$ and $\gamma + d \to \phi + d$ can be derivied as [42]:

$$\frac{d\sigma}{dt}\Big|_{\gamma-p} = \frac{1}{16\pi \cdot \Phi(s_p, M_p, 0)} \times \frac{4}{4} \times |T^p|^2, \tag{C.9}$$

$$\frac{d\sigma}{dt}\Big|_{\gamma-d} = \frac{1}{16\pi \cdot \Phi(s_d, M_d, 0)} \times \frac{2}{6} \times F_{form} \times \frac{2M_d}{M_p} \times |T^d|^2, \tag{C.10}$$

where

$$\Phi(s, M_1, M_2) = [(s - M_1^2)^2 + M_2^4 - 2sM_2^2 - 2M_1^2 M_2^2]. \tag{C.11}$$

T^p and T^d are invariant amplitudes for each reaction. M_p and M_d are the masses of proton and deuteron. s is the Mandelstam variable. The factors, $4/4$ and $2/6$, are spin statistical factors. And the factor $2M_d/M_p$ in the equation of coherent interaction is the correcting factor for the non-relativistic wave function for the deuteron.

By the form factors derived in this appendix, Sum over the deuteron spin projection in the final state gives factor:

$$2 \cdot (S_1^N)^2 + (S_0^N)^2.$$

An additional factor 4 due to the coherent process from the proton and neutron need to be added, and therefore the overall form factor F_{form} can be written as:

$$F_{form} = 4[2 \cdot (S_1^N)^2 + (S_0^N)^2]. \tag{C.12}$$

Appendix D

Tables of normalization of yield

The correcting parameters used to derive the differential cross section are listed. The data is obtained from [35, 43, 36]. The number of target nucleons N_{target} can be derived as:

$$N_{target} = \frac{l_{tgt} \cdot \rho}{A} \cdot (6.02 \times 10^{23}) \tag{D.1}$$

Where l_{tgt} is the target length, ρ is the target density, and A is the atomic wight of the target. These quantities for LD$_2$ and LH$_2$ runs are all presented in the tables below.

Table D.1: Normalization factor

E_γ bin (GeV)	F_{norm}
1.573 - 1.673	1.25290
1.673 - 1.773	1.42316
1.773 - 1.873	1.23063
1.873 - 1.973	1.33199
1.973 - 2.073	1.13190
2.073 - 2.173	1.32088
2.173 - 2.273	1.23043
2.273 - 2.373	1.23579
2.373 - 2.473	1.34186

Table D.2: Beam efficiency including tagger inefficiency and backward Compton scattering spectra

E_γ bin (GeV)	F_{beam}
1.573 - 1.673	0.0867
1.673 - 1.773	0.0910
1.773 - 1.873	0.0969
1.873 - 1.973	0.1044
1.973 - 2.073	0.1142
2.073 - 2.173	0.1258
2.173 - 2.273	0.1400
2.273 - 2.373	0.1344
2.373 - 2.473	0.0485

Table D.3: Other parameters used in deducing differential cross section

	LD_2 runs	LH_2 runs
N_{beam}^{VT}	2.27×10^{12}	1.71×10^{12}
N_{beam}^{HT}	2.24×10^{12}	1.50×10^{12}
N_{beam}	4.51×10^{12}	2.21×10^{12}
$\rho \ (g/cm^3)$	0.1790	0.0708
A $(g/mole)$	2.0140	1.0079

Table D.4: Other parameters used in deducing differential cross section common for LD_2 and LH_2 data

$l_{tgt} \ (cm)$	16
R_{branch}	0.492
η_{trans}	0.52

Appendix E

Supplementary plots

E.1   Results of examination on other off-shell schemes

The plots of the results of examination in other schemes are shown here with the same convention discussed in subsection 3.7.2.
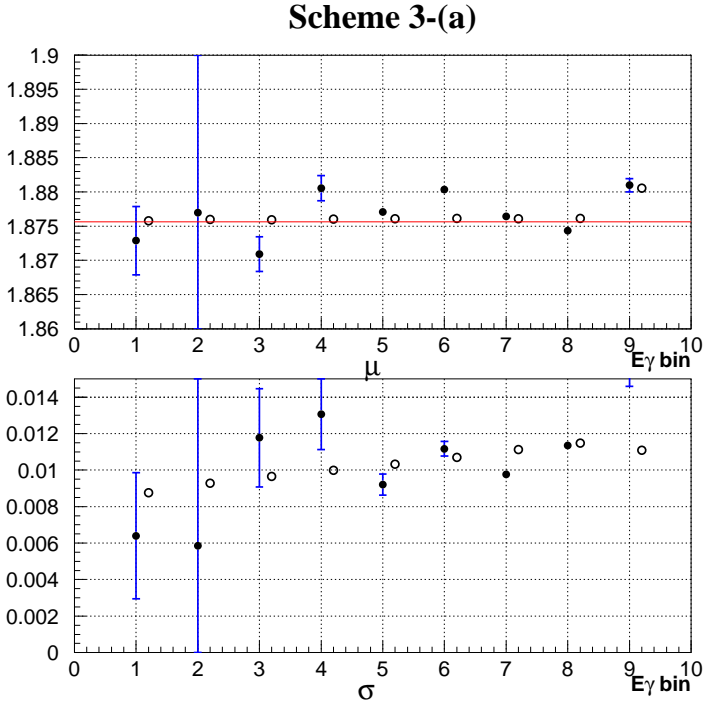
Figure E.1: Scheme 3-(a), off-shell effect examination on peak and width in different E_γ bin.
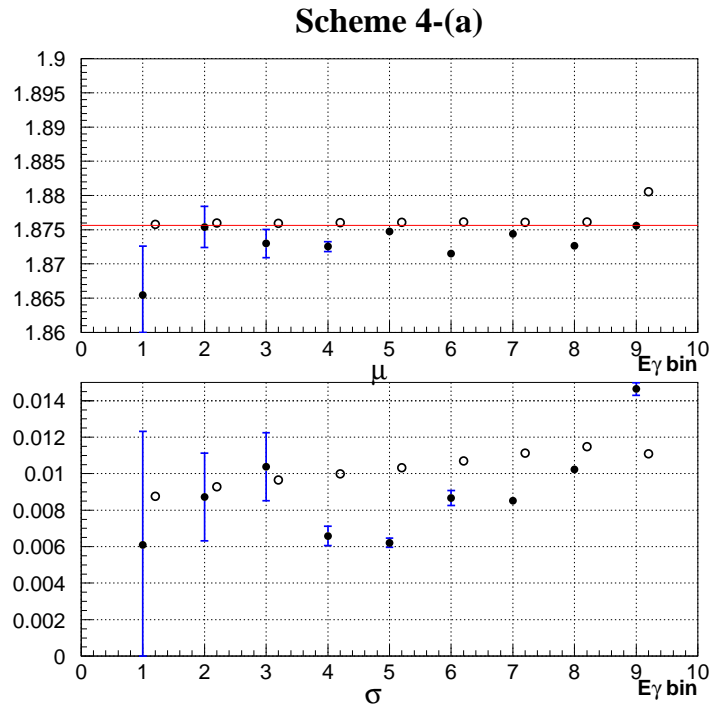
Figure E.2: Scheme 4-(a), off-shell effect examination on peak and width in different E_γ bin.
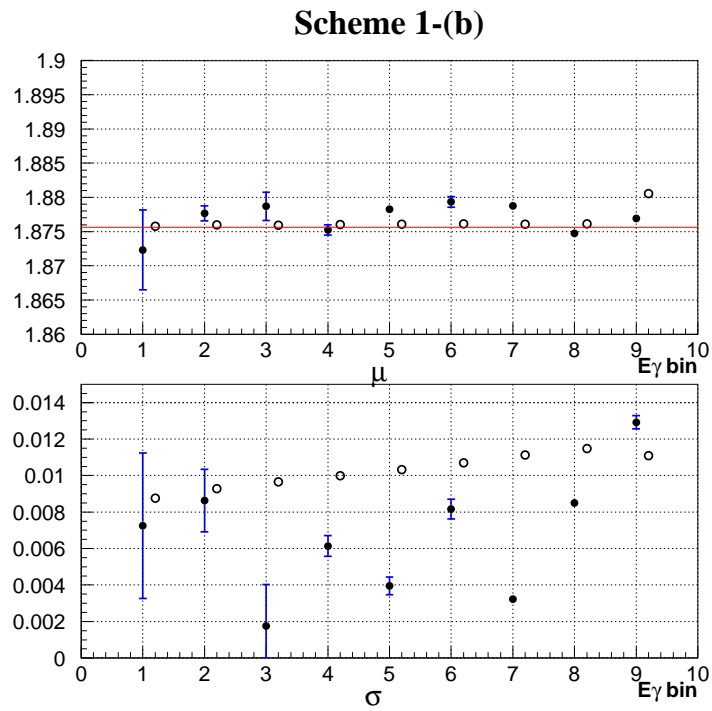
Figure E.3: Scheme 1-(b), off-shell effect examination on peak and width in different E_γ bin.
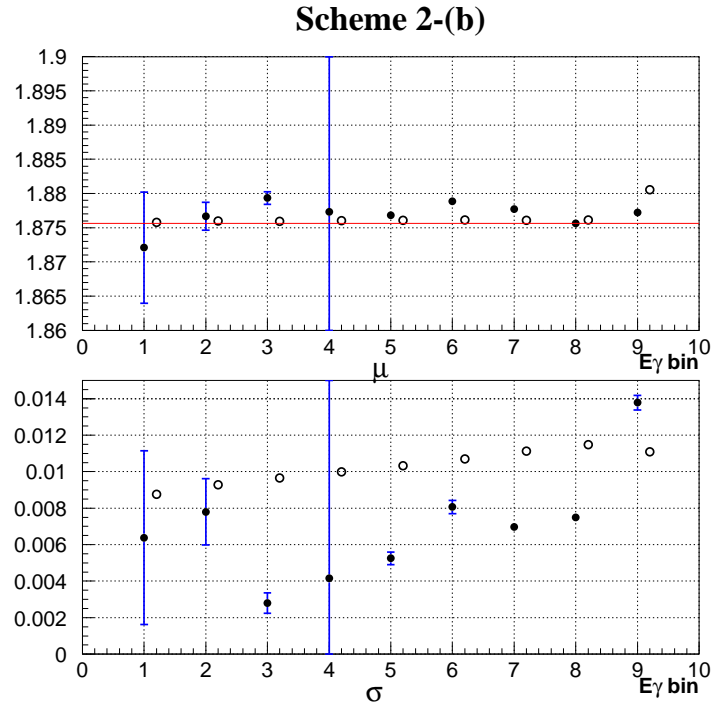
Figure E.4: Scheme 2-(b), off-shell effect examination on peak and width in different E_γ bin.
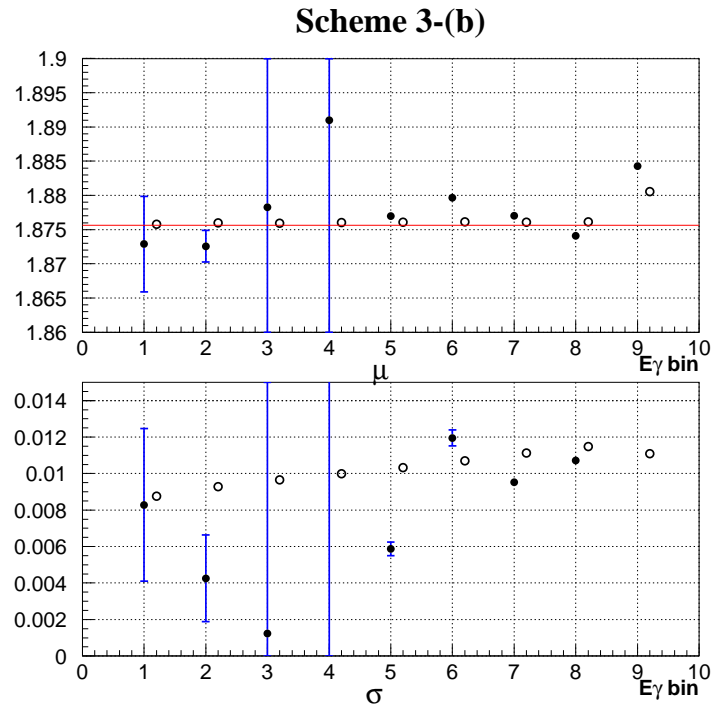
Figure E.5: Scheme 3-(b), off-shell effect examination on peak and width in different E_γ bin.
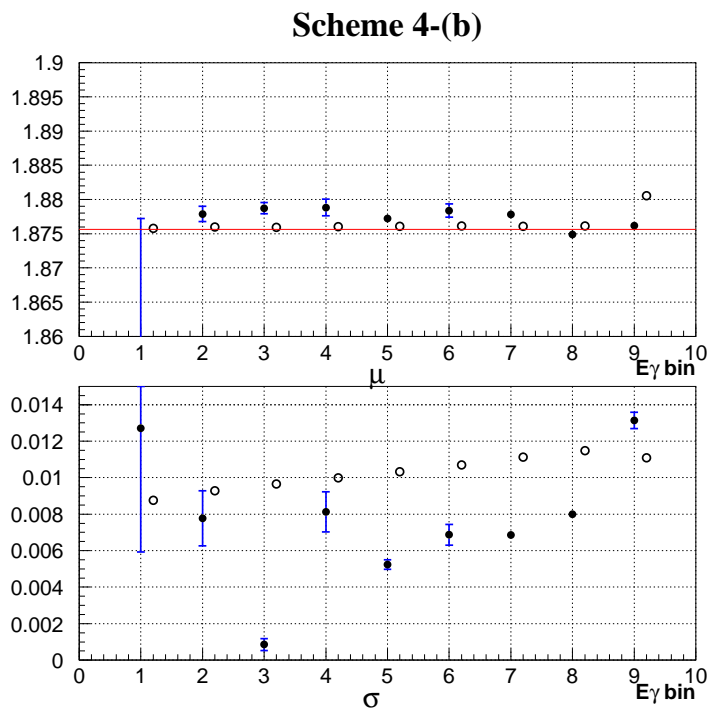
Scheme 4-(b)

Figure E.6: Scheme 4-(b), off-shell effect examination on peak and width in different E_γ bin.
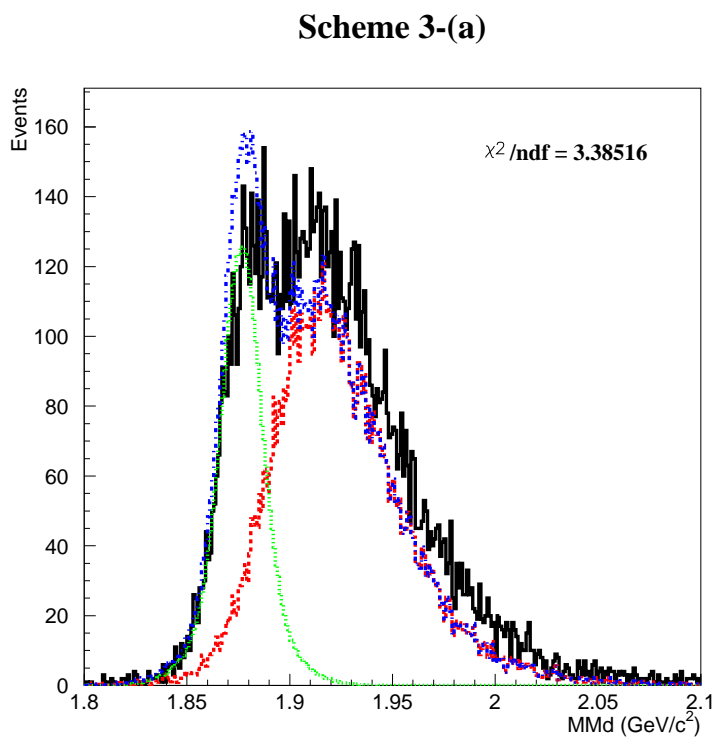
Scheme 3-(a)

Figure E.7: Scheme 3-(a), off-shell effect examination on MM_d fitting.

Scheme 4-(a)
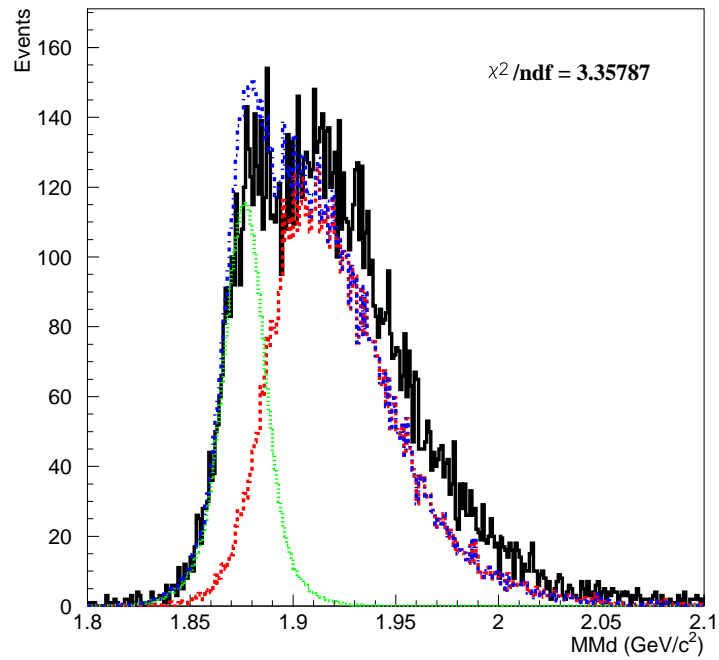
Figure E.8: Scheme 4-(a), off-shell effect examination on MM_d fitting.

Scheme 1-(b)
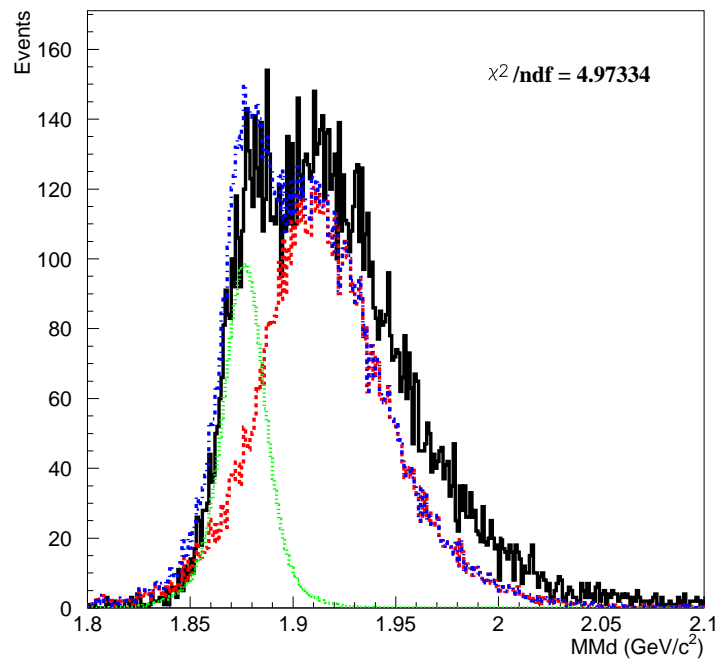
Figure E.9: Scheme 1-(b), off-shell effect examination on MM_d fitting.

Scheme 2-(b)
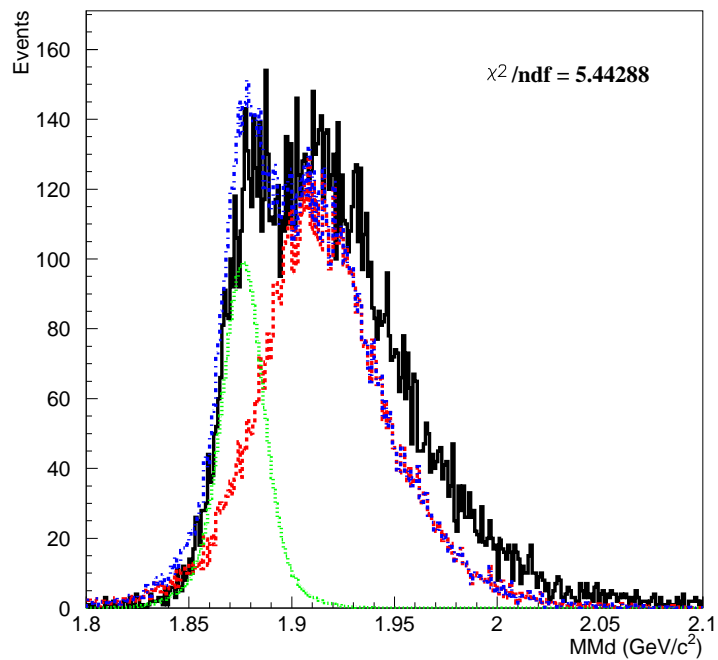
Figure E.10: Scheme 2-(b), off-shell effect examination on MM_d fitting.

Scheme 3-(b)
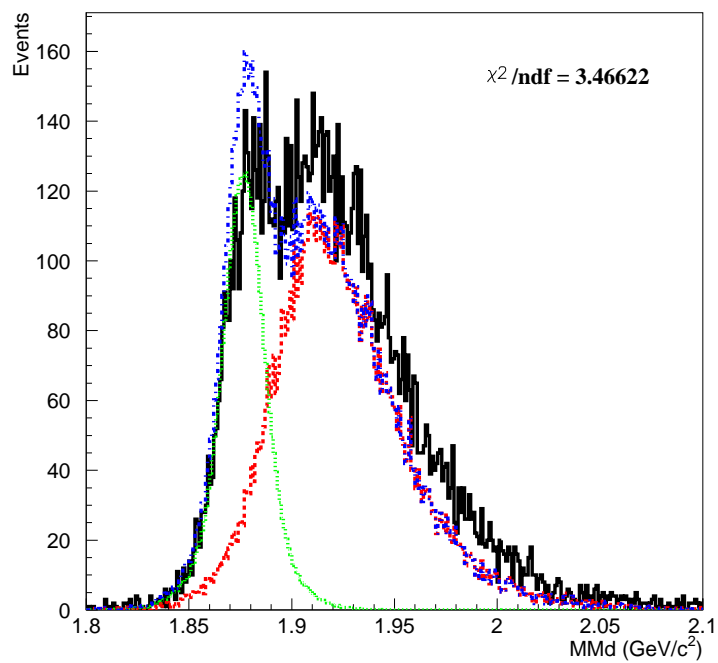
Figure E.11: Scheme 3-(b), off-shell effect examination on MM_d fitting.

Scheme 4-(b)
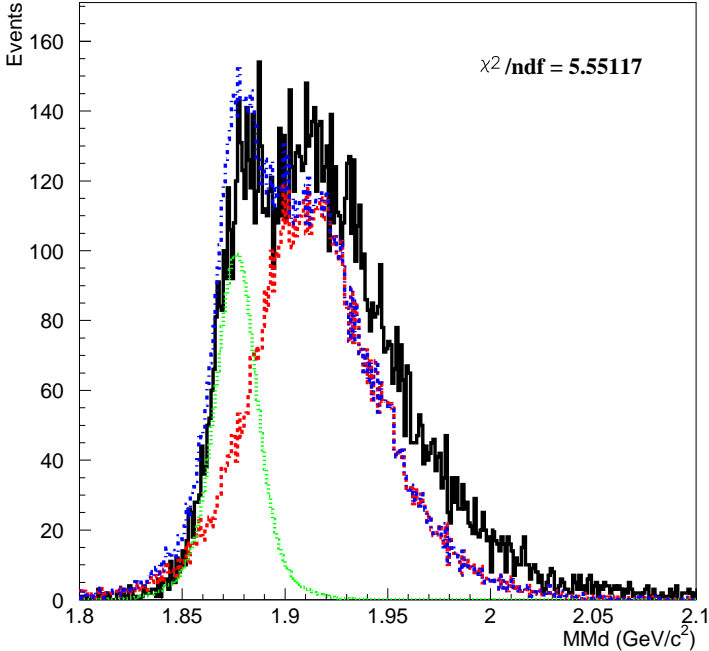
Figure E.12: Scheme 4-(b), off-shell effect examination on MM_d fitting.

E.2   MM$_d$ fitting

The MM$_d$ fitting in each E_γ , $\tilde{t}$ bin is illustrated here. The $\tilde{t}$ bins marked on the plots are
defined in Table 4.1. In every plot, the solid line is the MM$_d$ distribution and the dash line is
the result of the fit. Although the number of events is low in the low E bins and T bins, the
fitting is observed to be generally reasonable.
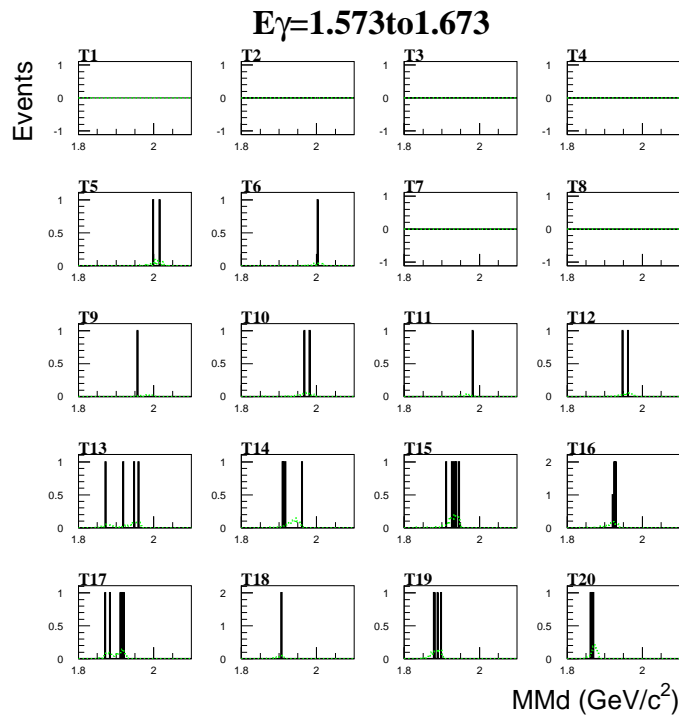
Figure E.13: E1 bin, MM$_d$ fitting.
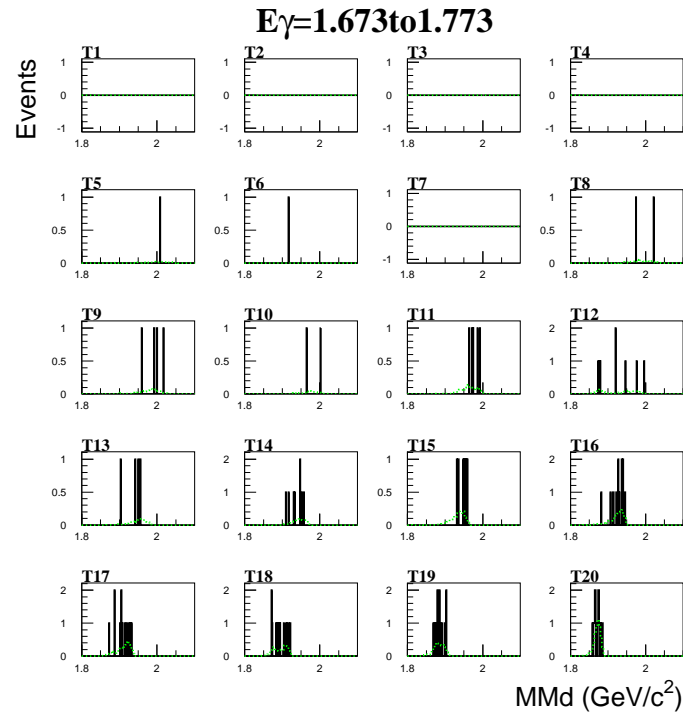
Figure E.14: E2 bin, MM$_d$ fitting.
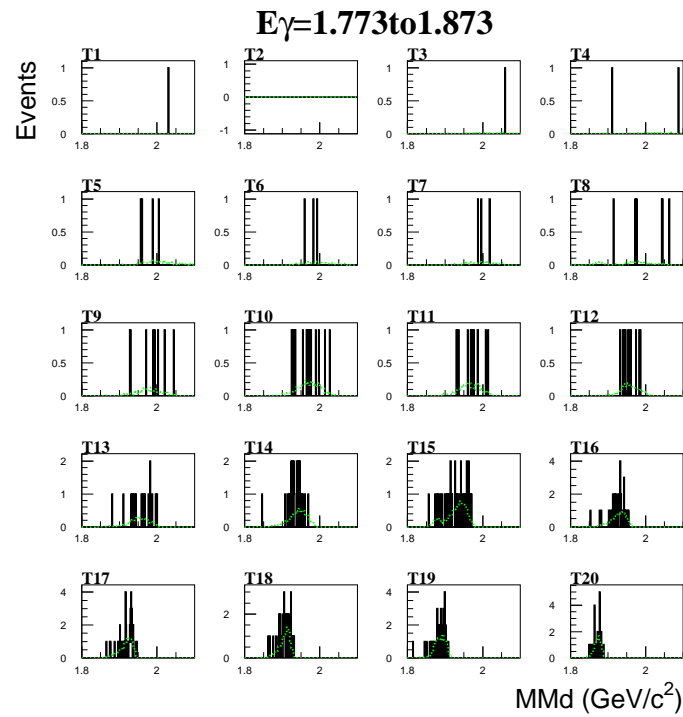
Figure E.15: E3 bin, MM$_d$ fitting.

Eγ=1.873to1.973
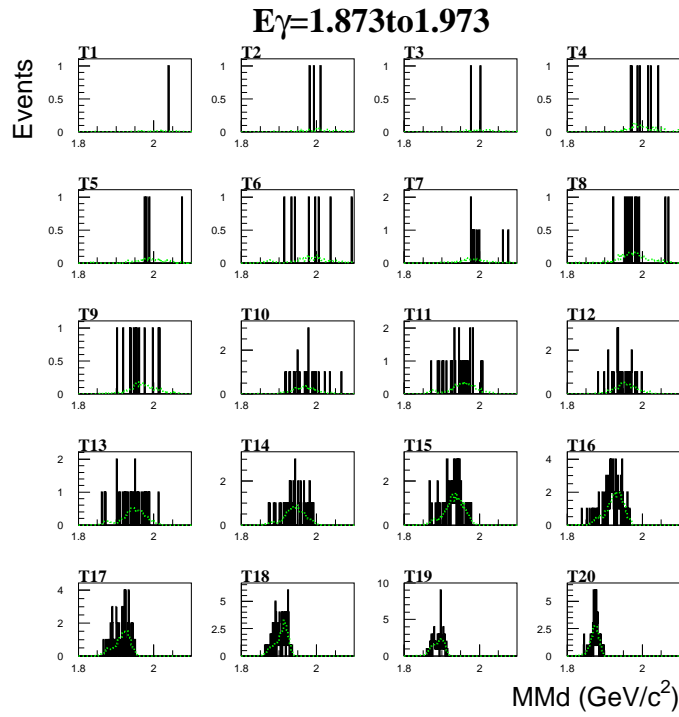
Figure E.16: E4 bin, MM$_d$ fitting.

Eγ=1.973to2.073
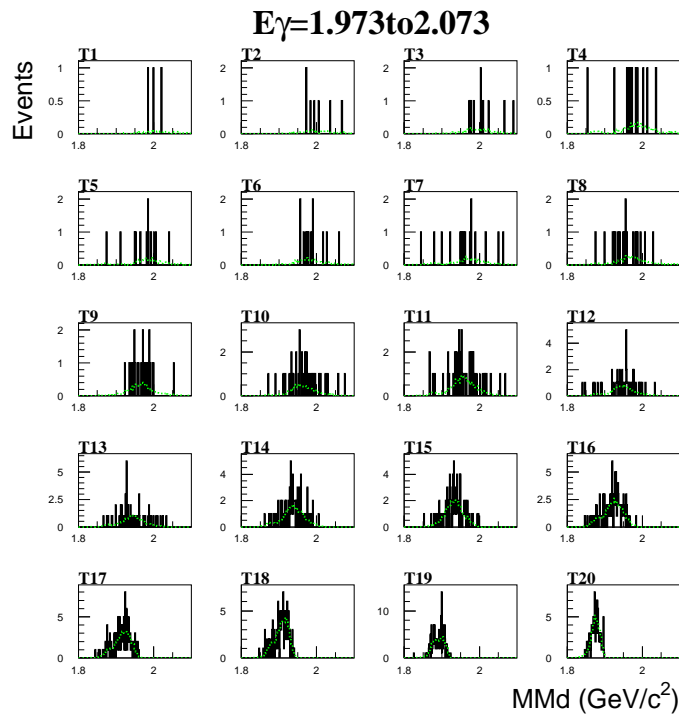
Figure E.17: E5 bin, MM$_d$ fitting.

Eγ=2.073to2.173
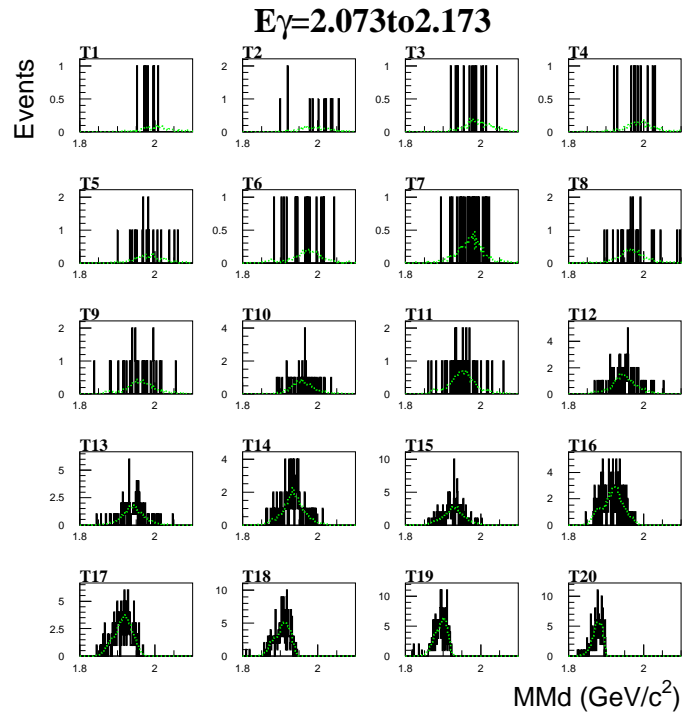
Figure E.18: E6 bin, MM_d fitting.

Eγ=2.173to2.273
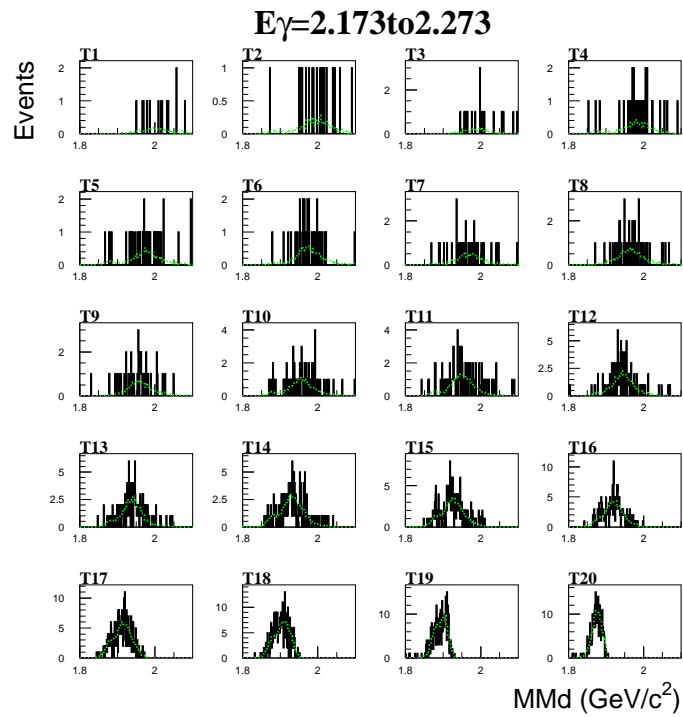
Figure E.19: E7 bin, MM_d fitting.

Eγ=2.273to2.373
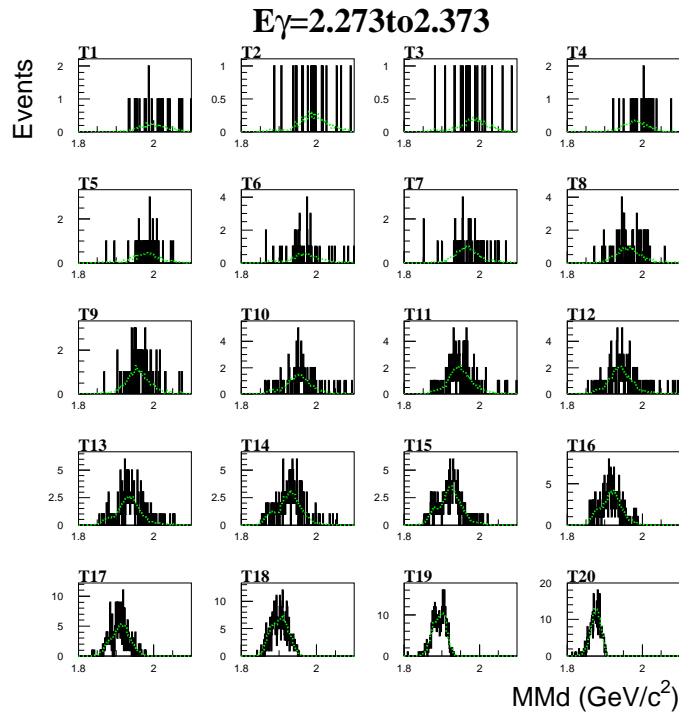
Figure E.20: E8 bin, MM$_d$ fitting.

Eγ=2.373to2.473
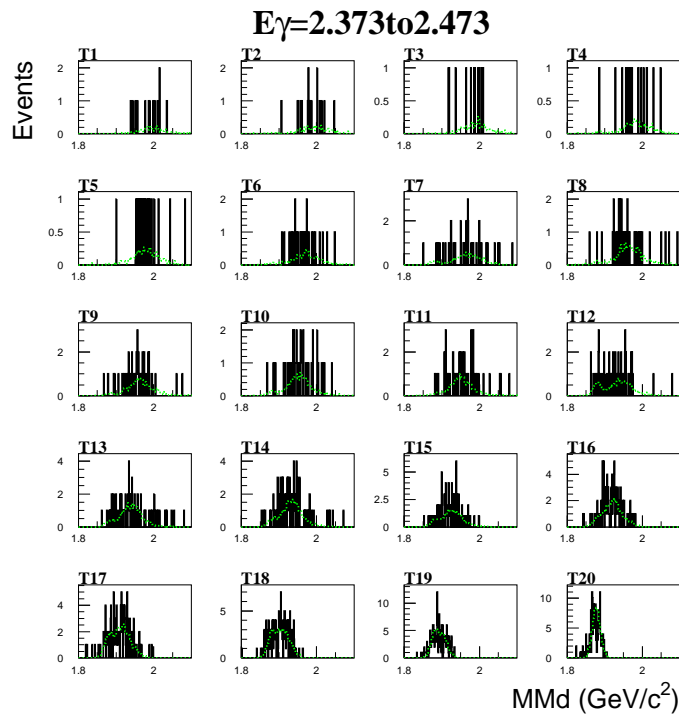
Figure E.21: E9 bin, MM$_d$ fitting.

Bibliography

[1] Martin L. Perl, *High Energy Hadron Physics*, JOHN WILEY & SONS, New York, 1974, and references therein.

[2] S. Donnachie, G. Dosch, P. Landshoff, and O. Nachtmann, *Pomeron Physics and QCD*, Cambridge University Press, Cambridge, England 2002, and references therein.

[3] O. Nachtmann, *Pomeron Physics and QCD*, `hep-ph/0312279` (2003).

[4] E. Anciant *et al.*, Phys. Rev. Lett. **85**, 4682 (2000).

[5] M. A. Pichowsky and T.-S. H. Lee, Phys. Rev. **D 56**, 1644 (1997).

[6] A. I. Titov, T.-S. H. Lee, H. Toki, and O. Streltsova, Phys. Rev. **C 60**, 035205 (1999).

[7] J.-M. Laget, Phys. Lett. **B 489**, 3133 (2000).

[8] T. Nakano and H. Toki, in *Proceedings of the International Workshop on Exciting Physics with New Accelerators Facilities, SPring-8, Hyogo* (World Scientific, Singapore, 1997).

[9] A. I. Titov and T.-S. H. Lee, Phys. Rev. **C 67**, 065205 (2003).

[10] A. I. Titov, Y. Oh, and S. N. Yang, Phys. Rev. Lett. **79**, 1634 (1997).

[11] A. I. Titov, T.-S. H. Lee, and H. Toki, Phys. Rev. **C 59**, R2993 (1999).

[12] T. Mibe, W.C. Chang, T. Nakano *et al.* (The LEPS collaboration), Phys. Rev. Lett. **95**, 182001 (2005).

[13] J. Barth *et al.*, Eur. Phys, J. A. **17**, 269 (2003).

[14] D. P. Barber *et al.*, Z. Phys. **C 12**, 1 (1982).

[15] H.-J. Behrend *et al.*, Nucl. Phys. **B144**, 22 (1978).

[16] U. Siodlaczek *et al.*, Eur. Phys. J. A **10**, 365 (2001).

[17] J. Weiß *et al.*, Eur. Phys. J. A **11**, 371 (2001).

[18] A. I. Titov, M. Fujiwara, and T.-S. H. Lee, Phys. Rev. **C 66**, 022202(R) (2002).

[19] G. McClellan *et al.*, Phy. Rev. Lett. **26**, 1593 (1971).

[20] CERN Program Library entry Q121, The Complete Reference **PAW** - *Physics Analysis Workstation*, v 1.07, Oct 1989.

[21] Particle Data Group.

[22] T. Mibe, Doctoral dissertation, Osaka University, 2004.

[23] J. Y. Chen, Master's thesis, National Kaohsiung Normal University, 2002.

[24] Y. Kato, *Current status of estimation of E_γ resolution*, report of LEPS collaboration meeting in Taiwan, 12-13 Jun 2006.

[25] T. Nakano *et al.*, Nucl. Phys. **A684**, 71 (2001).

[26] M. Sumihama *et al.*, Phys. Rev. **C 73**, 035214 (2006).

[27] Suggested by T. Nakano.

[28] Bogdan Povh *et al.*; translated by Martin Lavelle, *Particles and nuclei: an introduction to the physical concepts* 4th ed., Springer, Berlin; New York, 2004.

[29] M. Lacombe *et al.*, Phys. Lett. **101B**, 139 (1981).

[30] H. W. L. Naus and J. H. Koch, Phys. Rev. **C 36**, 2456 (1987).

[31] S. Kondratyuk, G. Martinus, and O. Scholten, Phys. Lett. **B 418**, 20 (1998).

[32] Suggested by T. Nakano and W. C. Chang.

[33] CERN Program Library entry D506, **MINUIT** - *Function Minimization and Error Analysis*, v 94.1 , Aug 1998.

[34] K. Lukashin *et al.* (The CLAS collaboration), Phys. Rev. **C 63**, 065205 (2001).

[35] H. Kohri, LEPS technical note **28** (2005).

[36] W. C. Chang and P. J. Lin, LEPS technical note **29** (under preparation), (2006).

[37] T. Chujo *et al.*, *Analysis Note: Determination of Charged Hadron PID boundaries by TOF (Study of squared mass resolution, momentum resolution, and TOF resolution)*, 2000.

[38] M. Lacombe *et al.*, Phys. Rev. **C 21**, 861 (1980).

[39] M. I. Haftel, L. Mathelitsch, and H. F. K. Zingl, Phys. Rev. **C 22**, 1285 (1980).

[40] A. K. A. Azzam *et al.*, Turk. J. Phys. **29**, 127 (2005).

[41] J. E. Elias *et al.*, Phys. Rev. **177**, 2075 (1969).

[42] A. I. Titov, private communications.

[43] H. Kohri, private communications.